5-1-2018

The paddlefish rostrum as a structure for bio-inspiration

Jeremiah Francis Deang

Recommended Citation

Deang, Jeremiah Francis, "The paddlefish rostrum as a structure for bio-inspiration" (2018). *Theses and Dissertations*. 4579.
https://scholarsjunction.msstate.edu/td/4579

The paddlefish rostrum as a structure for bio-inspiration

By

Jeremiah Francis Deang

A Dissertation
Submitted to the Faculty of
Mississippi State University
in Partial Fulfillment of the Requirements
for the Degree of Doctor of Philosophy
in Mechanical Engineering
in the Department of Mechanical Engineering

Mississippi State, Mississippi

May 2018

The paddlefish rostrum as a structure for bio-inspiration

By

Jeremiah Francis Deang

Approved:

Mark Horstemeyer
(Major Professor)

Hongjoo Rhee
(Committee Member)

Lakiesha Williams
(Committee Member)

Youssef Hammi
(Committee Member)

Paul Allison
(Committee Member)

Yucheng Liu
(Graduate Coordinator)

Jason Keith
Dean
Bagley College of Engineering

Name: Jeremiah Francis Deang

Date of Degree: May 4, 2018

Institution: Mississippi State University

Major Field: Mechanical Engineering

Major Professor: Mark Horstemeyer

Title of Study: The paddlefish rostrum as a structure for bio-inspiration

Pages in Study 131

Candidate for Degree of Doctor of Philosophy

The proposed research investigates the unique structure of the rostrum of the paddlefish (*Polyodon spathula*) for use in bio-inspiration. The rostrum comprises three different materials: midline cartilage, a network cartilage structure, and matrix tissue. The structure-property relationships of these materials were studied with various mechanical testing and imaging techniques. The mechanical properties and stress-strain behavior were applied to a material model that characterizes each material. A three-dimensional model was constructed from computed tomography images, and a mesh was exported for use in finite element simulations. Different boundary conditions were applied to show how the rostrum responds under deformation giving a stress distribution arising from different loadings. Finally, a new robust design paradigm is introduced with bio-inspiration introducing constraints and is explained through using the paddlefish rostrum as an example of a cell tower or antenna.

DEDICATION

I would first like to dedicate this work to my parents for their support as I continued furthering my education. I would also like to dedicate this work to my wife, Amina, who I met during my PhD process. Thank you for your love, encouragement, and constant joy you bring to my life. I love you.

Lastly, I would like to dedicate this work to God who has blessed me far beyond what I deserve.

> *"But now ask the beasts, and let them teach you; And the birds of the heavens, and let them tell you. Or speak to the earth, and let it teach you; and let the fish of the sea declare to you. Who among all these does not know that the hand of the LORD has done this, in whose hand is the life of every living thing, and the breath of all mankind?"* *Job 12:7-10*

ACKNOWLEDGEMENTS

I would like to acknowledge my major advisor Mark Horstemeyer who has not only shaped my professional career but has greatly impacted me in all aspects of my life. I am grateful for his support and the PhD process I’ve gone through under his guidance. Additionally, I would also like to thank my committee members Youssef Hammi, Hongjoo Rhee, Lakiesha Williams, and Paul Allison for their invaluable insight and guidance.

I’m very thankful for the countless people at CAVS for not only their expertise, but their willingness to go above and beyond in my graduate school endeavors. It would be impossible to name everyone along this journey, but some people in particular that I would like to acknowledge are Andy Oppedal, Raj Prabhu, Stephen Horstemeyer, Melissa Mott, Kyle Johnson, Will Lawrimore, Nayeon Lee, Denver Seely, Heechen Cho, Tate Fonville, and Karen Persons.

I would like to acknowledge the United States Army Corps of Engineers (USACE) Engineer Research and Development Center (ERDC) Structures Lab and CAVS of their mechanical labs and experimental equipment. Special thanks to the ERDC Environmental Laboratory's Fish Ecology team for the fun and informative trips taken to attain and study paddlefish.

Additionally, I would like to thank Farrokh Mistree, Janet Allen, and the Systems Realization Lab (SRL) team for their assistance and teaching of the design process from their perspective.

This effort was sponsored by the Army ERDC Laboratory in the Department of Defense (DoD). The U.S. Government is authorized to reproduce and distribute reprints for Governmental purposes notwithstanding any copyright notation thereon. The views and conclusions contained herein are those of the authors and should not be interpreted as necessarily representing the official policies or endorsements, either expressed or implied, of the U.S. Government and the DoD.

TABLE OF CONTENTS

LIST OF TABLES

LIST OF FIGURES

CHAPTER I

INTRODUCTION

1.1 Summary

The proposed research investigates the unique structure of the rostrum (or nose) of the paddlefish (*Polyodon spathula*). The rostrum comprises three different materials: midline cartilage, a network cartilage structure, and matrix tissue. The structure-property relationships of these materials were studied with various mechanical testing and imaging techniques. The mechanical properties and stress-strain behavior were applied to a material model that characterizes each material. A three-dimensional model was constructed from computed tomography images, and a mesh was exported for use in finite element simulations. Different boundary conditions were applied to show how the rostrum reacts and the stress distribution arises while it is subjected to different loadings. Finally, a new design paradigm constructed with the compromised Decision Support Problem (cDSP) is introduced with the inclusion of bio-inspiration and is explained through an example using the paddlefish rostrum.

1.2 Intellectual Merit

The proposed research aims to perform an unprecedented study on the materials and the design of the paddlefish rostrum from a structure-property perspective. Although paddlefish have been researched for their electric-sensing ability, the characterization of the structure-property-function relations of the components of the rostrum has not been studied. Furthermore, the structural scale was investigated through finite element simulations, which provided insight into how the rostrum responded to various loads and pressures. Additionally, a new design paradigm with the addition of bio-inspiration was introduced in which constraints were applied to a cell tower.

1.3 Broader Impacts

The paddlefish rostrum may provide a novel design for lightweight and high-strength materials for use in various applications such as cell towers, hydrodynamic design, and protective structures. The inclusion of bio-inspiration into a design paradigm, will have wider applicability, providing application to new designs based on important features observed in biological structures.

1.4 Background

Nature provides many examples of novel structures and materials that can serve as examples and concept generation for bio-inspired engineering designs for high performance materials and systems. The biological materials and structures studied tend to be multifunctional and can serve a multitude of mechanical functions that include impact resistance, fracture resistance, armor, and protection. Because of these characteristic traits, biological materials have become a source of inspiration in the field of bio-inspired design and biomimetics (1)(2)(3)(4)(5).

The relationship between mechanics and engineering with nature has been around for thousands of years; William Harvey was the first to identify the heart as an active pump circulating blood throughout the system of vessels and veins, and Giovanni Borelli carefully studied animal locomotion (6). Today, biomechanics gives engineers new opportunities for novel designs to develop new kinds of machines and structures. Though bio-inspiration and biomimetics are relatively new research fields, the general concepts and notions of looking at nature for designs has long existed. For example, the Chinese tried to produce artificial silk over 3000 years ago. Additionally, Leonardo Da Vinci observed birds, the shapes of the wings, and the motions of flight to invent new bio-inspired designs (see Figure 1.1) for flying machines (7).

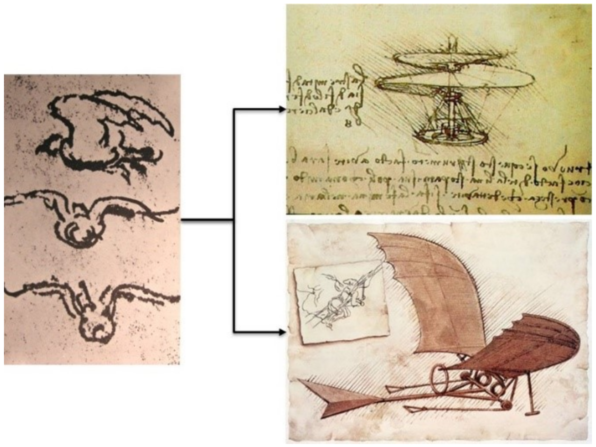

Figure 1.1 Observations of birds by Da Vinci used as bio-inspiration for flying machines (7).

This trend of exploring nature for new ideas has continued today, where many animals are used as inspiration for the conception of innovative ideas. For example, Meyers *et al.* (1) have studied abalone shells in applications for multifunctional materials. Lee *et al.*

(8) have studied woodpecker's beaks for energy absorption. Johnson *et al*. (9) have investigated the material properties and geometry of the ram's horn that are responsible for shock absorption. From gecko's feet and the bird wings to fish scales and spider silk, nature is constantly providing new ideas into the world of engineering. All around are biological structures that have inspired many of the mechanical designs we use today. Figures 1.2 and 1.3 show two more examples of bio-inspiration enhancing and creating new designs for trains and cars. The beak of the kingfisher bird shown in Figure 1.2 inspired the nose of the train in an effort to reduce the build-up of air pressure as the Shinkansen train travels through the tunnels at speeds of up to 240 km/hr. Not only did the new design solve the air pressure problem, but it also reduced power use and enabled higher speeds (2).

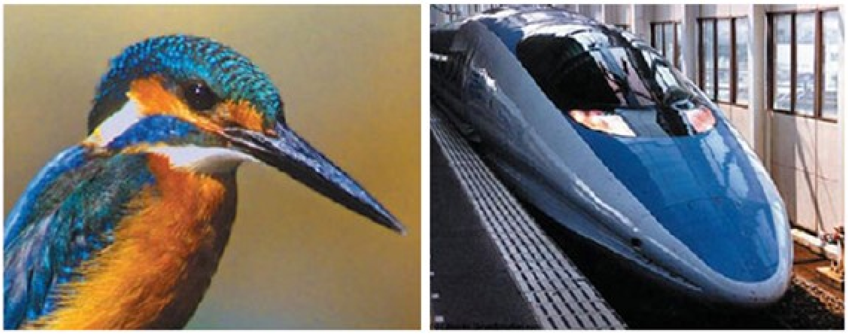

Figure 1.2 Kingfisher beak (left) used for the bio-inspiration of the nose of the Shinkansen train (right)(2).

Shown in Figure 1.3, Mercedes Benz introduced a new car design in 2011 based on studies done on the shape of the boxfish, which was shown to contribute to the fish's hydrodynamic stability while swimming.

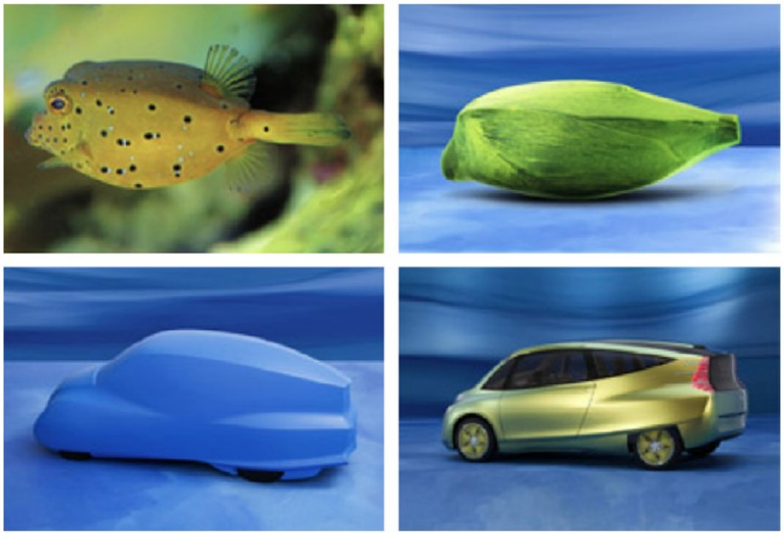

Figure 1.3 Boxfish shape used as bio-inspiration for a car design (2).

The work being presented in this dissertation focuses on another biological structure: the paddlefish (*Polyodon spathula*) rostrum, or nose. The cardinal aim of this research to gain insight and understanding of the rostrum structure through finite element analysis and structure-property relationships of the materials that comprise the rostrum.

Though the shape of the rostrum, is a simple "bill," the rostrum has a unique structure composed of a complex composition of skin, stellate bones, cartilage, and tissue. Additionally, according to Gurgens *et al.* (10), paddlefish are unique in the sense that they are the only fish known to use electric senses to detect and feed on plankton, with the rostrum functions as an electrosensory organ. Because the rostrum behaves as an antenna, the paddlefish are able feed on planktonic prey in the muddy Mississippi river where visibility is limited (11)(12). Like the sharks studied by Kaijura (13)(14), the paddlefish also contain the electrosensory pores called the Ampullae of Lorenzini (15). These electrical sensing organs are found on the head and gill cover, but they are especially numerous on the rostrum which provide spatial resolution for detecting and capturing plankton, thus providing the paddlefish with a greater search area for its prey. Additionally, Gurgens *et al.* (10) conducted a study displaying the paddlefish's electrosensory ability by showing how the fish avoids metal obstacles within a tank. Similar studies on sharks were also performed by Kaijura and Holland (14). The reaction of paddlefish to boat traffic shown by Rosen and Hales (16) is similar to the avoidance response of the paddlefish from metal objects being introduced into a tank. Further experiments were done by Wilkens *et al.* (11),(17) that show that the rostrum functions as an electrosensory antenna in plankton feeding. They were able to isolate the electrosensory function and showed that the paddlefish can feed on plankton solely on its electrical sensing ability alone. Furthermore, Wojtenek *et al*. (12) performed a study showing that paddlefish will even strike at artificial dipoles that simulate the weak electric fields of its planktonic prey.

Additionally, hydrodynamic characterization of the rostrum has been performed using computational fluid dynamics quantifying the amount of lift that is generated by the rostrum and comparing the results to hydrofoils (18). Though the paddlefish has a three-dimensional lattice of stellate bones that are unique to the paddlefish family (19), little research exists investigating the rostrum as a structural system for bio-inspiration.

1.5 Dissertation Structure

The following dissertation is divided into six chapters that will explore the paddlefish rostrum and bio-inspiration. Parts of this dissertation has been submitted for publication as separate works and were slightly modified to create this single, comprehensive dissertation.

Chapter 2 explores the material properties of the constituent materials of the rostrum. The mechanical properties of the midline cartilage, network cartilage, and network tissue were explored through characterization and mechanical testing techniques. Spatial dependence, strain rate dependence, and stress state dependence were explored. Materials were also characterized through a histological study and Fourier transform infrared spectroscopy. The results within this chapter lay the foundation for the material model used in the simulations in Chapter 3

In Chapter 3, finite element simulations of the rostrum were performed. The three-dimensional model was produced, and a mesh used for simulation in abaqus was exported. The mechanical properties discovered in the previous chapter were applied to the material models. Simulation results from various boundary conditions and loadings on the rostrum are presented, and observations are made on the stress distributions observed in the stress tensor components.

Chapter 4 discusses the incorporation of bio-inspiration into the design process; In particular, this chapter reviews the aspects of the compromised Decision Support Problem (cDSP) and introduces bio-inspiration ideas into the cDSP design frame. A cell tower design is used as an example, and the components of the design process are described.

Finally, Chapter 5 gives a summary of the dissertation, outlining some notable conclusions, and Chapter 6 provides suggestions for future and additional research areas to explore.

CHAPTER II

EXPERIMENTAL RESULTS FROM QUASI-STATIC AND HIGH-STRAIN RATE MECHANICAL TESTING OF THE CONSTIUENT MATERIALS IN THE PADDLEFISH ROSTRUM

2.1 Introduction

Biomechanics seeks to understand the mechanics of living systems by studying the proteins, tissues, and cells of various tissues, which provide a wide array of functionality and characteristics. Being able to understand the mechanics of biological tissues will be able to offer insight into the designs and functionality seen in nature and provide information to help predict the performance.

The primary focus of this chapter is to quantify the mechanical properties taken from exploratory experiments of the midline cartilage, network cartilage, and matrix tissue for use in finite element analysis. The results presented in this section will be used in the material models for various boundary conditions. A variety of experimental and characterization techniques are implemented to quantify material properties and describe the material components within the paddlefish rostrum.

2.2 Materials

Live specimens of *P. spathula* were contained at the Environmental Laboratory of the U.S. Army Engineer Research and Development Center (ERDC). The paddlefish were anesthetized and euthanized before the rostrum was amputated according to the ERDC Institutional Animal Care and Use Committee (IACUC) guidelines (Protocol #EL-6009-2011-5), which encompasses the National Institutes of Health Guide for Care and Use of Laboratory Animals. Cartilage samples were stored in a phosphate-buffered saline (PBS) solution to maintain hydration or native osmolarity. The rostrum for this study were obtained from adult paddlefish ranging from 700-800 mm long. The materials of interest in this study include the midline cartilage, the harder network cartilage, and the matrix tissue which is comprised of the remaining materials within the rostrum. Figure 2.1 shows a 3-D model depicting the structure and position of the midline cartilage, network cartilage, and matrix tissue.

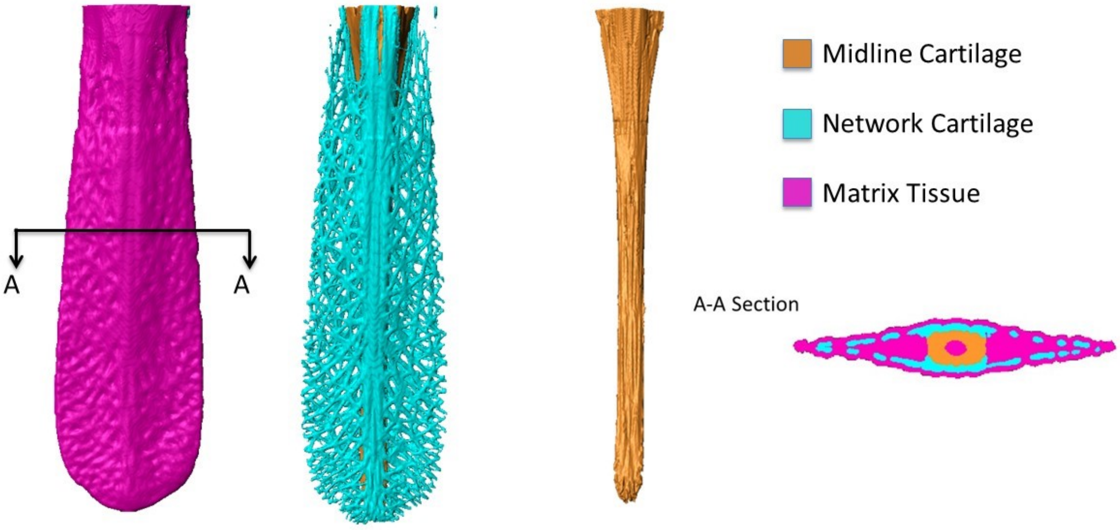

Figure 2.1 Rostrum model and constitutive materials.

2.3 Midline Cartilage

2.3.1 Methods

2.3.1.1 Low-Strain Rate Compression and Tension

The midline cartilage is a long section of cartilage that spans the length of the rostrum and is sandwiched between the network cartilage, which is displayed in Figure 2.1. For low-strain rate compression and tension testing, the midline cartilage was isolated from the rest of the rostrum, and samples from different sections along the length of the rostrum were obtained to determine if the stress-strain behavior of the midline cartilage of the rostrum was spatially dependent. Figure 2.2 shows samples that were extracted from three medial-line locations, designated as M1, M2, and M3. M1 is near the tip of the rostrum while M3 is located towards the cranial end of the fish.

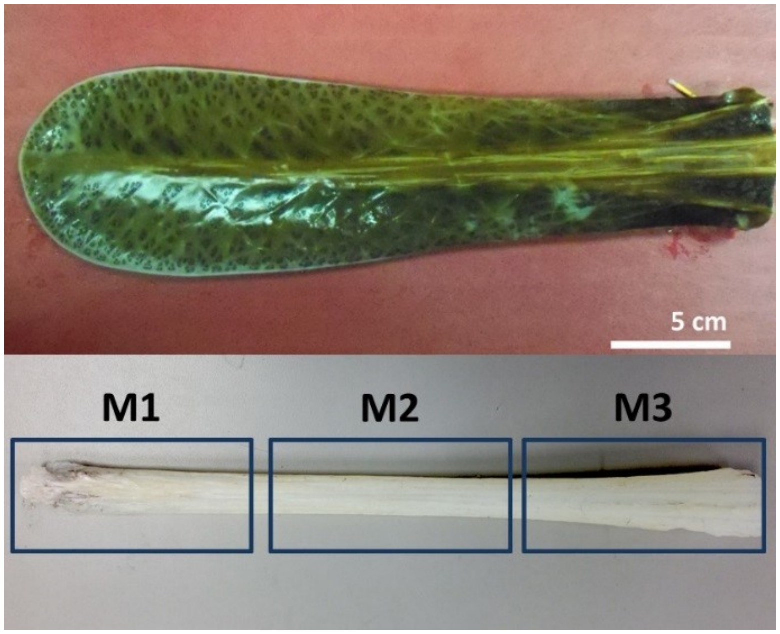

Figure 2.2 Paddlefish rostrum and the midline cartilage.

(top) Paddlefish rostrum. (bottom) Isolated midline cartilage with the location of the samples for low-strain rate compression testing along the paddlefish rostrum

For sample extraction hole-saw bits were used on a drill press down the length of the rostrum. Extraction began towards the cranial end of the fish at M3. A total of seven samples from each medial location was taken, and all samples were extracted from the same rostrum. Each sample was stored in PBS and stored in ice for transport to the Center for Advanced Vehicular Systems (CAVS) at Mississippi State University. Samples were tested within twenty-four hours, and before testing, samples were removed from ice and allowed to return to room temperature. Each sample had a diameter of 5.05±0.11 mm (average ± one standard deviation) and a diameter-height aspect ratio of 1.74±0.15. A scalpel was used to reach this aspect ratio and to ensure a smooth, flat testing surface. The diameter and height was recorded for each sample. The compression tests were done using the INSTRON 5882 (Instron, MA, USA) using a 1 kN load cell. Each sample was preloaded with approximately 4N of force to ensure complete contact on the top and bottom of each sample. Quasi-static compression tests were conducted at a constant strain rate of ~0.01/s. The data was recorded using the INSTRON Bluehill software. Using the load-displacement data, the true stress-strain curves for each test was produced. The true stress-strain data from each sample was input imported to a MATLAB software designed to interpolate an average stress-strain curve with a standard deviation for a set of samples. This procedure was repeated for each set of samples in M2 and M3.

Low-strain rate tension tests performed on the cartilage were performed to reveal the effect of stress state on the material. Dog-bone shaped tension samples were extracted from the midline cartilage. The skin and network cartilage were removed to expose the midline cartilage. Seven dog-bone shaped specimens were cut from two different rostrum lengths. The gage length of each specimen was 15.94±1.08 mm, gage width of 5.75±0.79 mm, and a thickness of 2.85±0.47 mm. The dog bone shaped tension samples were stored in PBS in a container of ice overnight and were then allowed to reach room temperature before testing. The INSTRON 5882 was used with a 5 kN load cell and tension grips. For each test, a sample was fastened to the upper grip, then lowered to the lower grip where it could be fastened as well. Each test was performed at a constant strain rate of ~0.01/s until failure of the sample. Load and displacement were recorded using the Bluehill software. Each experiment was additionally recorded on video for further analysis. The data for each test was exported to an Excel spreadsheet, and the true stress-strain data of each test was compiled to create an average stress-strain curve with standard deviation.

2.3.1.2 High-Strain Rate Compression

High-strain rate testing was also performed using the split-Hopkinson pressure bar method. The split-Hopkinson pressure bar is comprised of a striker bar, incident bar, and transmitted bar. A gas gun fires the striker bar into the incident bar, and a single stress wave is delivered to the specimen. Strain gauges on the incident and transmitted bars capture the reflected and transmitted stress wave, which can then be used to characterize the stress-strain behavior. A diagram for the split-Hopkinson bar method is shown in Figure 2.3. Testing was done with a sample size of N=3. Midline cartilage samples with diameters of 16.27±0.24 mm and diameter-height ratio of 2.83±0.25 mm were bored using circular drill bits and a drill press and kept hydrated. The dimensions of each sample was recorded before each test. Each sample was placed between the polycarbonate incident and transmission bars so that contact on both sides held the sample in place. The test was run at a strain rate of ~100/s and was recorded using a Phantom v710 high-speed camera. The experimental data gathered from the high-strain rate testing is presented as true stress-strain data.

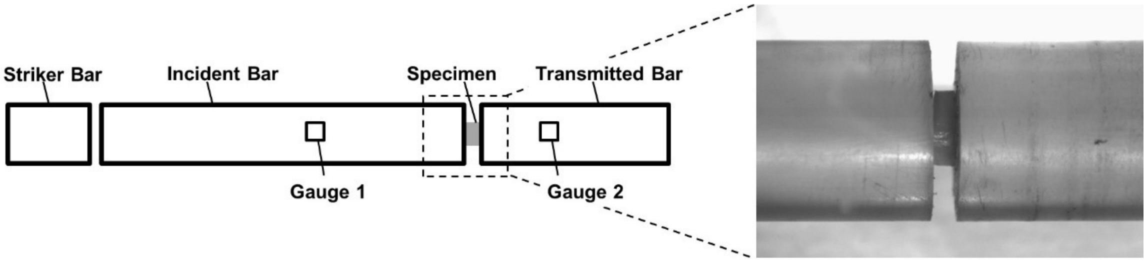

Figure 2.3 Split-Hopkinson bar compression test setup.

2.3.1.3 Histological Study

Cartilage is typically classified into three categories: elastic cartilage, fibrocartilage, and hyaline cartilage. A histological study was performed on the midline cartilage to view the microstructure of the midline cartilage and to provide further insight into determining its cartilage classification. The midline cartilage was sectioned along the length of the rostrum, and samples were cut in transverse, horizontal, and sagittal directions (see Figure 2.4) to view the spatial dependence of the cartilage cell structure. Similar to the effect of various etchants on polished metal samples, different stains affect the histological results and will attempt to highlight certain aspects. Cartilage slides were stained with hematoxylin and eosin, as well as alcian blue, in an attempt to view the possible presence of collagen fibers within the midline cartilage. Furthermore, image quantification was performed on the histological specimens to determine the nearest neighbor distance, number density, area, and area fraction.

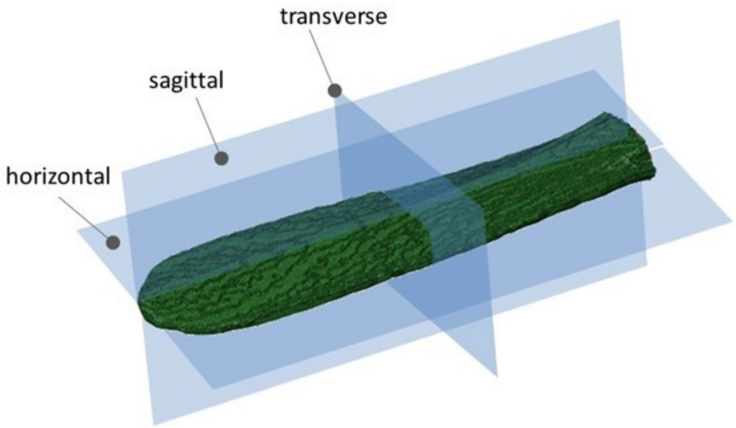

Figure 2.4 Transverse, sagittal, and horizontal planal directions for the histological study on the midline cartilage.

2.3.2 Results

2.3.2.1 Low-Strain Rate Results

Figure 2.5 shows the average compressive stress-strain curve from three different locations on the paddlefish revealing that there is no constitutive behavior difference for the midline cartilage. The error bars on each curve denote the standard deviation. M1, M2, and M3 represent different locations along the midline cartilage, where M1 is closer to the free end of the rostrum, M2 is the middle of the rostrum, and M3 close to the cranial end (recall Figure 2.2). Each location has a sample size of N=7.

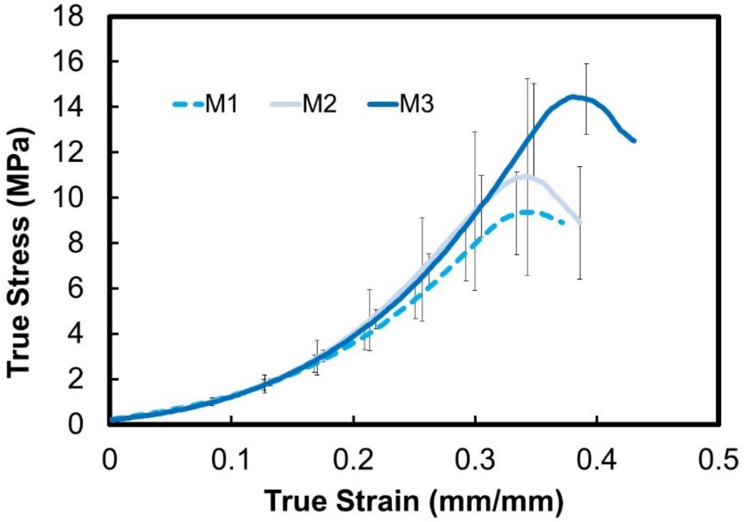

Figure 2.5 Low-strain rate compressive stress–strain behavior of the midline cartilage from different locations along the paddlefish rostrum. Sample size of N = 7 for each of spatial locations M1, M2 and M3

Figure 2.6 displays the stress state dependence of the midline cartilage in compression and tension. Because the low-strain rate compression results show that the cartilage is not spatially dependent, the compressive stress-strain behavior from the three different locations seen in Figure 2.5, were averaged into one compressive stress-strain curve. The stress-strain response of the midline cartilage is higher in compressive stresses than tensile stresses and shows a 68% reduction from compressive to tensile tests. The average ultimate compressive stress is 11.34±3.10 MPa and the average ultimate tensile stress is 3.62±0.62 MPa. The elongation to failure for the tension test was 0.28±0.03 mm/mm.

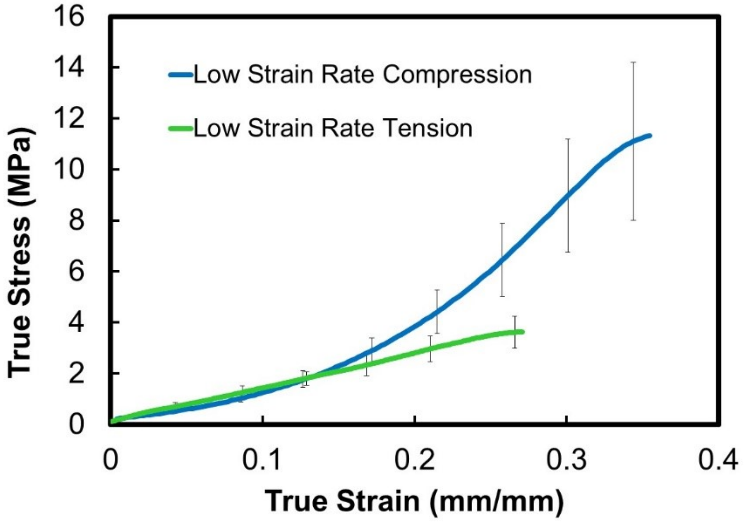

Figure 2.6 Low-strain rate comparison of midline cartilage of the paddlefish in tension and compression.

2.3.2.2 High-Strain Rate Results

Figure 2.7 shows the stress state and strain rate dependence of the midline cartilage. In terms of stress state, the stresses are greater for compression than for tension at the same strain level. Hence the midline cartilage has a higher ultimate strength under compression than tension. For compression, the stresses are greater for higher strain rates. The average ultimate compressive stress for high-strain rate is 25.07±10.86 MPa, a 120% increase from quasi-static tests.

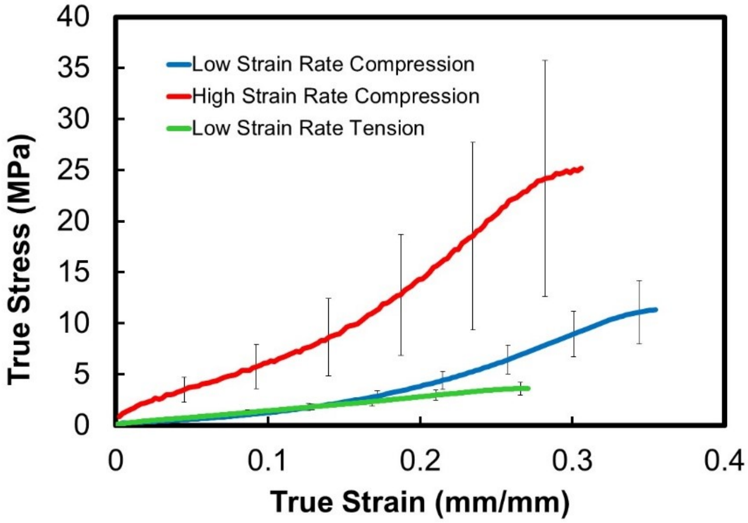

Figure 2.7 Stress state and strain rate dependence of the midline cartilage of the paddlefish rostrum.

2.3.2.3 Histological Study

Histological results show that there is no spatial dependence or orientation dependence on the midline cartilage. Furthermore, with no evidence of collagen fibers or elastin from the alcian blue stain, the structure of the cartilage mostly resembles hyaline cartilage. Figure 2.8 shows representative samples for both staining techniques from this study.

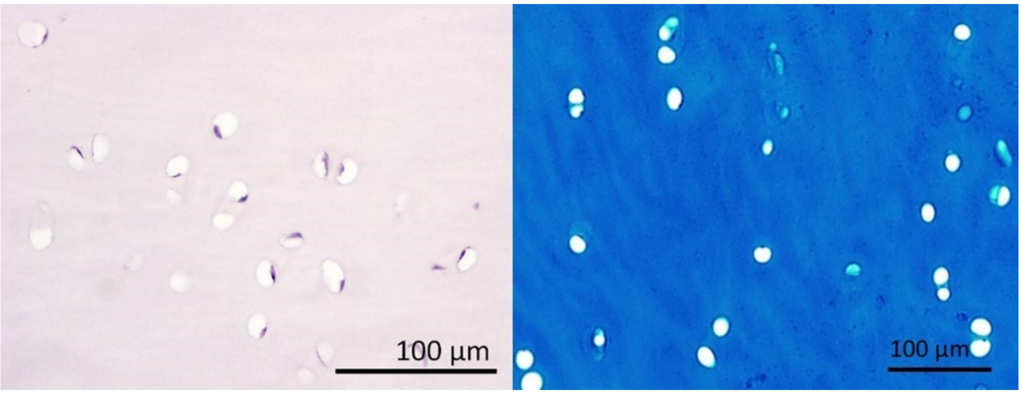

Figure 2.8 Representative image from the histological study of the midline cartilage of the rostrum.

Samples were taken in the transverse direction and were stained with (left) hematoxylin and eosin and (right) alcian blue.

The cells within the cartilage were also quantified. Using ImageJ (20)analysis software, the nearest neighbor distance was found to be 53.0±29.6 µm. The number density was 100.6±4.8/mm^2. The cell area and area fraction were 133.2±42.8 µm^2 and 1.29±0.06 %, respectively.

2.3.3 Discussion

Cartilage exists in different forms. Hyaline cartilage provides stiff and somewhat flexible support. It reduces friction in bony surfaces and can be found in the nose and rib cage area. Elastic cartilage also provides support, but is much more flexible, containing collagen fibers that allow it to undergo distortion without damage. Elastic cartilage is present in the ear. Fibrocartilage has a dense arrangement of fibers that are oriented in a specific manner. Compared to hyaline and elastic cartilage, fibrocartilage has a greater resistance to deformation under high stresses. Fibrocartilage also helps prevent bone to bone contact and is present in intervertebral discs. Though a large amount of previous research has been done on the mechanics of cartilage, the results reported here are among the first to explore the effect of different stress states as well as strain rates ranging from ~0.01/s to ~100/s for cartilage.

Comparing this study to previous research done, the results from the low-strain rate compression tests presented here are similar to those done by Porter and Long (2010) (21) in the compression of the cartilage found in the vertebrae of sharks. Particularly, the initial concave stress-strain behavior and the ultimate strength of the paddlefish cartilage are comparable to the study done by Porter and Long (2010). Additionally, Yamada (1970) reported work on the mechanical properties of different kinds of human tracheal cartilage (22). The average ultimate strength observed in Yamada's data for specimens ranging from 10-89 years of age was 2.35 MPa and ranged from 3.53 MPa (10-29 years old) to 1.67 MPa (70-89 years old). Furthermore, Figure 2.8 shows that the low-strain rate tension test results (seven tests from different locations along the midline cartilage) from this study compare well with Yamada's low-strain rate results for tracheal cartilage. Yamada's data seen in Figure 2.9 displays the strength of tracheal cartilaginous tissue from people between the ages of 20-29. The average ultimate tensile strength from the tracheal cartilage from that age group was 3.53 MPa which is a 2.48% difference compared to the ultimate strength observed in this paper. The elongation to failure was 0.27 mm/mm which is a 3.57% difference from the 0.28 mm/mm elongation to failure from the tensions tests in this study.

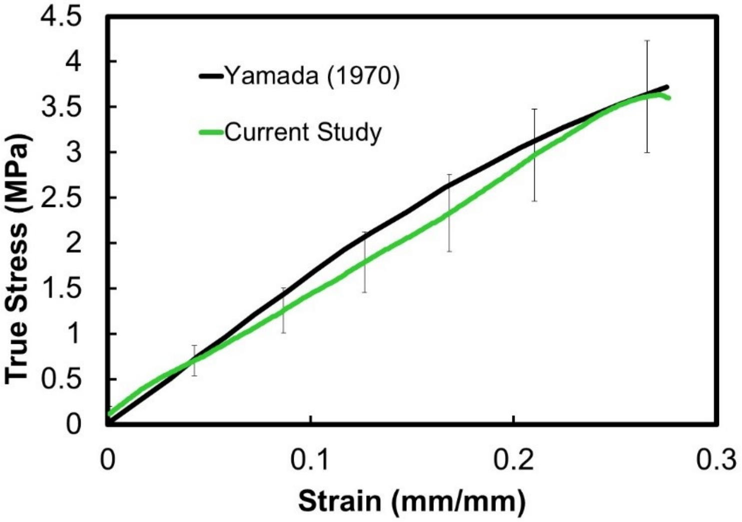

Figure 2.9 Stress-strain behavior comparison for low-strain rate tension of cartilage. Midline cartilage of the paddlefish was compared with the human tracheal cartilage studied by Yamada (22).

The histological study shows that the midline cartilage cellular structure closely resembles that of hyaline cartilage. Figure 2.10 compares this cartilage to other types of cartilage. Note the absence of collagen fibers in the paddlefish cartilage which are evident in the elastic cartilage (dark pink) and the fibrocartilage (dark grey). Furthermore, the tracheal cartilage, seen in the study done by Yamada (Figure 2.9), is also a type of hyaline cartilage. Also, there was no histological difference based on orientation or sample location, supporting the experimental results that the stress-strain behavior is indifferent of location (Figure 2.5). The image quantification can also provide insight into the age of the paddlefish. Research done by Stockewell (23) and Barbero *et al.* (24) have shown an inverse relationship of the number of cells in articular cartilage (a type of hyaline cartilage) with the age of the sample.

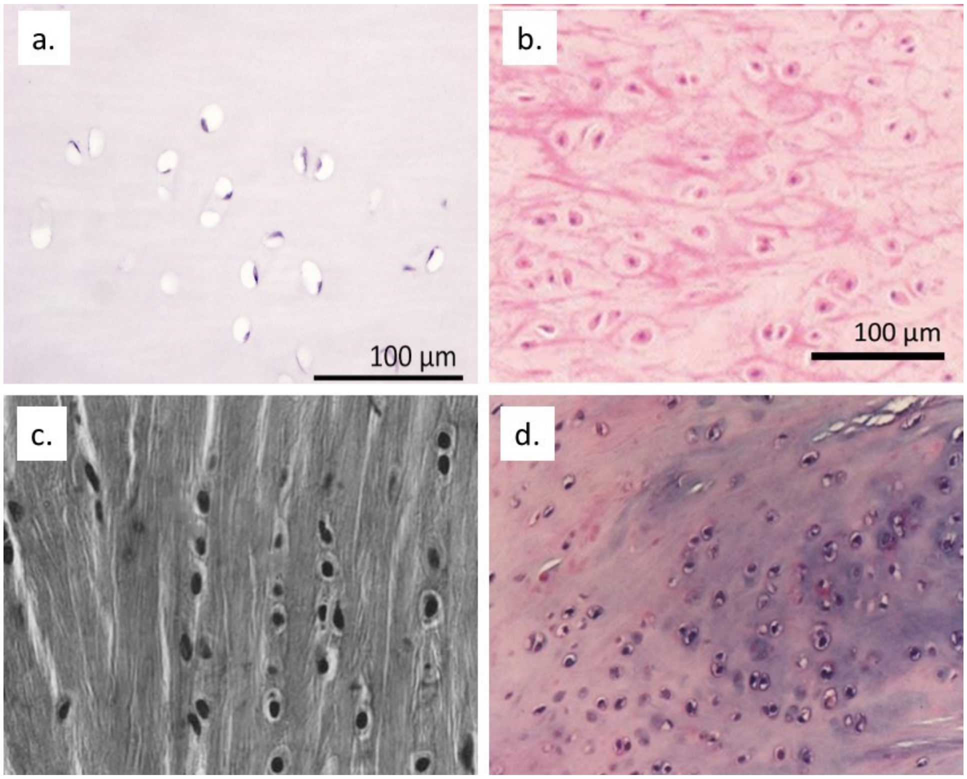

Figure 2.10 Comparison of the paddlefish cartilage with other types of cartilage. (a.) Paddlefish cartilage (b.) elastic cartilage (25) (c.) fibrocartilage obj. mag. 300x (26) (d.) hyaline cartilage obj. mag. 24x (27)

From the results shown in Figure 2.6, the rostrum cartilage has a different stress-strain behavior under different stress states. This tension-compression asymmetry is caused by the collagen content and water content, which determines its compressive properties (28)(29). Furthermore, the difference in stress-strain behavior between tension and compression seen in the rostrum cartilage has been observed in previous research dealing with cartilage found in human joints (30). Additionally, the results in this paper show that the average ultimate tensile strength of the midline cartilage is 31.9% of the average ultimate strength seen in compression.

Figure 2.11 shows the progression of a low-strain rate tension test from no elongation until right before the specimen fails. As the specimen undergoes tensile stresses, the cartilage elongates until enough stress is applied and a crack is formed in the cartilage. Once introduced, the crack will continue to propagate until it eventually grows across the entire cross section, causing failure of the specimen. This pattern was observed in each tensile experiment. The specimen seen in Figure 8 had a crack initiate at a strain of 0.23 mm/mm and had an elongation to failure at 0.28 mm/mm.

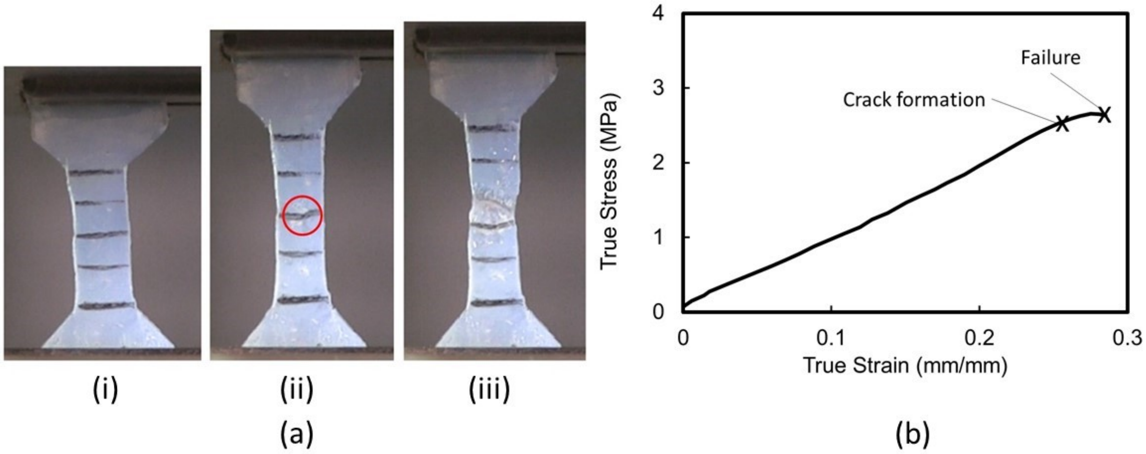

Figure 2.11 Crack formation and failure of the midline cartilage during low-strain rate tension testing. Low-strain rate tension test with (i) no elongation, (ii) formation of a crack, and (iii) crack extension right before failure. (b) Stress-strain curve displaying the locations and strains at which the crack started and the specimen failed.

2.4 Network Cartilage

2.4.1 Nanoindentation Procedures

One feature of the paddlefish that is unique in nature is the network cartilage. From Figure 2.1, the network cartilage is an extension of the cartilage skeletal structure that encompasses the midline cartilage, extends outward away from the cranium, and branching out to the edges of the rostrum. The matrix tissue surrounds the network cartilage and is also situated between the branched sections of the network cartilage (see A-A section of Figure 2.1). Though the network cartilage seems like one continuous piece, like a tree trunk with its extending branches, it is comprised of small star-shaped structures joined by connective structure seen in Figure 2.12.

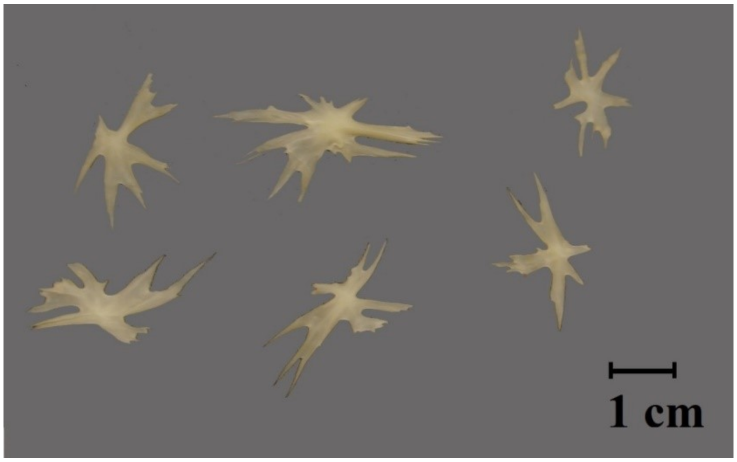

Figure 2.12 Network cartilage structures.

Mechanical properties were taken from nanoindentation experiments performed by Allison *et al.* (31) on the network cartilage. Similar to the midline cartilage, samples were taken from the cranial end, middle, and tip of the rostrum to explore the possibility of spatially dependent material properties. Figure 2.13 shows the samples taken along the middle (M1, M2, and M3) and left side (L1, L2, and L3) of the network cartilage.

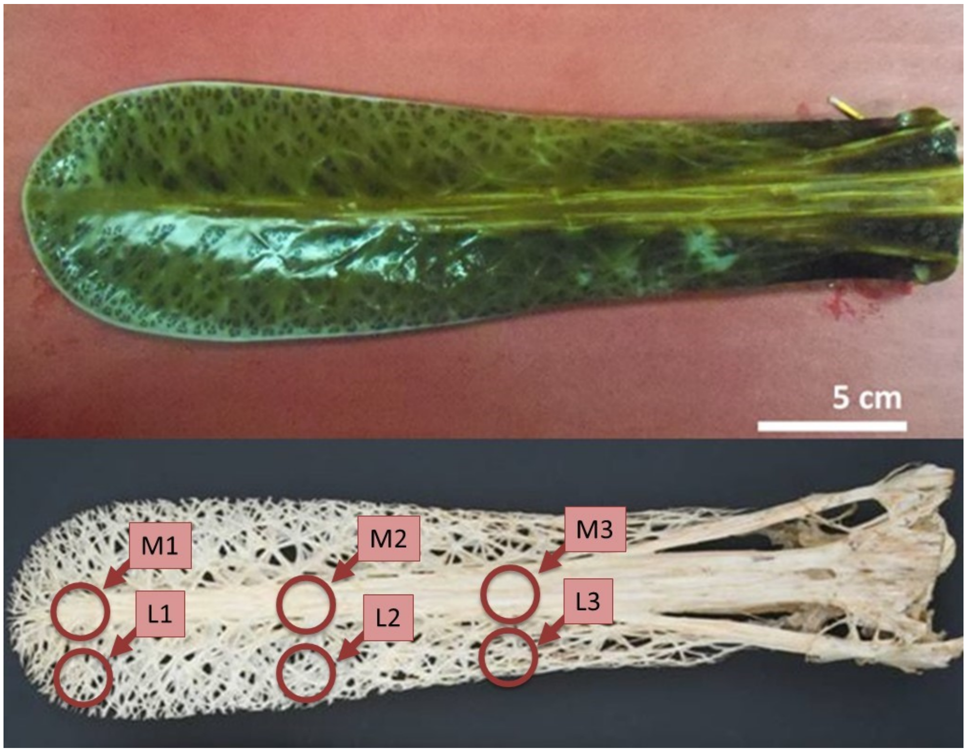

Figure 2.13 Network cartilage from the rostrum. (top) Paddlefish rostrum (bottom) Isolated network cartilage showing the location of network cartilage samples.

Network cartilage was removed the rostrum, mounted in epoxy resin, and polished using silicon carbide abrasive discs ranging from 200 to 1200 grit. An Agilent G200 nanoindenter (Englewood, CO, USA) was used to indent the specimens with a load of 50 mN. The data was analyzed using standard routines (Oliver and Pharr, 1992) (32) to determine the hardness, H. The hardness for each test is defined by Eq. (2.1):

$$H = \frac{Pmax}{A} \tag{2.1}$$

where P_{max} is the peak load, and A is the projected indentation area indenter. The reduced Young's modulus is calculated during the unloading phase and is described by Eq. (2.2):

$$E_r = \frac{1}{2}\sqrt{\frac{\pi}{A}}\frac{dP}{dh} \tag{2.2}$$

where *dP/dh* is the slope of the unloading curve. The modulus of the material, E, is found using Eq. 2.3:

$$\frac{1}{E_r} = \frac{(1-\nu^2)}{E} + \frac{(1-\nu_i{}^2)}{E_i} \tag{2.3}$$

2.4.2 Fourier Transform Infrared Spectroscopy

Fourier transform infrared spectroscopy (FT-IR) data was also taken from Alison *et al.* (31). FT-IR was performed on network cartilage samples using a Nicolet 6700 FT-IR spectrophotometer (Waltham, MA, USA) in attenuated total reflectance (ATR) mode with a single-bounce diamond-ATR crystal. Infrared spectra between 4000 and 650 cm^{-1} were collected at a resolution of 4 cm^{-1} using128 scans.

2.4.3 Nanoindentation Results

Nanoindentation results for hardness and modulus are shown below in Figures 2.14 and 2.15. Along the medial line, the material properties did not show any spatial dependence, with an average hardness and modulus of 0.44±0.01 GPa and 12.06±0.68 GPa, respectively. However, spatially dependent material properties were observed along the side of the rostrum where the hardness increased from 0.32 to 0.39 GPa toward the cranial end. The modulus also showed a spatial dependence, with a positive parabolic response with the highest value reported at the cranial end.

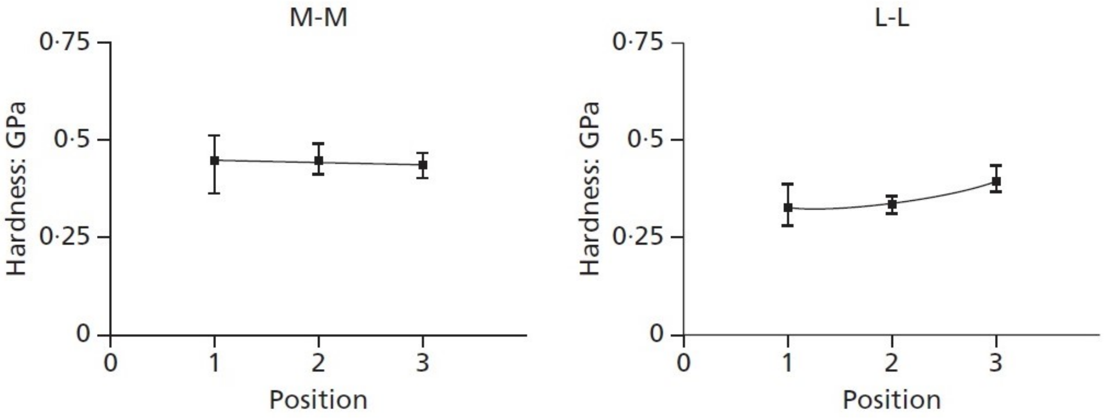

Figure 2.14 Network cartilage hardness results from nanoindentation. Refer to Figure 2.11 for position reference.

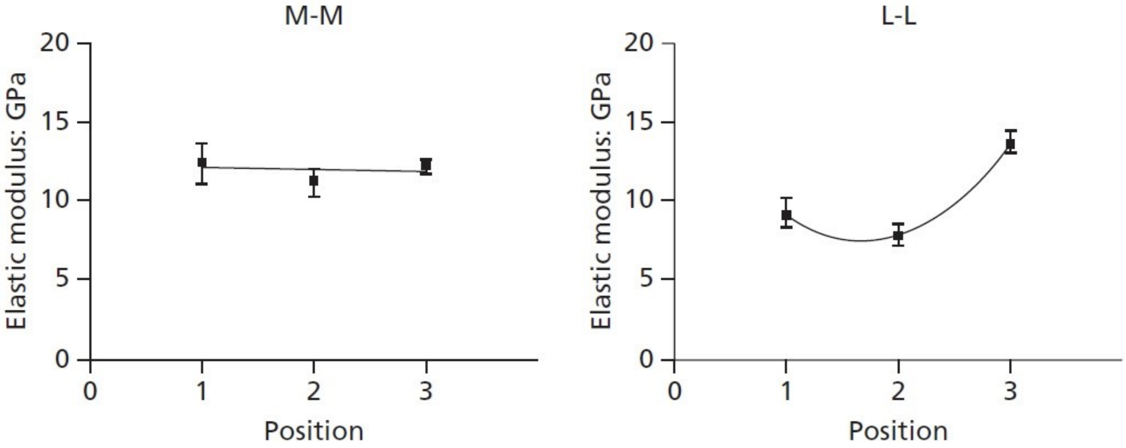

Figure 2.15 Network cartilage modulus results. Refer to Figure 2.11 for positions reference.

2.4.4 Fourier Transform Infrared Spectroscopy Results

Figure 2.16 shows the spectra for the network cartilage. The main functional groups that are present in the network cartilage are amide, carboxylic, phosphate, and carbonyl.

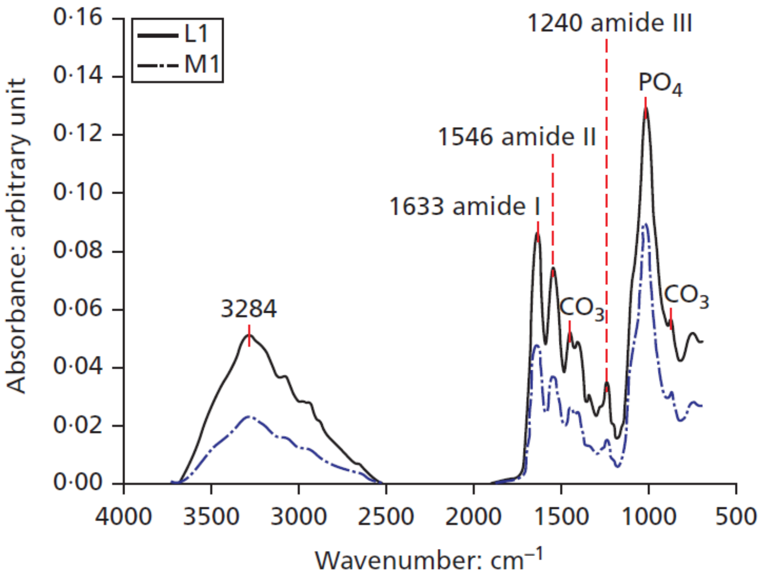

Figure 2.16 Fourier Transform Infrared Spectroscopy results for the network cartilage of the paddlefish.

2.4.5 Discussion

The FT-IR results show consistent characteristic peaks between along the medial line and the side of the network cartilage. The peaks and characteristics seen in the FT-IR results are similar to FT-IR results seen in shark cartilage (33)(34). Sharks are very similar to paddlefish in that they both not only have Ampullae of Lorenzini (electrosensory pores) but they also have skeleton made of cartilage.

Unlike the midline cartilage and the matrix tissue (seen in the following section), the network cartilage exhibits spatially dependent mechanical properties. The FT-IR results do not suggest a significant difference between the two, so additional characterization techniques may need to be done to account for this phenomenon. The morphology and the growth of the rostrum as the paddlefish ages may provide insight into the differences in mechanical properties seen in the network cartilage. A study quantifying the microstructure of the network cartilage can quantify the age. Research performed on human bone has shown a difference in the microstructure of bone as a function of age (35)(36)(37). McCalden *et al.* (37) showed that mechanical properties could be estimated by porosity and density, which were related to donor age. Similar results were seen by Wang *et al*.(38). The bone porosity had a direct relationship with the age of the bone and an inverse relationship to the elastic modulus. Performing similar characterization techniques should present useful information into the age of the network cartilage and how it forms.

Cartilage can exist as elastic cartilage, hyaline cartilage, and fibrocartilage, but it can also become calcified (mineralized) resulting in a much stiffer cartilage and a material that resembles bone (39). The skeleton of the paddlefish, as well as sharks, is comprised of this type of cartilage (29)(31). Compared to bone, calcified cartilage is more flexible and can also reduce the skeleton's weight, saving energy as the fish swims (42). The calcified cartilage of the network cartilage also exhibits similar material properties to that of bone. Mechanical testing data from Wang *et al.* (38) observed an elastic modulus of bone ranging from 10.7 – 11.5 GPa.

2.5 Matrix Tissue

2.5.1 Compression Testing Procedures

The matrix tissue constitutes the remaining tissues in the rostrum. This includes the tissue that surrounds and is in between the network cartilage seen in Figure 2.1 The compression test methods on the soft tissue are similar to the compression test methods used for the midline cartilage. These samples are cut from the sides of a using a hole-saw bit on a drill press. Once these samples were extracted from the rostrum, the outer skin layer and network cartilage on both sides of the soft tissue were removed using a scalpel. The resulting samples had diameters of 10±0.17 mm with diameter-height aspect ratios of 1.5±0.13 mm. These samples were tested using the INSTRON 5882 with a 1 kN load cell and 3” platens. The dimensions of each sample was recorded and input into the INSTRON Bluehill software. Each sample was placed on the lower platen before each test. Once the sample was on the lower platen, the upper platen was lowered until a preload of 4 N was applied to ensure complete surface contact on the top and bottom of each sample with the platens. Each test was run at a constant strain rate of 0.01/s until the load reached ~400 N. Load and displacement was recorded using the Bluehill software where Engineering stress and strain, as well as True stress and True strain could be calculated. This data was exported to an Excel spreadsheet where stress-strain curve could be reduced and analyzed. The stress-strain data for each sample was imported to a MATLAB program designed to interpolate an average stress-strain curve for a set of data

2.5.2 Compression Test Results

The average stress-strain curve from each location data set was compared and analyzed to determine if location on the rostrum affected the material properties of the matrix tissue in compression. Similar to the midline cartilage, a spatial dependence on the stress-strain behavior was not observed, and Figure 2.17 shows the average stress strain behavior of the matrix tissue.

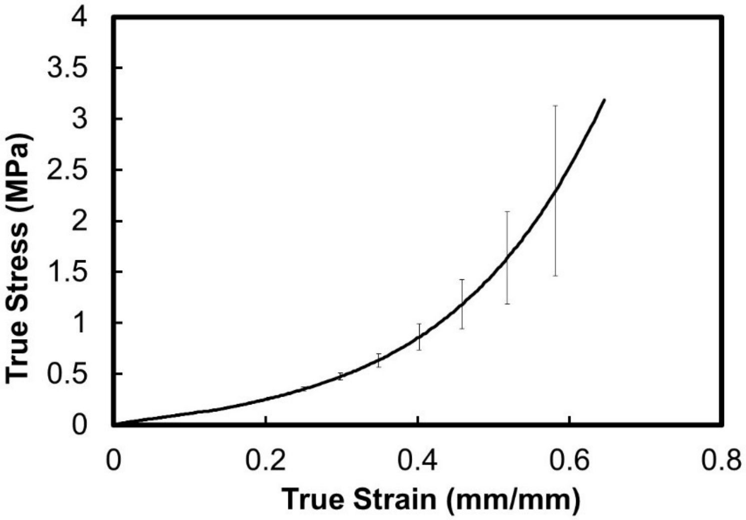

Figure 2.17 Low-rate compression of the matrix tissue.

2.5.3 Discussion

Results for the matrix tissue are similar to results seen in other soft tissues, including brain, fascia, and other connective tissues (43)(44)(45). In particular the nonlinear behavior seen within the stress-strain curve is common within soft tissues. The motivation for lumping the remaining tissue into the matrix tissue stems from the computed tomography images (seen in the next chapter). The results seen in this chapter for the midline cartilage, network cartilage, and matrix tissue will be used for the material model, which is also found in the upcoming chapter.

CHAPTER III

MODELING AND FINITE ELEMENT ANALYSIS OF THE PADDLEFISH

3.1 Introduction

A motivation for this study stems from the unique geometry of the network cartilage observed within the rostrum. The modeling and finite element analysis will provide an exploratory study investigating the stress distribution within the rostrum from an array of boundary conditions.

3.2 Methods

3.2.1 Three-Dimensional Model of the Rostrum

This chapter focuses on the modeling and finite element analysis of the rostrum using the results taken from the previous chapter. Before any type of analysis can be conducted, a three-dimensional model and mesh is constructed. To produce the model, several rostrum were extracted from live specimens to be used the next day with computed tomography (CT). CT scans were performed on the paddlefish rostrum using a General Electric Phoenix v|tome|x. Scans were done with an initial pixel resolution of 0.22 mm. Figure 3.1 shows an example of a Computed Tomography (CT) scan of the top portion of the rostrum. Note that denser materials are shown as darker colors in the CT scan, which allows the CT scan to differentiate between the midline cartilage, network cartilage, and the matrix tissue.

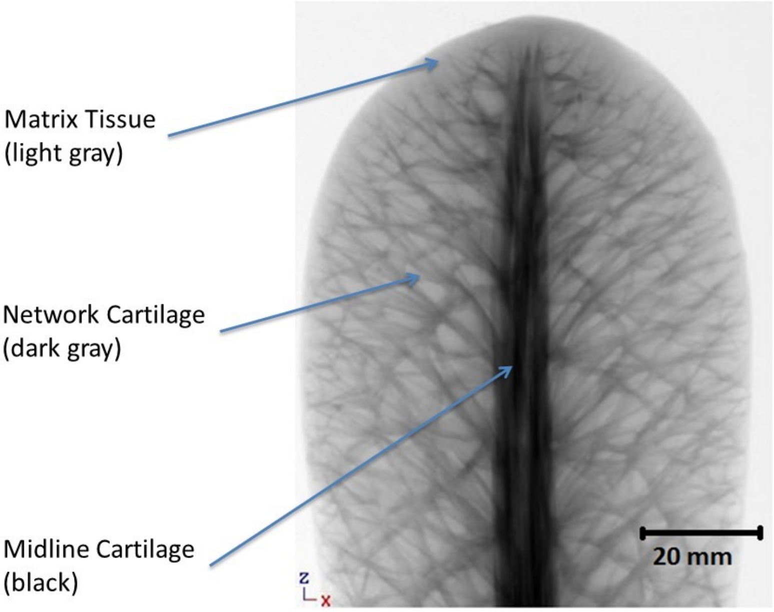

Figure 3.1 Computed tomography of the upper section of the paddlefish rostrum. Computed tomography showing the different constitutive materials of the paddlefish.

Multiple scans were taken of each section of the rostrum at different angles as the section underwent a complete rotation. Each section contained a total of 600 DICOM Images, which were then exported and stacked to create a three-dimensional model of a rostrum section. Because of the size of the rostrum, three different sections were scanned, aligned, and then reconstructed to create a complete model of the entire rostrum. Figure 3.2 shows the alignment of the multiple scans that were required to generate the entire rostrum, and Figure 3.3 shows the changes in the cross section from the reconstructed model.

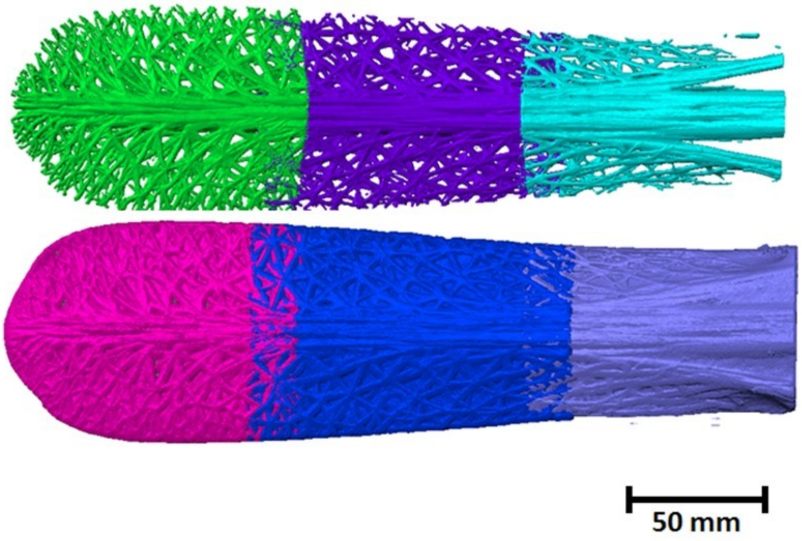

Figure 3.2 Model construction of the rostrum taken from multiple computed tomography scans.

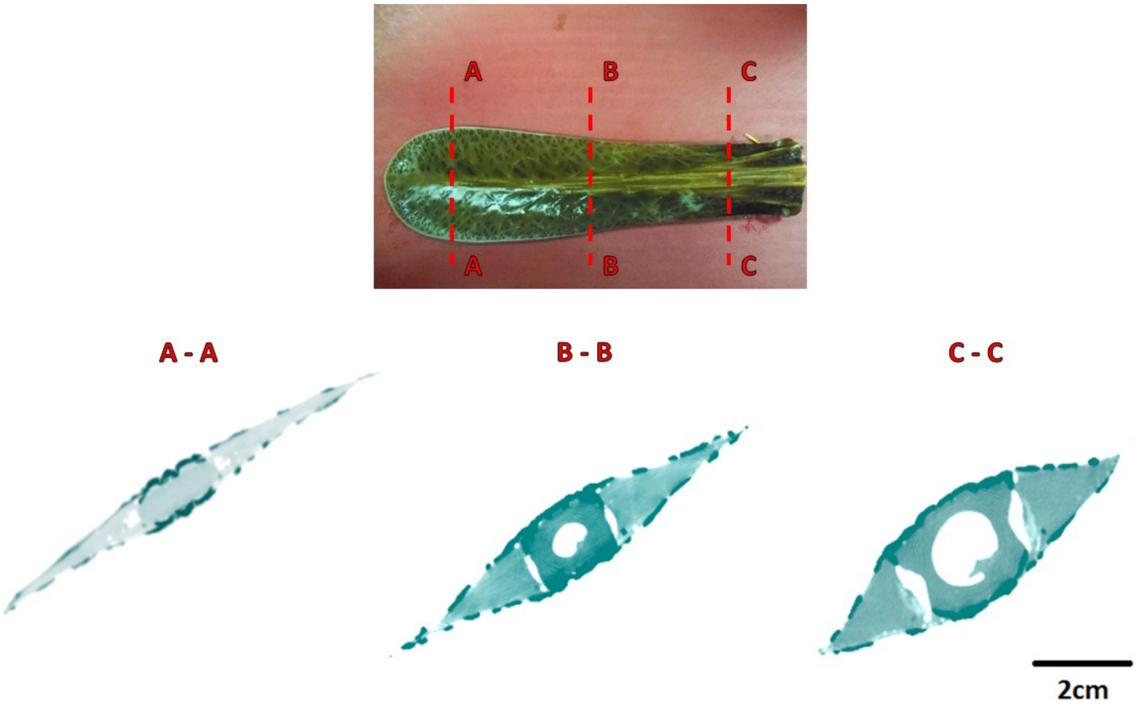

Figure 3.3 Change in cross sections along the length of the rostrum.

The DICOM images were then transferred to ScanIP (Simpleware Ltd. Exeter, UK) for 3D model construction. ScanIP allows for the segmentation of different materials and has been used to model the segmentation of human bone, bone marrow, blood vessels, connective tissue, muscle, and skin (46). Segmentation is performed using a density threshold, where a specific density range distinguished by CT scans will be assigned a specific notation. In this case, the rostrum will be segmented into three different materials: the network cartilage, midline cartilage, and matrix tissue. Because the density of the remaining materials could not be differentiated, the remaining tissue was consolidated into the ‘matrix tissue’. Figure 3.4 shows the segmentation of the materials within ScanIP. Finally, an orphan mesh was exported from ScanIP for use in abaqus simulations. The initial pixel resolution of 0.55 mm produced a mesh consisting of 5.6 million total elements. The rostrum was resampled to a voxel size of 0.95 mm, resulting in a final mesh with 1.42 million elements.

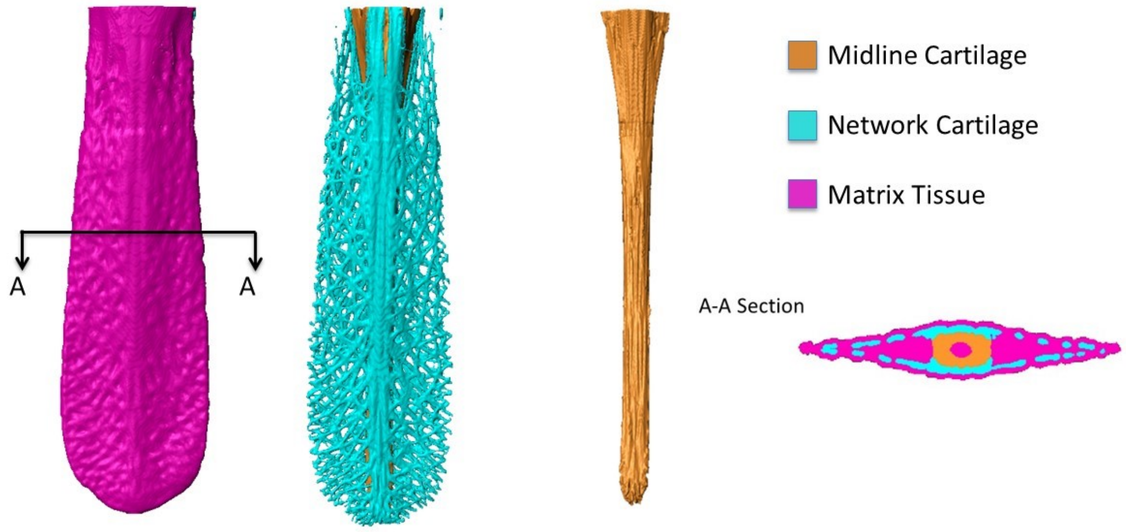

Figure 3.4 Rostrum model and constitutive materials.

Once the model was created, the geometry of the rostrum was analyzed. ScanIP and BoneJ (47) were used to study the volume fraction of the materials, as well as the changes in area fraction of the materials along the length of the rostrum. Additionally, BoneJ was utilized to determine the moment of inertias of the cross-sectional slices obtained from ScanIP.

3.2.2 Hyperelastic Model

Once the mesh was created, a material model for the midline cartilage, network cartilage, and matrix tissue was needed to describe the stress-strain behavior of each material. Because of its ability to capture nonlinear elastic regions, a hyperelastic model was chosen to model the stress-strain behavior of the midline cartilage and matrix tissue.

Additionally, hyperelastic models have been utilized to model a number of different biological materials including a cartilage, tendon, brain, liver, and spinal cord (48)(49)(50). A fitting routine within abaqus was used to determine the material model constants that best fit the experimental data taken from Chapter 2.

In particular, the Ogden hyperelastic model was utilized (51)(52). Deformations are defined in the form of the following,

$$x_1 = \lambda_1 X_1 , \qquad x_2 = \lambda_2 X_2 , \qquad x_3 = \lambda_3 X_3 \tag{3.1}$$

where (X_1 , X_2 , X_3) are rectangular Cartesian coordinates of a material in an unstressed reference configuration, (x_1, x_2, x_3) characterize the material after deformation, and $(\lambda_1, \lambda_2, \lambda_3)$ are positive constants. For a hyperelastic model, the strain-energy function, W, depends symmetrically on $\lambda_1, \lambda_2, \lambda_3$, i.e.

$$W(\lambda_1, \lambda_2, \lambda_3) = W(\lambda_1, \lambda_3, \lambda_2) = W(\lambda_2, \lambda_1, \lambda_3) \tag{3.2}$$

For an incompressible material, the principal stretches satisfy the constraint

$$\lambda_1 \lambda_2 \lambda_3 = 1 \tag{3.3}$$

For the Ogden material model, the strain-energy function is defined by principle stretches as:

$$W(\lambda_1, \lambda_2, \lambda_3) = \sum_{i=1}^{N} \frac{\mu_i}{\alpha_i} ({\lambda_1}^{\alpha_i} + {\lambda_2}^{\alpha_i} + {\lambda_3}^{\alpha_i} - 3) \tag{3.4}$$

The principal Cauchy stresses $(\sigma_1, \sigma_2, \sigma_3)$ are related to the stretches through W by the equation

$$\sigma_i = \lambda_i \frac{\partial W}{\partial \lambda_i} - p \tag{3.5}$$

where p is a Lagrange multiplier associated with the constraint in Equation 3 and can be assumed to be zero for an incompressible material.

Abaqus simulations were performed to show the accordance of the material model with the characteristic behavior of the midline cartilage and matrix tissue. Single element simulations were performed in tension and compression to verify the ability of the model to capture the stress state dependence of the material. An Ogden hyperelastic model with N=3 was used (refer back to Equation (3.4)), and Table 3.1 and 3.2 shows the single set of constants used for the material model of the midline cartilage and matrix tissue for all simulations.

Table 3.1 Constants used for the Ogden hyperelastic model of the midline cartilage.

i	**μ_i**	**α_i**
1	-1196.32	-0.00765
2	622.06	0.39905
3	577.91	-0.54259

Table 3.2 Constants used for the Ogden hyperelastic model of the matrix tissue.

i	**μ_i**	**α_i**
1	-1.28772136	4.93387993
2	1.81071911	5.68884248
3	-0.0927071	-4.51736587

Figure 3.5 and 3.6 show that the results of the single element simulations using an Ogden hyperelastic model capture the behavior of the midline cartilage and matrix tissue very well. For the midline cartilage, a single set of constants were able to capture the stress-state dependence seen from the experimental results (recall Figure 2.6).

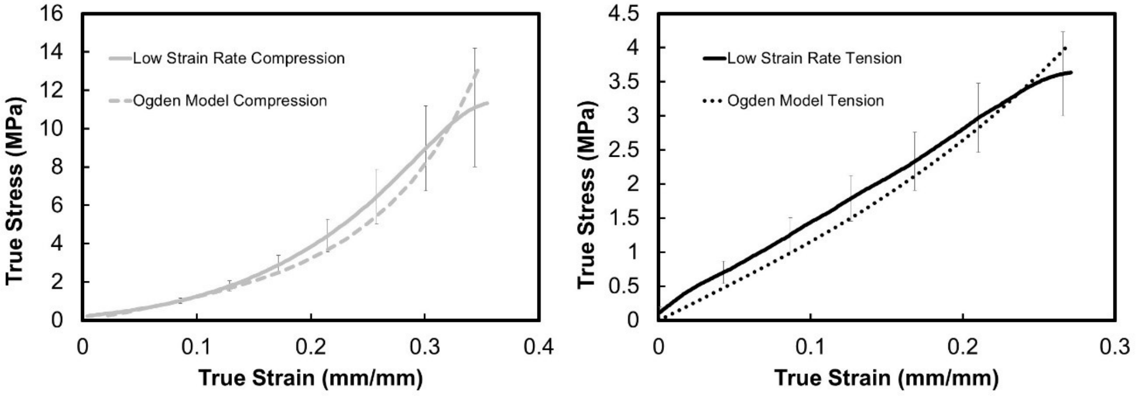

Figure 3.5 Single element simulation results for the midline cartilage using the Ogden model compared with experimental results. (Left) Low-strain rate compression comparison and (right) low-strain rate tension comparison.

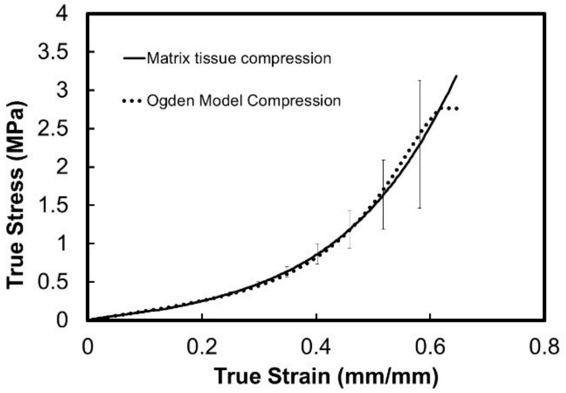

Figure 3.6 Single element simulation results for the matrix tissue using the Ogden model compared with experimental results.

3.2.3 Abaqus Model and Boundary Conditions

The model produced by ScanIP will incorporate the hyperelastic model from the previous section for the material model of both the midline cartilage and the matrix tissue. A simple elastic model using the elastic modulus from the nanoindentation data in Section 2.4 will be used for the network cartilage.

The mesh generated by the ScanIP software contains a total of 1.42 million elements composed of 1.30 million C3D4 linear tetrahedral elements and 0.12 million C3D8 linear hexahedral elements. A parametric study was performed on the model to examine the effect of the number of processors on the computation time. Based on the graph shown in Figure 3.7, 48 processors was found to be the optimal number for computational time. A time increment of $1\text{x}10^{-6}$ seconds was found to produce stable results. The total time period of each simulation presented was 1 s. Field and history output were requests at increments of 0.01 s, and the computational time for each simulation was roughly 12 hours.

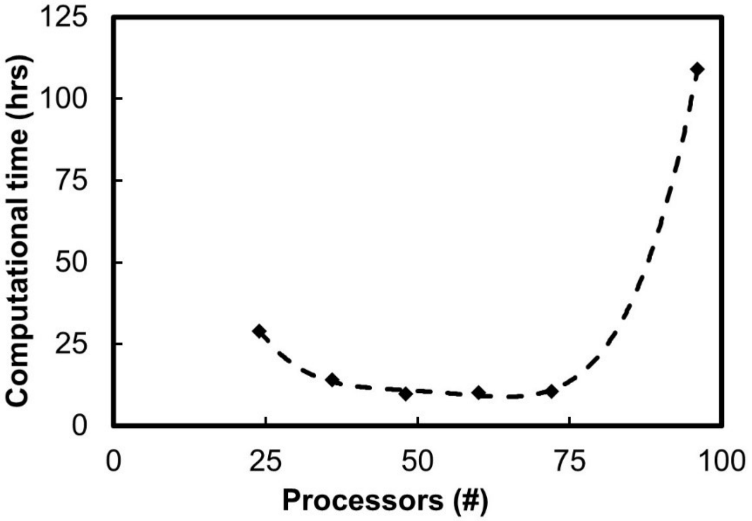

Figure 3.7 Computational time versus number of processors.

Various loads were applied on the rostrum to visualize and understand the stress distribution within the rostrum and possible stress dissipation mechanisms. For each simulation, the rostrum had a fixed boundary condition on the cranial end of the rostrum.

Simulations with pressure loads representing the force of water flow were performed in the x, y, and z axes (refer to Figure 3.9 for axis orientation). First, an FEA with a pressure load in the y-direction will be performed. A pressure in the y-direction represents the least aerodynamic orientation of the rostrum and the hydrodynamically worst orientation for a paddlefish while swimming. However, this is typically observed in the paddlefish as it eats it prey or escapes its predators. In this case, the fish is either swimming towards the surface the water or towards the bottom of the river floor, and the top or bottom surface of the rostrum is subjected to the forces from the water flow. Figure 3.8 illustrates the pressure load in the y-direction.

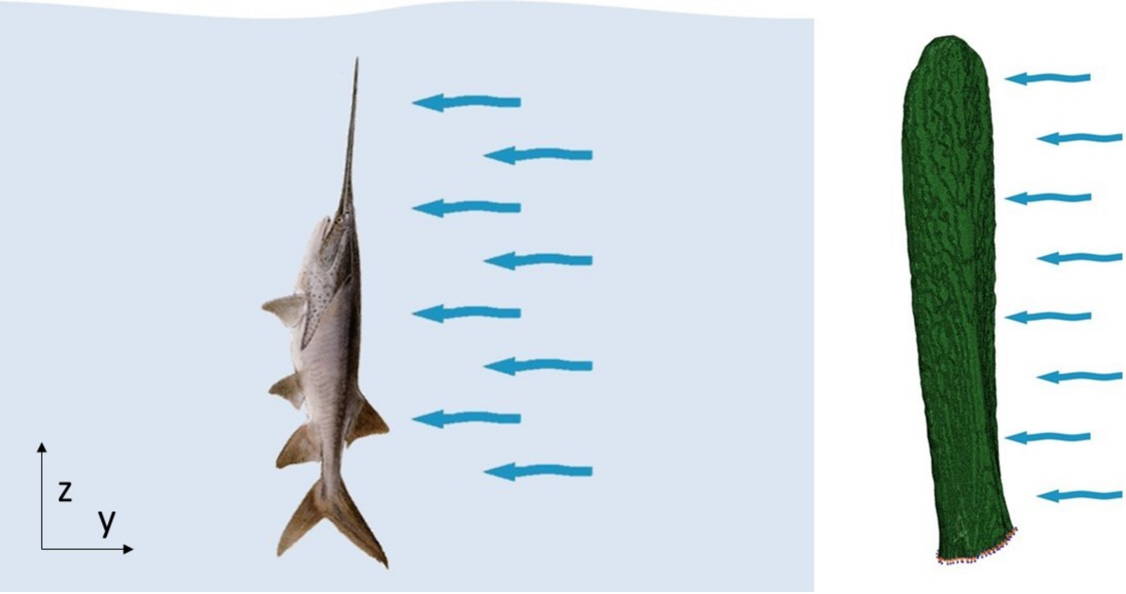

Figure 3.8 Diagram for a pressure load in the y-direction from the fluid flow of water.

Additional simulations will be done using a pressure load in the x-direction as well as the z-direction.

To determine the pressure caused by the water flow, Bernoulli's equation is applied (Eq. 3.6).

$$\frac{1}{2}\rho {v_1}^2 + \rho g z_1 + P_1 = \frac{1}{2}\rho {v_2}^2 + \rho g z_2 + P_2 \tag{3.6}$$

Based on the diagram in Figure 3.8, Equation 3.6 simplifies to:

$$P_{rostrum} = \frac{1}{2}\rho_{water} {v_{water}}^2 \tag{3.7}$$

Research done on the Mississippi River shows that the maximum water velocity in a channel typically reaches up to 1.2 m/s (53). Using this velocity and the density of water, the resulting pressure seen in Figure 3.8 is 720 Pa.

3.3 FEA Results

Figures 3.10-3.15 depicted below show how the rostrum responds to the various loading conditions. The network cartilage experienced the greatest stresses, and as a result the majority of the FEA figures will display the stress distribution for the different stress tensors within the network cartilage. Figure 3.9 labels the viewpoints of the rostrum, as well as the orientation of the coordinate system.

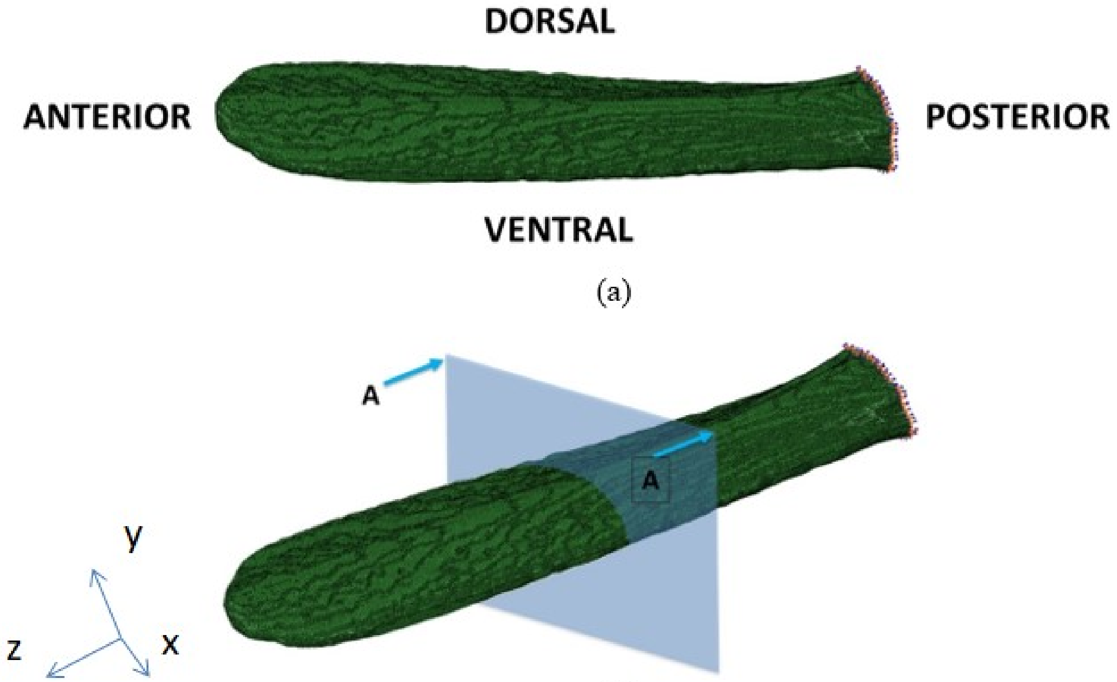

(a)

(b)

Figure 3.9 Stress tensor orientation

(a) Labeled sides of the paddlefish rostrum. (b) Section A-A which will be referred to as the ‘sectioned view’ of the rostrum.

Figures 3.10, 3.11, and 3.12 show the stress distribution throughout the network cartilage resulting from top-pressure loading (Fig. 3.10), side-pressure loading (Fig. 3.11), and front-pressure loading (Fig. 3.12). Appendix A provides a more comprehensive figure set, showing all the stress tensor components for each loading condition and highlighting different magnitudes of stresses.

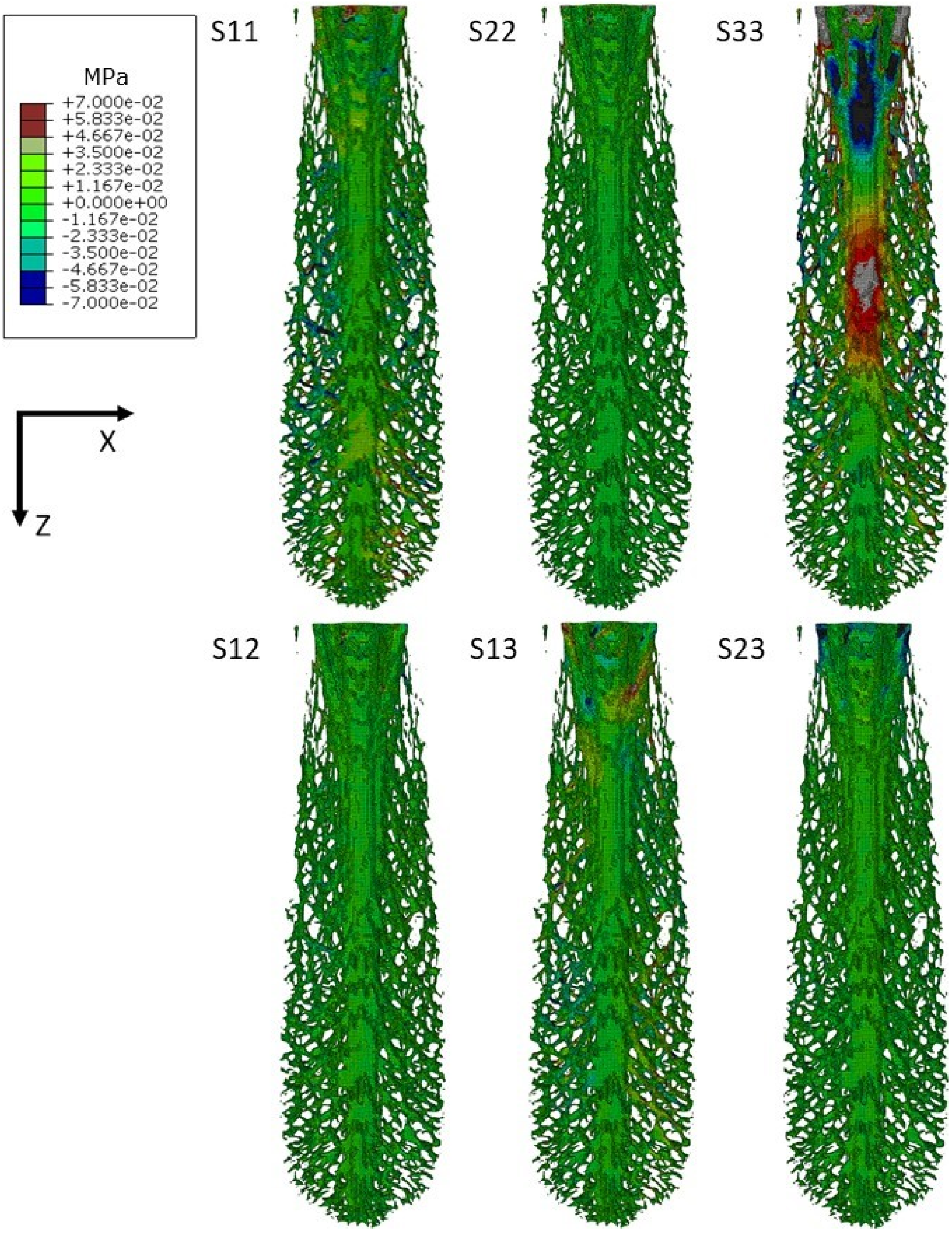

Figure 3.10 Dorsal view of the stress distribution for stress tensor components from top-loading pressure simulation. Maximum stress shown is 0.07 MPa.

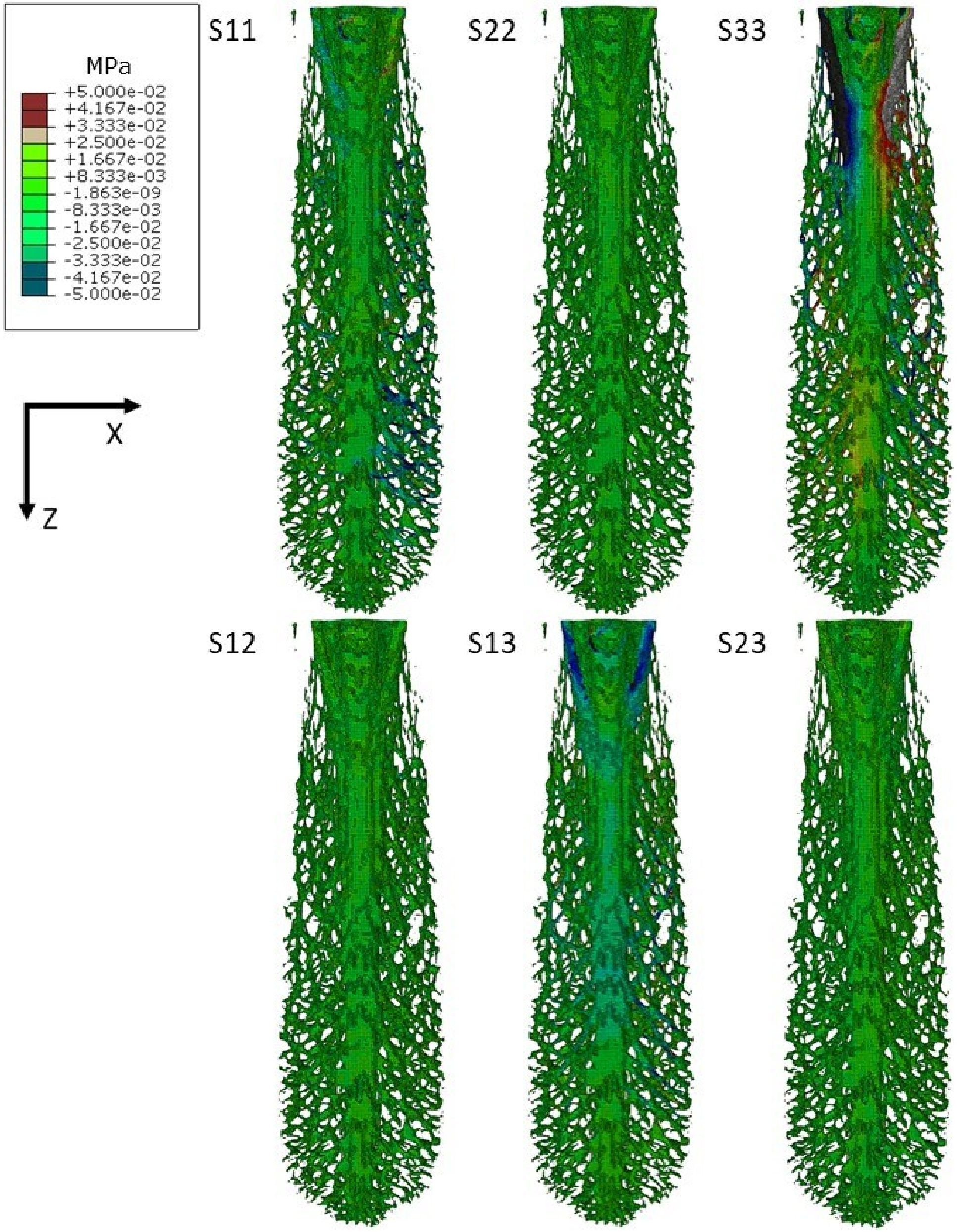

Figure 3.11 Dorsal view of the stress distribution for stress tensor components from side-loading pressure simulation. Maximum stress shown is 0.05 MPa.

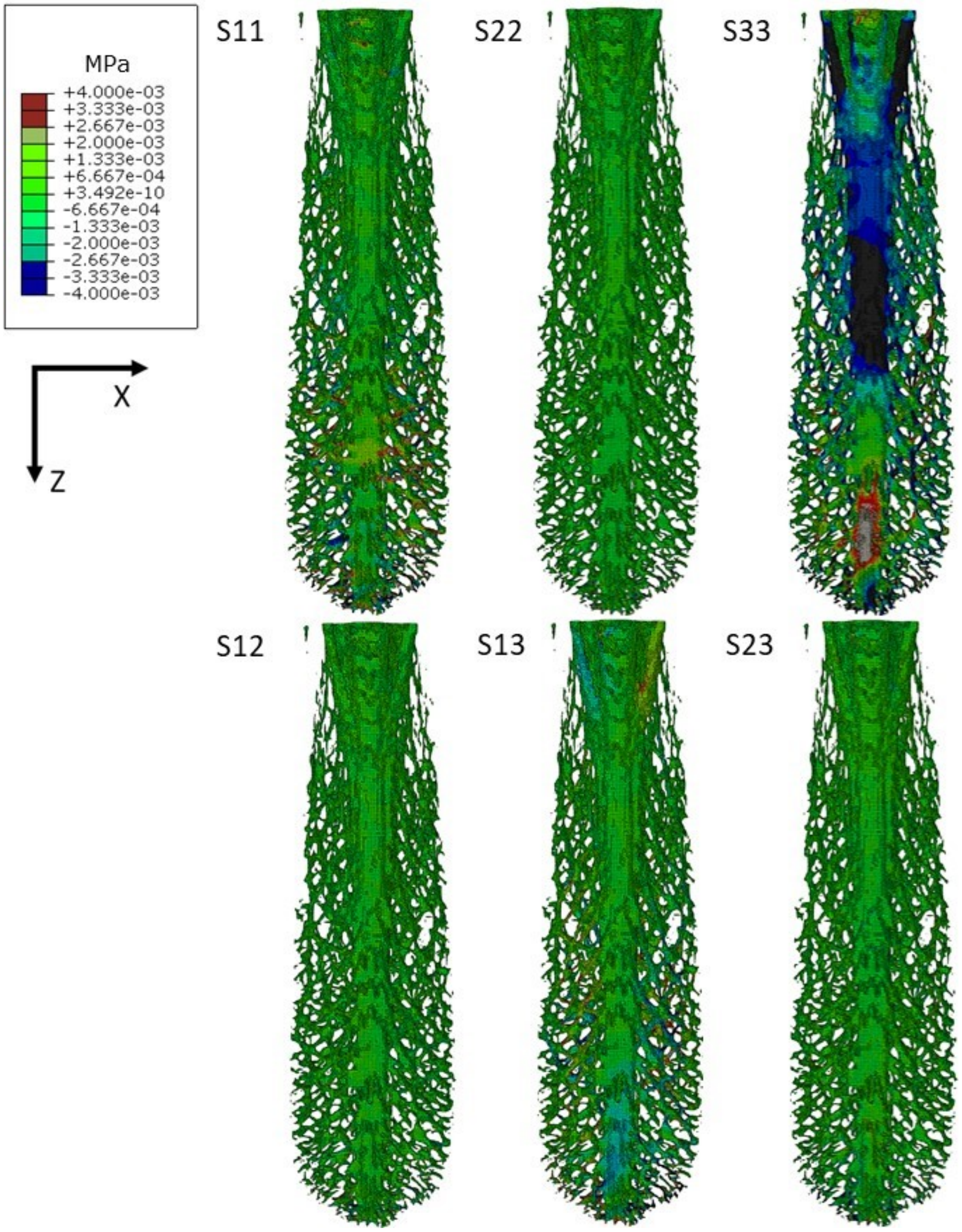

Figure 3.12 Dorsal view of the stress distribution for stress tensor components from front-loading pressure simulation. Maximum stress shown is 0.004 MPa.

3.4 Discussion

Because the rostrum is unique a unique structure in nature, the structural characteristics were quantified to gain insight into the integrity of the its design. Using

ScanIP, the total volume fraction of the matrix tissue, network cartilage, and midline cartilage were found to be 61.8%, 2.16%, and 16.5%. Additionally, cross-sectional slices were taken along the length of the rostrum to determine the overall area of the cross section as well as the area fraction of each material. Figure 3.13 measures the changes in total cross-sectional area of each slice, while Figure 3.14 quantifies the area fraction of the midline cartilage, network cartilage, and matrix tissue. From Figure 3.14 the area fraction of the rostrum is mostly comprised of the matrix tissue throughout the entire length. The area fraction of the network cartilage is greater than the midline cartilage at the free end. However, towards the cranial end the branching system of the network cartilage reduces and area fraction of the midline cartilage becomes greater.

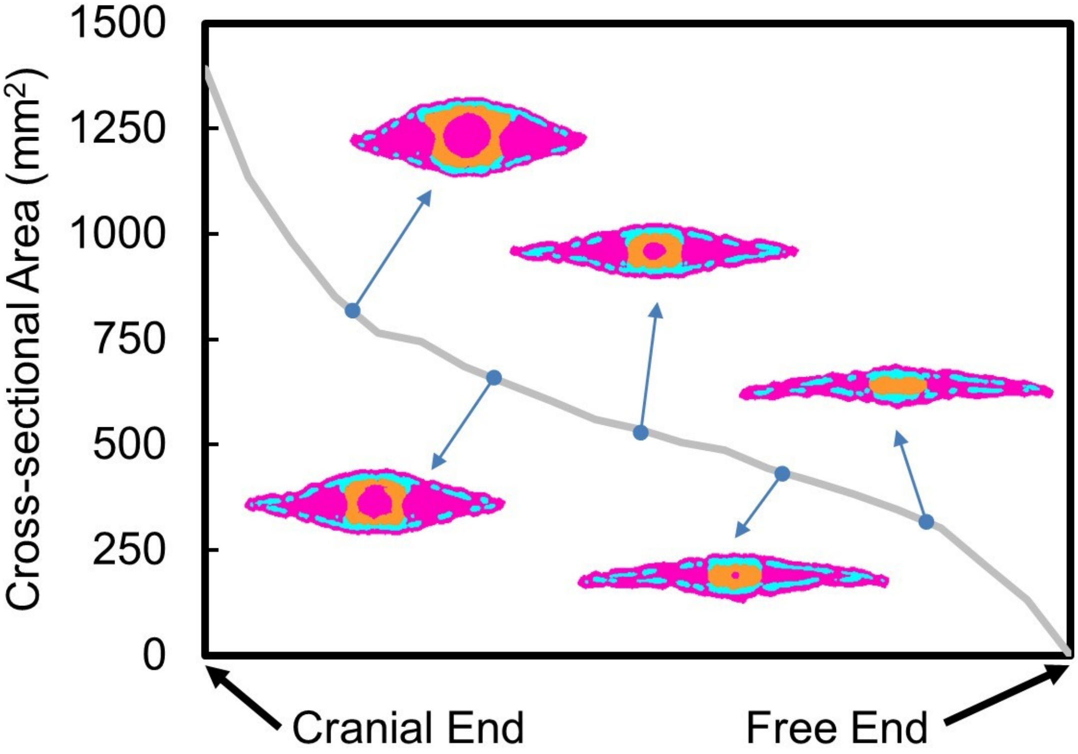

Figure 3.13 Changes in total cross-sectional area along the rostrum.

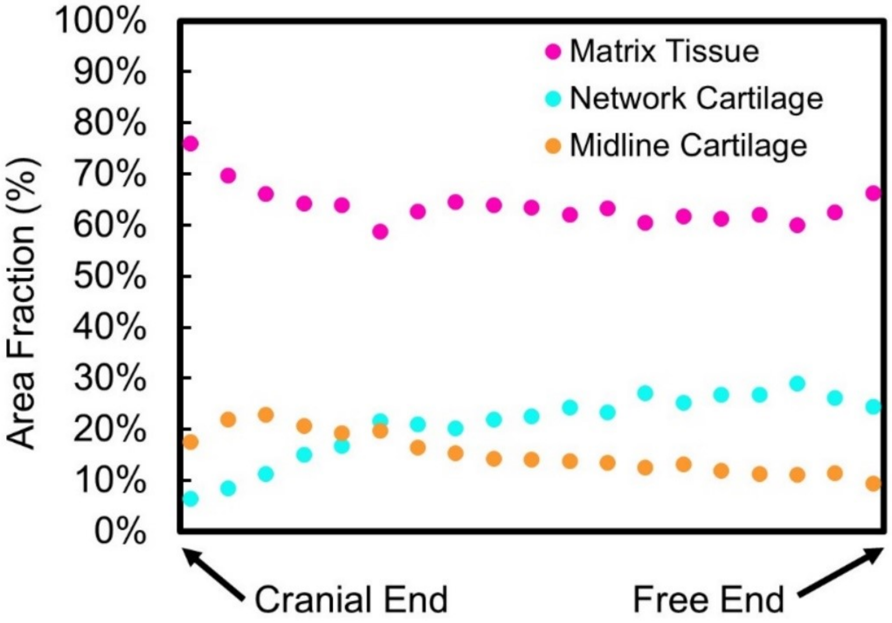

Figure 3.14 Area fraction of the matrix tissue, network cartilage, and midline cartilage along the length of the rostrum.

FEA results were also compared to an analytical solution. The effects of the cross-sectional geometry on the bending stress were calculated using:

$$\sigma_{bending} = \frac{My}{I} \tag{3.8}$$

where y and I represent the distance from the neutral axis and the moment of inertia, and were calculated from BoneJ image analysis. Assuming the stresses would mainly occur in the network cartilage, y and I were determined for the network cartilage and used to determine the maximum bending stress from Eq. 3.8. At the fixed end, the distance from the neutral axis and the moment of inertia were calculated as 7.13 mm and 7209 mm^4, respectively. The moment, M, was calculated, from the shear and moment diagrams seen below in Figure 3.15.

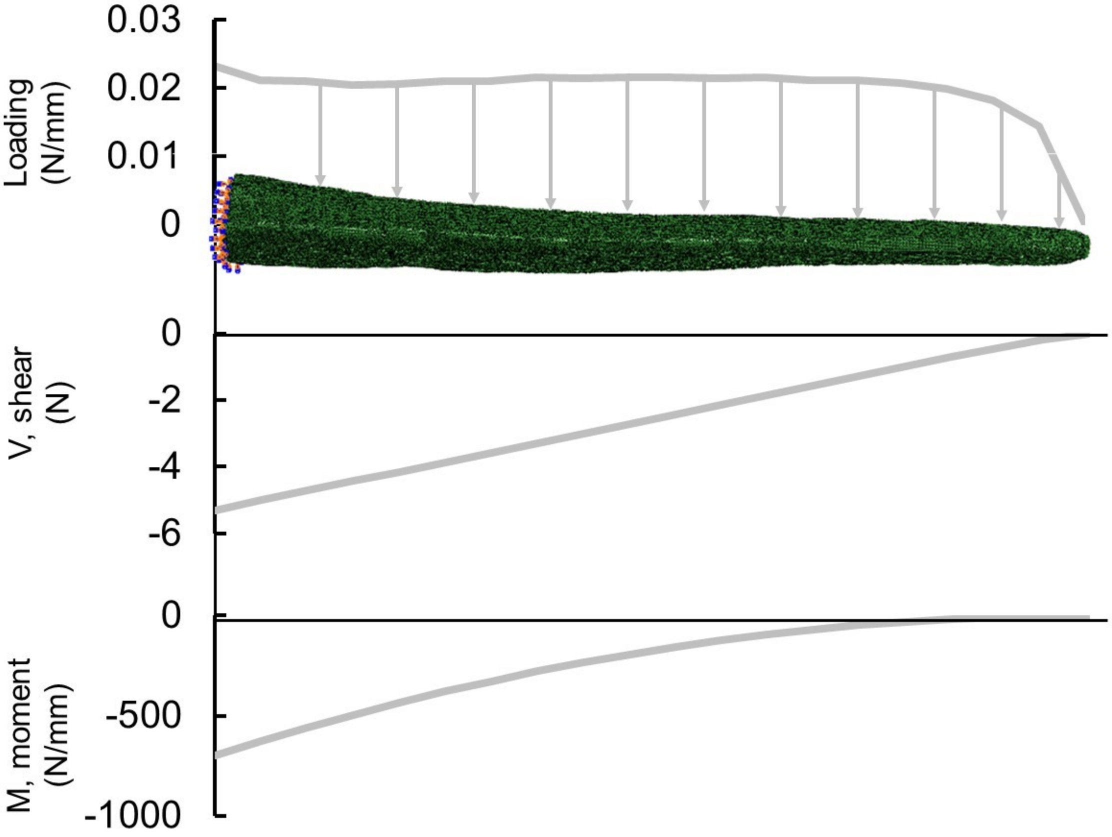

Figure 3.15 Shear and moment diagrams for top-pressure loading simulation.

The loading diagram is a function of the calculated pressure of 720 Pa, as well as the width of the rostrum at a given length. Using the moment calculations seen in Figure 3.15 in conjunction with the BoneJ findings, the resulting bending stress occurring within the network cartilage at the fixed end was calculated to be 0.69 MPa. The calculations compare very well with the simulation results seen below in Figure 3.16 which show the S33 stress tensor within the network cartilage.

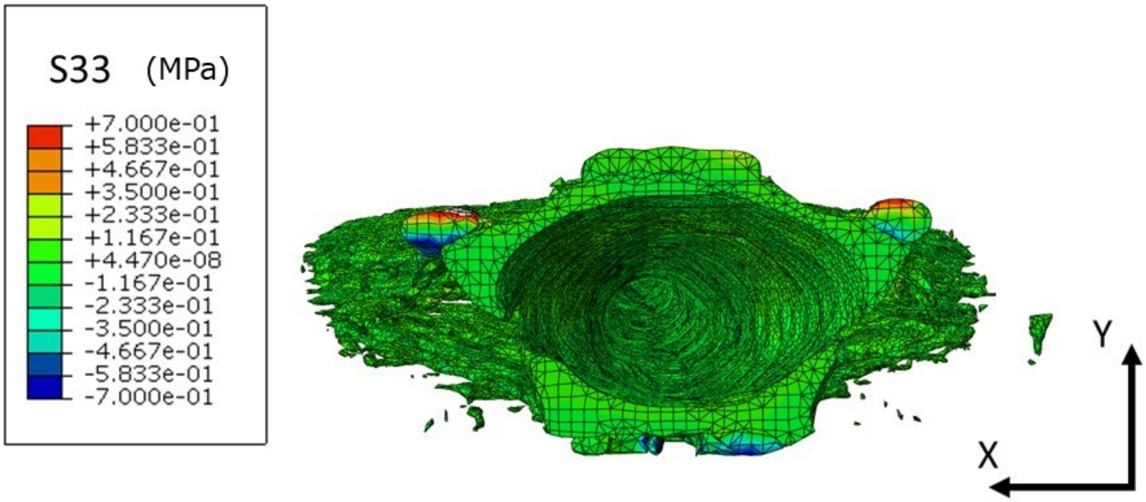

Figure 3.16 Stress diagram of the network cartilage at the fixed end of the rostrum.

In general, the stresses experienced are very low compared to the yield strength of bony materials, which range in magnitude from 10 MPa to 100 MPa (54)(55). The minimal stresses are a result of the boundary conditions which describe a typical water flow experienced by the fish. The resulting pressure is not expected to cause any detrimental damage caused by the stresses in the rostrum. Because of the boundary and loading conditions prescribed, the rostrum behaves somewhat similar to a cantilevered beam. As a result, the primary stress tensor component in each loading condition was the S33 tensor, resulting mainly from the bending moment experienced by the rostrum. The secondary stress tensor in each component was found to be S13 shear stress tensor. However, Figure 3.10 shows some compressive stresses in the S33 tensor. This is a result of the non-uniform direction of the pressure added on the rostrum. The pressure loading placed on the rostrum acts in the normal direction on the element. As a result of the changing cross sections (see Figure 3.13), compressive loads were introduced towards the cranial end of the rostrum. Nevertheless, the maximum compressive stresses experienced are still an order of magnitude less than the resulting bending stress seen at the fixed boundary condition.

Figure 3.13 compares all three loading conditions. The maximum Von Mises stresses experienced at the fixed end of the rostrum are 0.7 MPa, 0.3 MPa, and 0.02 MPa. Based on the results, the boundary condition with the top-loading pressure experienced the most stress, which was to be expected due to the shape of the rostrum. The top-loading pressure also represents the least hydrodynamic orientation, which is apparent in the manner of how the paddlefish swims, which is side to side (where the water flows in the x-direction). Nevertheless, the paddlefish will sometimes experience top-loading pressure as it maneuvers to feed on zoo plankton.

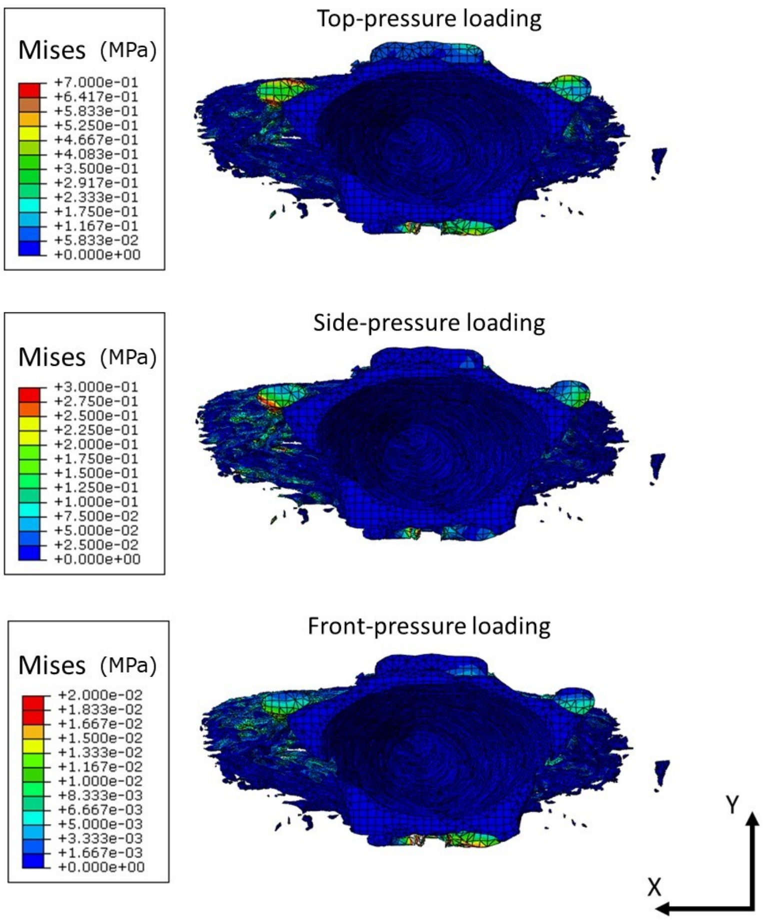

Figure 3.17 Comparison of max stresses between different loading conditions.

Although abaqus results were able to provide detailed feedback into the overall stress distribution of the structure, the load transfer mechanisms of the system are still unknown. However, observations into the stress distribution provide insight into the integrity of the network cartilage. The design of the rostrum contains characteristics of fail-safe design. The branching system provides multiple load paths for the structure. Failure within one of the branches would be transferred to other members. Also, from Figures 3.18, the outer branches of the network cartilage may seem to provide early detection of stresses. As the pressure load increases, the higher stresses are experienced first within the branches of the network cartilage before the main line.

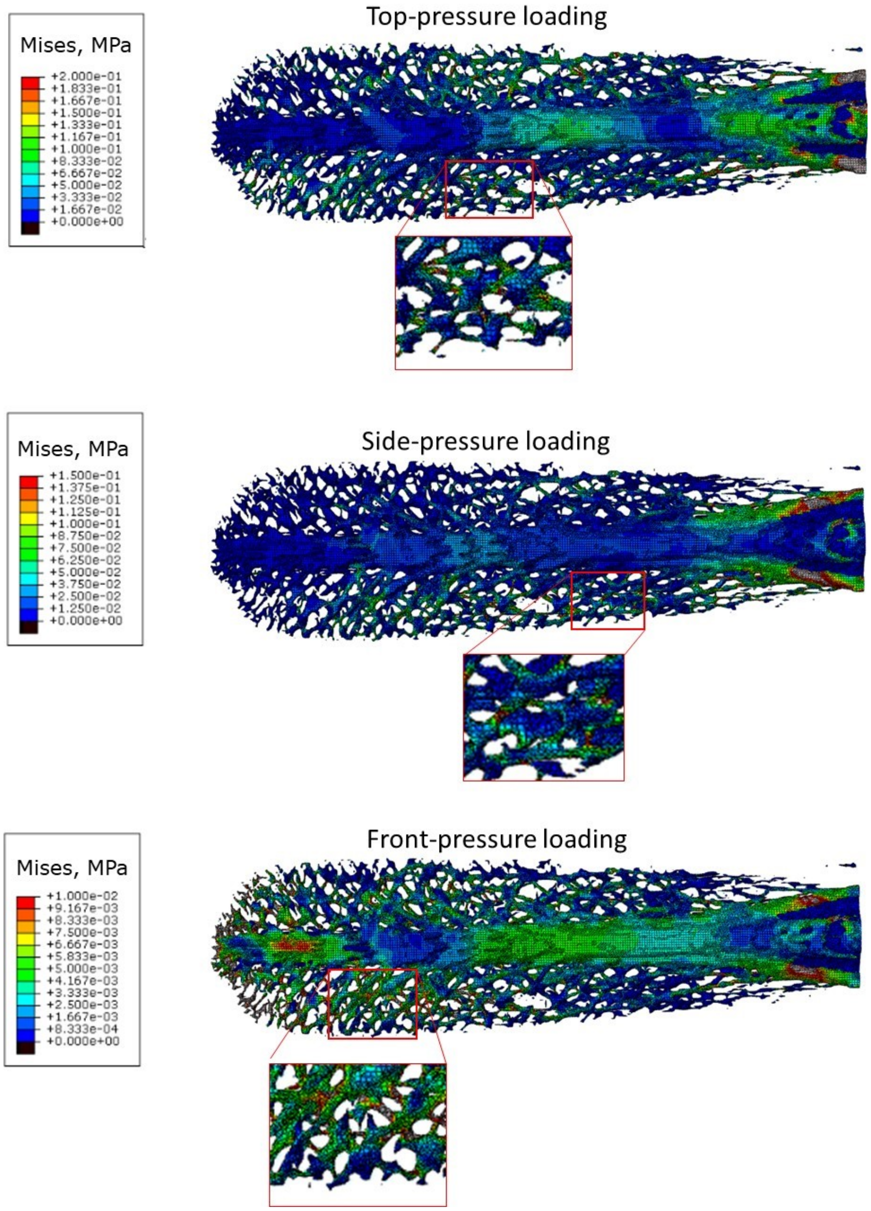

Figure 3.18 Branches of the network cartilage experience higher stresses than the main network cartilage line.

Additionally, the results and models used within this paper has been used in other research applications of the rostrum. Allen and Riveros (18) hydrodynamically characterized the paddlefish rostrum using models and data seen in this paper. They found that the size, shape, and position of the rostrum develop hydrodynamic life which aids in the fishes feeding. Furthermore, they found that the streamlined shape of the rostrum resulted in minimum pressures experienced, similar to the results seen in this paper. In fact, they found that the amount of lift is comparable to that produced by a symmetric airfoil (NACA 0012). Some additional applications can include protective panels, novel building materials, body and vehicle armor, and ship design.

CHAPTER IV

BIO-INSPIRATION AND DESIGN

4.1 Introduction

4.1.1 Paddlefish Rostrum and Cell Tower

One of the main functions of the rostrum is to act as an antenna. The rostrum extends from the cranial end, which lengthens the Ampullae of Lorenzini (electroreceptors), thus enhancing the paddlefish's electroreception range for feeding. This is analogous to how cellular towers work; the larger the tower, the greater the signal coverage. Additionally, they both undergo similar loadings, where the rostrum experiences pressures resulting from fluid flow, and the cell tower undergoes air flow pressure from wind and stresses resulting from the additional weight of the structure. Because of the similarities, the rostrum may be a suitable candidate for alternate cell tower designs or provide inspiration into the improvement of current tower designs.

Communication towers are typically classified into three different type of towers: guyed towers, monopole, and self-supporting towers. Guyed towers are held up by tensioned cables, and though they are typically cheaper to build, they require an extended surrounding area to anchor the wires. Monopoles are single self-supporting poles, typically built on top of high raised buildings. Self-supporting towers are towers are typically built of a lattice steel structure (56)(57), and though they weigh more than guyed towers, they do not require an extensive base to build on. For this research, a new design for a self-supporting tower will be created.

Weather plays an important role when analyzing cell towers and investigating a design's structural response and viability. Wind forces account for many tower failures and include effects from regional wind speeds (58). Ice and snow are also detrimental to a structure's integrity (59). Not only does the additional weight increase the stress on the structure, but the ice and snow will also demand that the design enlarge the structure's area that can then be subjected to strong winds. As a result, designers should take into consideration the dangerous combination of high wind speeds and icy/snow conditions (60).

4.1.2 Compromise Decision Support Problem and Bio-inspiration

One challenge facing designers is the concept of idea generation. Bio-inspiration can alleviate this by providing unique structural designs and functions shown in nature (recall Figures 1.1, 1.2, and 1.3). For the paddlefish, the network cartilage provides a unique design for its function as both an antenna and hydrodynamic structure. Although bio-inspiration can lead to new conceptual ideas, the degree to which a designer should apply these concepts and structures into a design can be challenging.

Bio-inspiration and biomimicry are terms that are often interchanged but have slightly different aspirations. Biomimicry focuses on the imitation of biological systems, whereas bio-inspiration uses principles in nature and aims to create novel designs that have yet to be created. Because of this main difference, bio-inspiration relies more on the knowledge of the designer. How exactly does one take into account the various parameters observed in biological structures and apply them to a new design? What are the important features that can improve new designs? In an attempt to answer these types of questions, a new paradigm built on the construct compromised Decision Support Problem (cDSP) (61) will be used.

In the design process, one common obstacle is the tradeoff between competing design objectives. In the simple case of a pressure vessel, the designer may want to minimize the weight of the pressure vessel but maximize the pressure vessel's volume. Improving one of these objectives adversely affects the other; they are competing objectives that need to be compromised. To aid in these type of decisions, the compromise Decision Support Problem (cDSP) (61) is used.

The cDSP is a mathematical construct that aims to satisfy a set of constraints and competing design objectives as closely as possible (62). A cDSP can improve the design of a system by exploring a solution space that is restricted by designer-specified constraints, showing again the importance of the knowledge of the designing engineer. cDSPs can have a wide range of applications and have been used for the design of aircraft, ships, optimization of the parameters used for steel production processes, and turbine propulsion systems (63)(64)(65).

A quick guideline to the components and terminology used for the cDSP is summarized in Table 4.1. A more detailed explanation is provided in the following sections.

Table 4.1 Components of the compromised Decision Support Problem (cDSP).

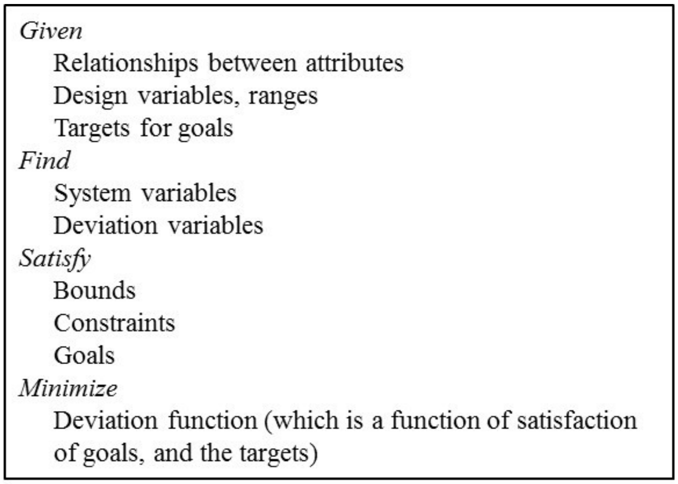

Given
- Relationships between attributes
- Design variables, ranges
- Targets for goals

Find
- System variables
- Deviation variables

Satisfy
- Bounds
- Constraints
- Goals

Minimize
- Deviation function (which is a function of satisfaction of goals, and the targets)

4.2 Methods

4.2.1 Cell Tower Model

A cDSP construct will be created for the design of a cell tower. The results for the cDSP will be compared with a tower described in a previous study by Martin *et al*. (57). Figure 4.1 shows the design variables used within the base tower. The tower is simplified from the original design, where the original design contains varying types of L-beams throughout the height of the structure, while the simplified tower uses 125 x 15 L-beams for the main beams and a 65 x 7 L-beams for the supports (see Figure 4.2 for L-beam annotation). The cell tower will has a square base, and truss members will be made of high strength steel with properties taken from a transmission tower design by Shea and Smith (56). The density, Young's modulus, and yield stress of the material are 7850 kg/m^3, 214 GPa, and 360 MPa, respectively. Additionally, Figure 4.3 shows the details of the L-beams within the Abaqus finite element model.

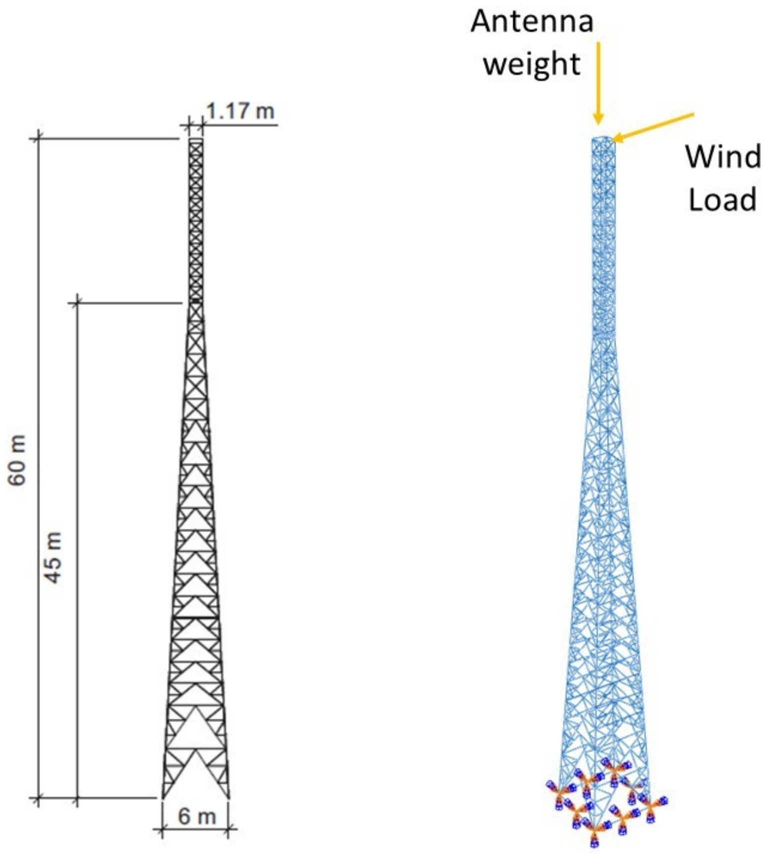

Figure 4.1 Cell tower base design (57)(left) and Abaqus model with loads and boundary conditions (right).

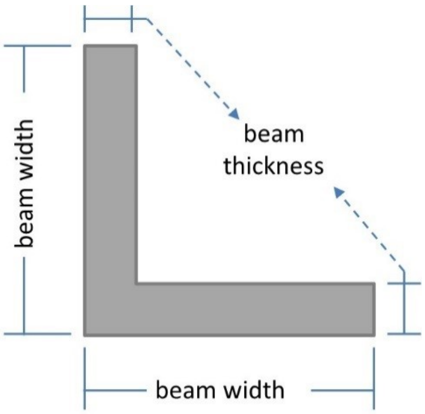

Figure 4.2 L-beam annotation, where 125 x 15 L describes an L-beam with a 125 mm beam width and 15 mm beam thickness.

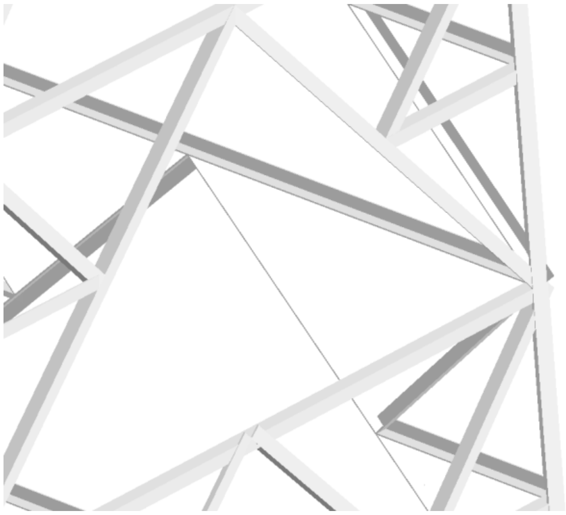

Figure 4.3 L-beams structures within the cell tower design.

The tower has a fixed boundary condition at the base of the structure. The antenna weight is 5.3 kN prescribed by the ANSI/TIA-222-G Standard (66). Because ice and wind are detrimental to a tower's design, the tower will include an additional weight from a 1.25 cm thickness layer of ice and a wind load of 1000 N on top of the structure. The final structure has 5412 quadratic beam elements with a total mass of 15,622 kg.

4.2.2 compromised Decision Support Problem of a Cell Tower

A possible work flow diagram of the design process is shown in Figure 4.3. The inclusion of bio-inspiration within the design process can affect the *Ideate* step, which is traditionally how bio-inspiration is used within a design; A novel biological structure provides ideas, and then possible concepts are generated, which may lead to a new design. These ideas and concepts come from the important features observed within the biological structure, but the actual application of the biological principles into the new design can be convoluted. However, within this design paradigm, bio-inspiration is also included within the *bio-inspired constraints* section in the cDSP (see Table 4.2). The designer is now able to constrain the design by including important features that were observed in the *Ideate* step. These *bio-inspired constraints* can represent certain features (aspect ratio, number of joints, *etc*.) the designer wants to mimic based on the biological structure of inspiration. Furthermore, because the cDSP allows the designer to explore a solution space, the bio-inspired design can be compared with the traditional designs, showing the effects of the bio-inspired constraints and validating whether the new, bio-inspired design is an improvement.

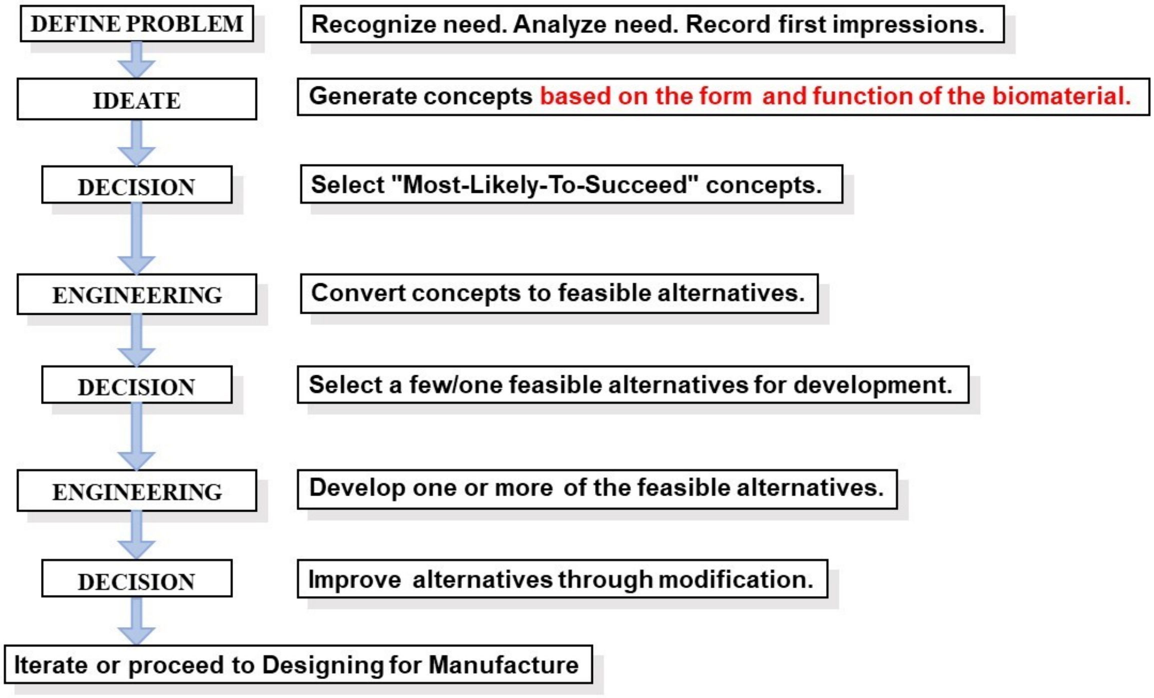

Figure 4.4 Design work flow with the inclusion of biomaterials.

Table 4.2 Components of the compromised Decision Support Problem (cDSP) with the inclusion of *Bio-inspired constraints*.

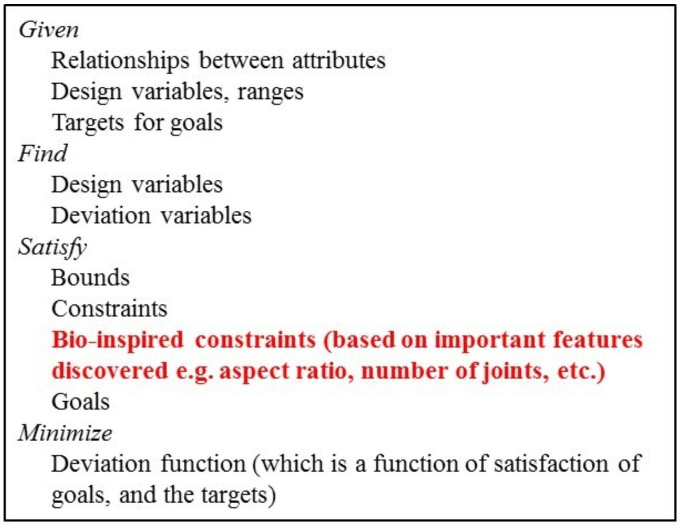

Given
- Relationships between attributes
- Design variables, ranges
- Targets for goals

Find
- Design variables
- Deviation variables

Satisfy
- Bounds
- Constraints
- **Bio-inspired constraints (based on important features discovered e.g. aspect ratio, number of joints, etc.)**
- Goals

Minimize
- Deviation function (which is a function of satisfaction of goals, and the targets)

This section will use a simplified cDSP to describe the process of using *bio-inspired constraints* within the cDSP paradigm for designing a cell tower. Refer to Table 4.2 for a list of the cDSP components described. An important stage in creating a cDSP is defining the problem, which will lay the foundation for the *given*, *find*, *satisfy*, and *minimize* sections. For this simplified, theoretical problem, a cell tower will be constructed with a minimum height of 40 m and will have a square base. Trusses will be made of a high strength steel L-beams, similar to the study performed on transmission tower lines by (57) and have two different cross-sectional areas for the main beams and support beams. The goals of this design are to minimize the cross-sectional area of the main L-beams, minimize cost, and maximize height.

Table 4.3 Cell tower cDSP components.

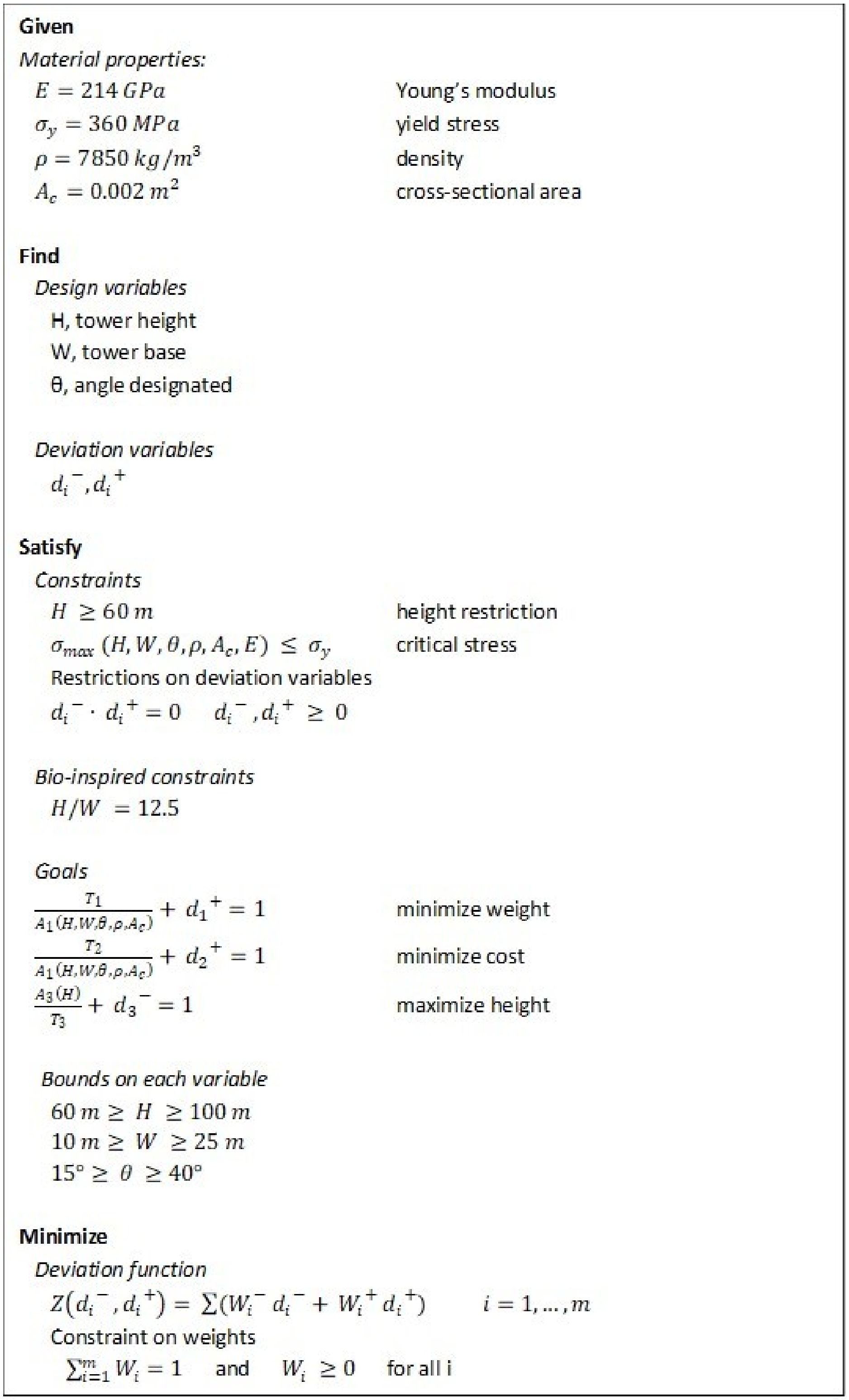

Given

Material properties:

$E = 214\,GPa$	Young's modulus
$\sigma_y = 360\,MPa$	yield stress
$\rho = 7850\,kg/m^3$	density
$A_c = 0.002\,m^2$	cross-sectional area

Find

Design variables

H, tower height
W, tower base
θ, angle designated

Deviation variables

d_i^-, d_i^+

Satisfy

Constraints

$H \geq 60\,m$	height restriction
$\sigma_{max}(H, W, \theta, \rho, A_c, E) \leq \sigma_y$	critical stress

Restrictions on deviation variables

$d_i^- \cdot d_i^+ = 0 \quad d_i^-, d_i^+ \geq 0$

Bio-inspired constraints

$H/W = 12.5$

Goals

$\frac{T_1}{A_1(H,W,\theta,\rho,A_c)} + d_1^+ = 1$	minimize weight
$\frac{T_2}{A_1(H,W,\theta,\rho,A_c)} + d_2^+ = 1$	minimize cost
$\frac{A_3(H)}{T_3} + d_3^- = 1$	maximize height

Bounds on each variable

$60\,m \geq H \geq 100\,m$
$10\,m \geq W \geq 25\,m$
$15° \geq \theta \geq 40°$

Minimize

Deviation function

$Z(d_i^-, d_i^+) = \sum(W_i^- d_i^- + W_i^+ d_i^+) \qquad i = 1, \ldots, m$

Constraint on weights

$\sum_{i=1}^{m} W_i = 1$ and $W_i \geq 0$ for all i

The *Givens* describe what is known in the system, which can be certain requirements that a design needs to be met or types of materials used within the system. In this example, a cell tower needs to be constructed with a minimum height of 40 m. The cell tower will have a square base, and truss members will be made of high strength steel, whose properties are analogous to the base tower model. Additionally, the tower will have a layer of ice with a thickness of 1.25 cm and density of 916.7 kg/m^3, and a wind load will be applied as a concentrated force of 1000 N on the top of the structure. A cost function is created as a function of mass. Cost values were derived from cost estimates for self-supporting towers from Trylon TSF Inc. (67) and is shown in Figure 4.5. A trendline is applied and is shown in the figure and is used as the function to correlate cost with the tower mass.

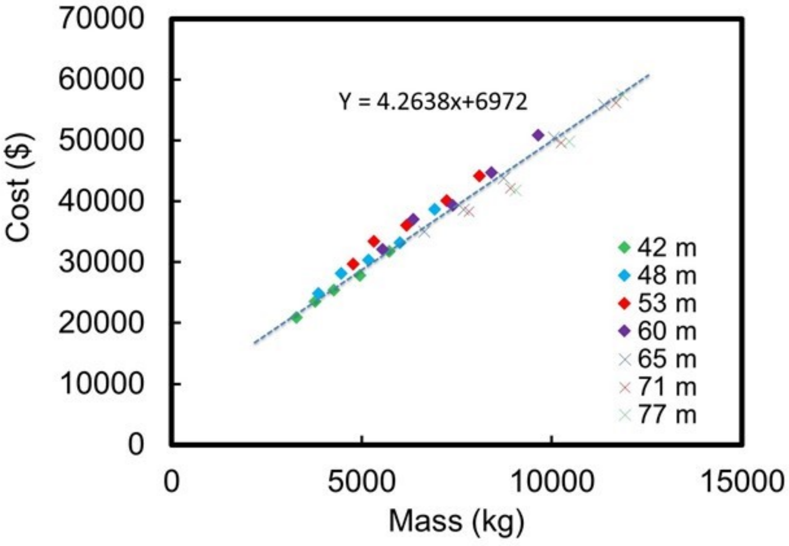

Figure 4.5 Cost versus mass for cell towers of different heights (data taken from Trylon TSF Inc. (67)).

The *design variables* represent variables that can be controlled independently by the designer. They are independent of each other and can accurately describe a system when correctly defined. For a cell tower, some *design variables* can be height, width, and the cross-sectional area of the trusses. For this design, the cross-sectional area is a function of the L-beam width and thickness, indicating that the L-beam width and thickness are the design variables. Again, the example provided represents a simplified design problem; some additional *design variables* for a more realistic problem can include the tower envelop angle (see Figure 4.3), the angle(s) between trusses, and the changes in L-beam designs throughout the length of the rostrum.

Bounds describe the upper and lower limits on the design variables. For instance, a cell tower may require a certain base width depending on the location of construction, or the height must be between two given measurements for maximum signal transmission and reception.

Constraints are limitations placed on a design. They may include strength constraints, stiffness constraints, or dimensional constraints. For example, a cell tower must withstand a load with a specific factor of safety, the maximum stress in a truss must be less than the critical buckling stress, the maximum mass must be less than a specified value. *Constraints* are incorporated for a design to be considered feasible, and mathematically, all constraints are functions of *design variables*. For this problem, the bending stresses and compressive stresses are constrained by the steel's yield stress. Additionally, a dimensional constraint is placed on the L-beam, where the thickness to width ratio is 1:10, which is a common ratio for the construction of steel L-beams. If the dimensions were not constrained, the cDSP may provide results that describe an L-beam that is not typically produced.

The *bio-inspired constraints* refer to ideas or designs observed in nature that will be directly applied to a design. The addition of this component allows designers to directly add aspects of biological structures to alter a design. Some examples of *bio-inspired constraints* are the aspect ratio of height to width, the number of joints, and the materials used. For this example, the height to width ratio of 12:1 is inspired by the length to width ratio of the rostrum shown in Figure 4.4. Additional *bio-inspired constratins* that can possible be added to a more in-depth model are provided below in the discussion.

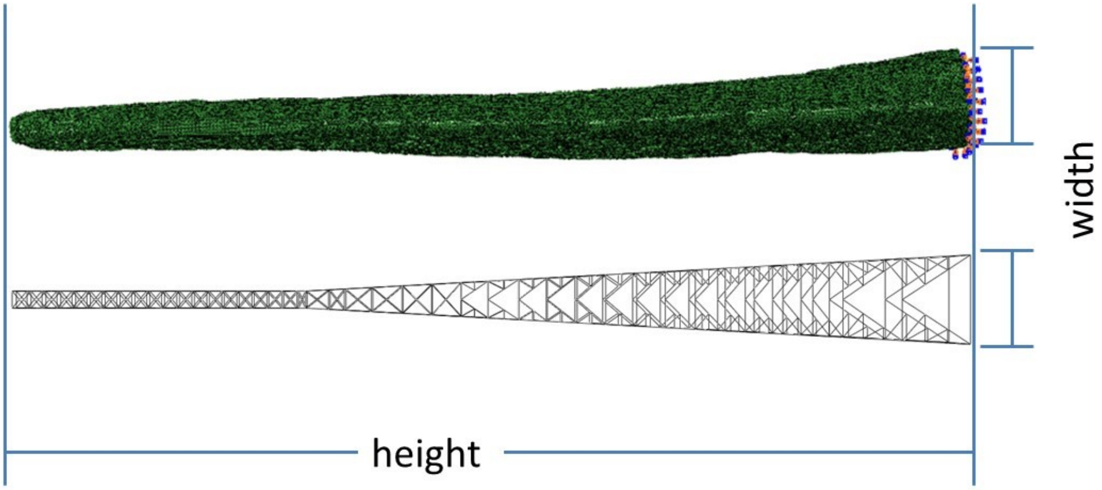

Figure 4.6 Height-width ratio of the paddlefish rostrum used as a *bio-inspired constraint.*

In the cDSP the design objective is modeled as a *goal*. These *goals* represent what the designer wants to achieve from the design. In this example, the *goals* are to minimize the cross-sectional area of the main truss members, minimize cost, and maximize height. For each *goal,* there is an assigned target value, T_i. The actual attainment of the *goal* exists in the form of the achievement function, $A_i(x)$. The achievement function, $A_i(x)$, represents the ith objective as a function of design variables, x. The difference between the target value and the actual attainment is quantified by the *deviation variable*, d_i:

$$d_i = T_i - A_i(x) \tag{4.1}$$

The *deviation variable* can have a positive or negative connotation, ${d_i}^-$ and ${d_i}^+$, and they represent the degree to which a target value is overachieved or underachieved. The attained value cannot be both overachieved and underachieved, therefore one of them must be zero. The following restrictions apply to the *deviation variables*:

$${d_i}^- \cdot {d_i}^+ = 0 \tag{4.2}$$

$${d_i}^-, {d_i}^+ \geq 0 \tag{4.3}$$

The aim of the cDSP is to minimize the difference between target values and attained values. This is accomplished by minimizing the deviation function, $Z({d_i}^-, {d_i}^+)$, which is written in terms of the *deviation variables*. The combination of target values conceived by the designer may not be possible to achieve, but the *deviation function* provides an indication of the degree to which specific goals are achieved. The formulation of the *deviation function* can be *Archimedean* or *Preemptive*, and for this example we will use and discuss the *Archimedean* formulation. This formulation is a weighted sum of the deviations of each goal. Here, we quantify the importance of this goal with respect to the other goals, and the most general form is written as the following,

$$Z({d_i}^-, {d_i}^+) = \sum({W_i}^- {d_i}^- + {W_i}^+ {d_i}^+) \qquad i = 1, \ldots, m \tag{4.4}$$

where the weights, $W_1, W_2, \dots, W_m$, indicate the level of importance of each goal. For the Archimedean formulation, the weights satisfy the following conditions:

$$\sum_{i=1}^{m} W_i = 1 \quad \text{and} \quad W_i \geq 0 \quad \text{for all i} \qquad (4.5)$$

Once a cDSP is properly define, they are solved through a tailored computational environment known as DSIDES (Decision Support in the Design of Engineering Systems). Appendix B contain the supplementary cDSP files for the tower design.

4.3 Results

The results of the cDSP based on the construct and variables observed in Table 4.4 prescribe a tower with a height of 72 m beam width of 80 mm and a beam thickness of 8 mm. The goals of minimizing the cross-sectional area, maximizing height, and minimizing cost have values of 12.16 cm^2, 70 m, and \$59,500. The deviation variables for these goals are 0.23, 0.12, and 0.35 respectively. The width of the tower was constrained by the *bio-inspired constraint* height to width ratio of 12:1. The cDSP tower will have a tower base width of 6 m.

Table 4.4 Design variable and goal comparison of the cDSP tower with the base tower.

	Base tower	**cDSP tower**
DESIGN VARIABLES		
height, m	60	72
beam width, m	0.12	0.08
beam thickness, m	0.015	0.008
GOALS		
minimize cross-sectional area of main beams, cm^2	33.75	12.16
maximize height, m	60	70
minimize cost, $	73500	59500

A revised tower was modeled in Abaqus with the cDSP results. Wind and ice loads were applied, and the resulting stresses from the applied loads on the new model is compared with the base model and is shown below in Figure 4.7. From Figure 4.7, the max stress experienced in the base tower and cDSP tower are 24.83 MPa and 54.45 MPa, respectively. The maximum deflection experienced in the towers are 1.74 cm and 6.87 cm for the base tower and cDSP tower, respectively.

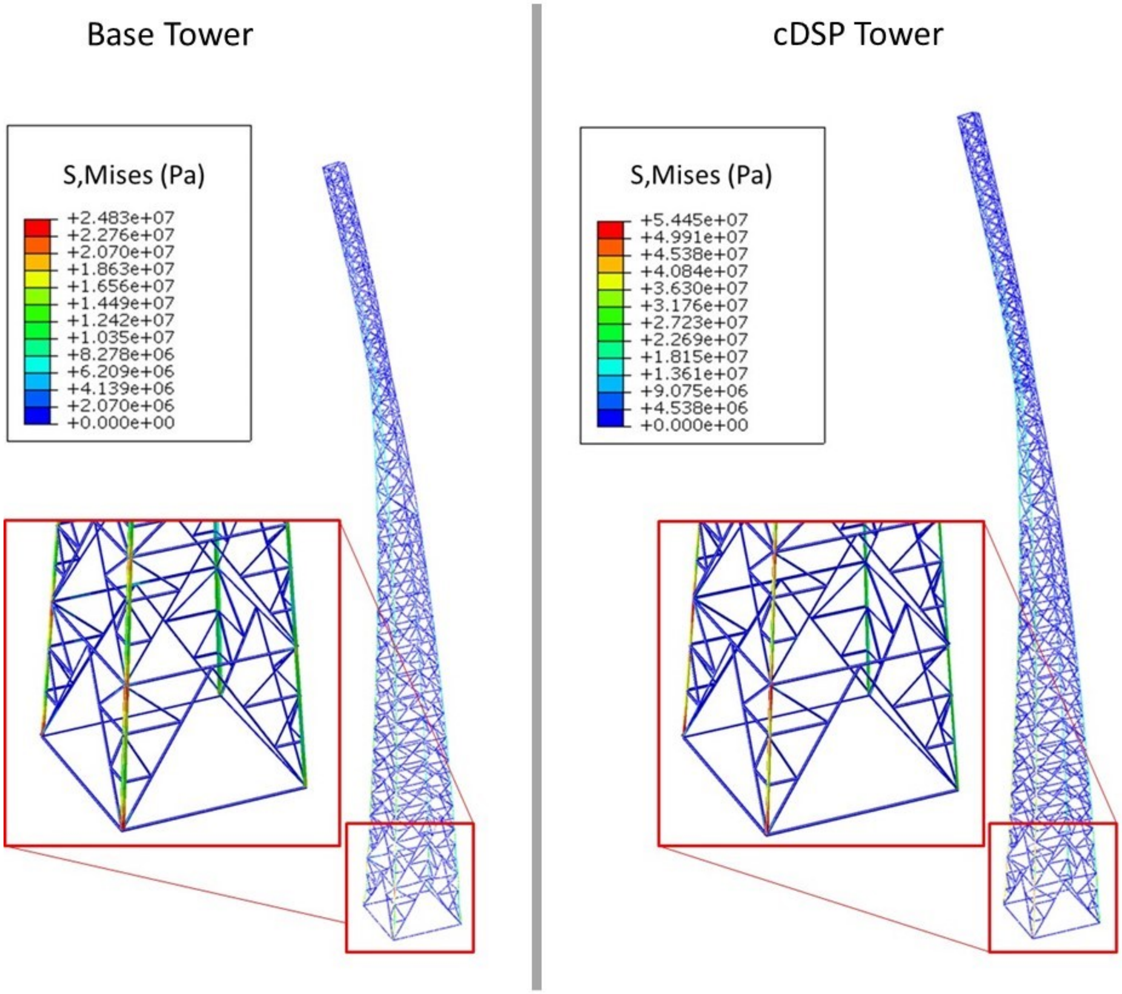

Figure 4.7 Comparison of the maximum stresses experienced by the base model and cDSP model.

4.4 Discussion

As of September 2017, the state of Mississippi has over 3700 towers (Federal Aviataion Administration Digital Obstacle File). The improvement of the designs of towers can lead to cost reduction and material reduction while still meeting the standards of tower design. The proposed cDSP construct can help aid in the design process of towers under a variety of environments and loading conditions.

The original tower design had a total mass of 15622 kg and the total length of all the beams was 1609 m. The total length of the main beams of the structure was 240 m, accounting for 15% of the overall length. However, the total mass of the main beams was 6358 kg, which accounts for 41% of the total mass. For this reason, one of the goals for the cDSP was to minimize the cross-sectional area of the main beams, which will reduce the overall mass of the entire structure. Table 4.4 compares the design variables for the base tower and cDSP tower. Comparing the results shown in Table 4.4 the cDSP tower has 58% less mass in the main beams (21% mass reduction overall), 20% increase in height, and a 20 % decrease in cost. Recall that the cost function prescribed for the towers was based only as a function of mass. Taking into consideration the construction costs would likely also cause the cost of the tower to be a function of the height as well. The cDSP tower does experience a higher stress because of the added weight and the increased wind load. However, the max stress experienced of 54.4 MPa is lower than the yield strength of 360 MPa.

The cDSP construct also has the ability of including a material selection design variable within another construct called the selection-DSP (68). Suppose a tower construction company has access to a variety of different steel alloys with different material properties. The combination of cDSP and selection-DSP will take into account the material properties and costs of the different steels when attempting to achieve the designer-specified goals.

Throughout the process of the cDSP, the designer's knowledge and decision-making is highlighted. The designers with an expertise in cell towers know how to properly define the design problem and the important *design variables* to consider. The loads prescribed above are for wind and ice assumptions, but an expert tower designer will know a specific ice thickness layer and wind loads depending on the region where the tower is constructed. The knowledge of the designer can create realistic goals and target values. If the targets of the goals cannot be met, the knowledge of the designer becomes even more valuable, because they would have to decide which goals are more important to the design. The decision-making accomplished by the designer can also greatly affect the solution based on how they weight specific goals. Additionally, the results may also be different between two different designers based on how they weight and target each goal. A more experienced designer may come up with a better design compared to the novice.

Furthermore, the familiarity of the designer with the biological structure used for inspiration will help guide them in the important aspects to include within the *bio-inspired constraints.* For this specific problem, only the height-to-width ratio of the paddlefish rostrum was added as a design constraint. Some additional constraints can include the material selection for the main beams and the support beams. The network cartilage showed spatial dependence on the material properties (recall Figures 2.14 and 2.15). Applying this constraint will change the desired response of the support beams. The result of this constraint can possibly reduce the required yield stress for the support beams, change the material of the support beams, and possibly reduce the overall cost of the tower. Another possible bio-inspired constraint includes taking changing widths seen within the main line of the network cartilage and applying it to the changing main L-beam dimensions within the cell tower (Figure 4.8). Furthermore, the same width ratio constraint can be applied to the branching system of the network cartilage with the support beams.

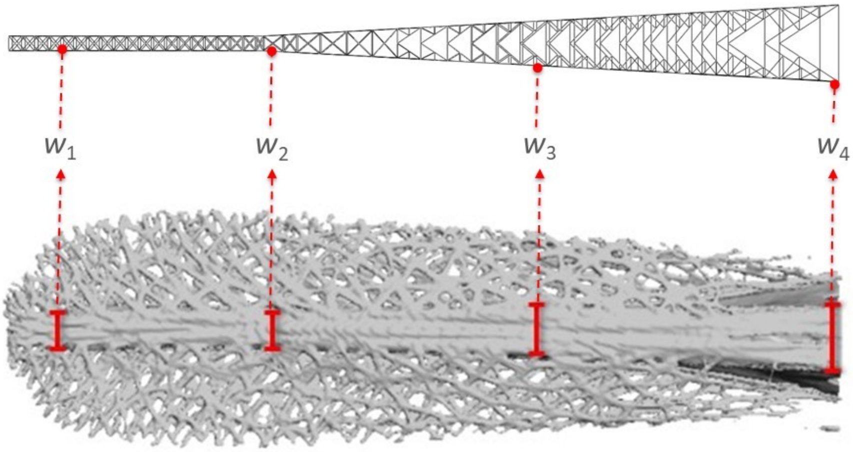

Figure 4.8 *Bio-inspired constraint* on the width of the L-beams throughout the tower height based on the width ratios seen in the main line of the network cartilage.

The angles describing the tower envelope, seen in Figure 4.8 is another design variable that can be constrained from bio-inspiration.

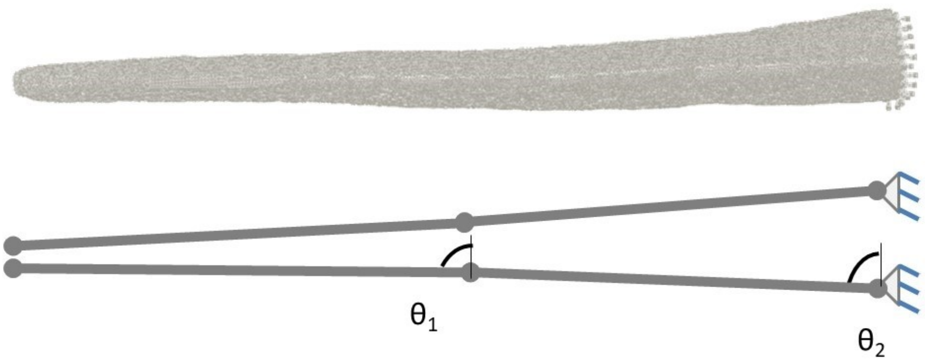

Figure 4.9 *Bio-inspired constraint* on the angles for the tower envelope.

Because the cDSP includes weighted goals that have a target value designated by the designer, a variety of different design problems can be solved using the same foundational components. For example, a tower built on the ground in an open field can have the same cDSP as a tower built on top of a building. The cDSP will have the same constraints but can be tailored around these different design problems by altering the *bounds* and *goals*. A design for a tower on top of a building may prioritize the minimization of the cost function, where an open field tower may prioritize the goal of a maximum height.

The decision-making skills of the designer also plays an important role within the exploration of a design space. Although there are multiple ranges of design variables that can be used to achieve a satisfying solution, the designer must prioritize and decide on the final solution point based on the weighting factor of each goal. There will also be cases where a feasible design space does not exist, and in this case, the designer must choose which goals will be compromised.

Applying bio-inspiration into cDSP allows researchers and designers to practically apply a multitude of other bio-inspiration research into the designs of new structures. For example, cDSP can be used with the biomechanics of teeth (see Appendix C) for use in bio-inspiration. Suppose an armor structure was built using inspiration from hard structures, like teeth, found in nature. A designer can mimic the material properties of the dentin or enamel. They can also choose to create a multilayered material, using mechanical properties, layer thicknesses, and/or chemical compositions similar to the enamel and dentin. Additional designs can also be created from the paddlefish. The rostrum model described in Chapter 3, has been used for hydrodynamic characterization.

cDSP could be implemented for a design of a novel wing design using, again using *bio-inspired constraints* from the paddlefish. From the paddlefish rostrum, to fish teeth, to a multitude of other biological structures, there many opportunities to integrate cDSP into bio-inspired materials.

A complimentary tool that the can really benefit the cDSP and bio-inspiration is TRIZ (Teoriya Resheniya Izobreatatelskikh Zadatch). TRIZ can be used in concept generation as well as problem solving (69). Genrich S. Altshuller, the creator of TRIZ, investigated invention and creativity by reviewing over 200,000 patents. Through his studies, he discovered that almost all invention problems contain at least one contradiction. He found that better inventions often hinged on how well the contradiction is resolved, an ideology that cDSP aims to do. One useful tool TRIZ includes is a list of design parameters that may possibly contradict each other. Additionally, a table is provided, showing the how improving one design parameter can negatively affect the other parameters. To help resolve these contradictions, Altshuller compiled a list of principles. The contradiction table and the list of principles will not provide the designer with an exact solution to conflicting design parameters, but they will be able to suggest promising guidelines. The tools of TRIZ are useful in the field of bio-inspiration. In fact, Vincent *et al.* (70) describe the use of TRIZ within biomimetics, and Vincent and Mann (71) describe TRIZ as a way to bridge technology and engineering with biology. The tools present within TRIZ can help identify the ways nature solves contradictory problems in terms of typical design parameters. TRIZ is also a helpful tool in cDSP, providing the designer with the extended knowledge of contradicting design parameters.

Because the cDSP is reliant on the knowledge of the designer, TRIZ can provide very helpful information when diagnosing and creating designs.

CHAPTER V

SUMMARY

Bio-inspiration is a recent emerging engineering design method involves studying designs seen within nature to create novel mechanical structures. This present work studies the rostrum, or nose, of the paddlefish, *Polyodon spathula*. The materials within the rostrum were quantified using various characterization techniques and mechanical testing equipment, and the results were used for the material model of the midline cartilage, network cartilage, and matrix tissue. A mesh and three-dimensional model were created from computed tomography images. Abaqus simulations were performed to view the stress distribution throughout the rostrum. Additionally, a design paradigm with the integration of bio-inspiration was created using the compromised Decision Support Problem.

Some notable conclusions from this work:

- Results from the mechanical testing of the midline cartilage did not show a spatial dependence, but they did exhibit stress-state and strain-rate dependence.
- A histological study on the midline cartilage was characterized as hyaline cartilage, and results matched other data for hyaline cartilage.
- Network cartilage showed a spatial dependence on hardness and modulus values.

- Matrix tissue did not exhibit a spatial dependence.
- Abaqus simulations showed that the S33 and S13 stress tensors were the primary and secondary stress tensors.
- Top-loading pressure was most detrimental to the rostrum.
- Rostrum exhibited characteristics of an early-detection system within the branches.
- Analytical solutions compare very well with finite element analysis.
- Abaqus model of a cell tower was created for analysis.
- A working cDSP was constructed for cell tower designs, and the results showed a design improvement over the original design.

CHAPTER VI

FUTURE WORK

6.1 Material model for FEA

To produce more accurate simulations shown in Chapter 3, different material models for the midline cartilage, network cartilage, and tissue should be explored. The current Ogden hyperelastic model used for the tissue and midline cartilage within the simulations can take into consideration the stress state dependence of the material (see Figure 3.4); however, it does not include strain rate dependence for the materials (see Figure 2.7). The MSU ISV polymer model has been previously used for biological materials and would be the ideal model for the materials in the rostrum. This model has been previously been used to model the brain in finite element analysis (72). The MSU ISV model takes into consideration the stress state as well as the strain rate dependence. However, this model currently works for materials that exhibit a linear elastic behavior, and unfortunately, the tissue and the midline cartilage have nonlinear elastic behavior. The ability of the ISV model to capture nonlinear elastic behavior would provide more precise simulations, and more importantly, the updated model could then be used for other nonlinear elastic materials.

6.2 Additional characterization mechanical testing of the rostrum components

Additional biomechanical testing should be performed on the components of the rostrum. The only mechanical testing done on the network cartilage were performed on dry samples. The inclusion of hydrated nanoindentation would not only provide a hydration effect of the material, but would also contribute to the overall material model and simulation accuracy. Previous research has shown the effects of hydration on the material properties of biological materials (73)(74)(75). Johnson *et al*. (66) and Trim *et al*. (67) performed mechanical tests on hydrated and dehydrated rams horns. Compared to dry samples, the wet samples of the ram horn in compression and tension showed a decrease in modulus ranging from 82% in tension to 95% in compression. Similarly, for nanoindentation performed on bone, the modulus for wet samples were 14% lower than dry samples (73). Additional characterization on the network cartilage can provide useful information into the formation of the rostrum and how it ages. Further characterization can also offer insight into the spatial dependence seen within the network cartilage.

Tension and compression samples were difficult to obtain because of the complex nature of the network cartilage. However, if larger rostrums could be obtained, it may be possible to gather larger samples to test the stress-state and strain-rate dependence of that material. Furthermore, larger rostrums could deliver tension specimens of the matrix tissue and provide the material's stress-state and strain-rate dependence.

Because the computed tomography imaging could not differentiate additional materials aside from the network cartilage and midline cartilage, the remaining rostrum components were lumped into a single material. Additional characterization and mechanical testing could be performed to distinguish the tissues that make up the matrix tissue. At the very least, the tissue between the network cartilage should be characterized because it accounts for the highest volume fraction of the matrix tissue. Additionally, for this research, the cavity within the midline cartilage (see Figure 2.1) is characterized as matrix tissue. However, the material that actually exists within the cavity is a type of fatty tissue. Characterization and mechanical testing could also be performed on this material to more accurately describe the rostrum model.

High rate tension tests were performed on the midline cartilage. However, the sample number was inadequate due to the limited rostrums available. Obtaining rostrums to perform high rate tension tests would provide additional information to describe the overall material's stress-strain behavior.

6.3 Expand cDSP tower design

The current work provides a working cDSP for a simplified tower design. Additional design variables, boundary conditions, and loads from literature research, especially on tower structure standards, should be included. With a more developed model, the solution space should be explored through ternary plots that display a feasible design space. Additionally, the cDSP in combination with the selection-DSP (68) can provide a design framework that also explores material alternatives for the L-beams.

Furthermore, the cDSP can be used with addition to robust design. Systems and designs can be complex and susceptible to a variety of uncertainty. As a result, designs need to be robust and be able to perform under a multitude of conditions. The cDSP construct forms the foundation of a robust design method called the Robust Concept Exploration Method (RCEM) (65)(76). Robust solutions offer desirable tradeoffs between expected performance and the sensitivity of the performance from deviations in design or uncontrollable variables (62). Biological structures are constructed as systems with a robust design that are typically multifunctional and perform under a variety of conditions. Incorporating robustness into a design, is another form of the inclusion bio-inspiration into mechanical systems.

6.4 cDSP, TRIZ, and bio-inspiration

The combination of cDSP, TRIZ, and bio-inspiration can be useful for research regarding design and bio-inspiration. Chapter 4, discusses the possibility of using these tools together. Additional research can result in a new design construct that can be especially valuable for biological materials.

REFERENCES

1. Meyers MA, Lin AY, Seki Y, Chen P-Y, Kad BK, Bodde S. Structural biological composites: an overview. Jom. 2006;58(7):35–41.

2. Chen P-Y, McKittrick J, Meyers MA. Biological materials: Functional adaptations and bioinspired designs. Prog Mater Sci. 2012 Nov;57(8):1492–704.

3. Meyers MA, Chen P-Y, Lin AY-M, Seki Y. Biological materials: Structure and mechanical properties. Prog Mater Sci. 2008 Jan;53(1):1–206.

4. Allison PG, Chandler MQ, Rodriguez RI, Williams BA, Moser RD, Weiss CA, et al. Mechanical properties and structure of the biological multilayered material system, Atractosteus spatula scales. Acta Biomater. 2013 Feb;9(2):5289–96.

5. Barthelat F. Biomimetics for next generation materials. Philos Trans R Soc Math Phys Eng Sci. 2007 Dec 15;365(1861):2907–19.

6. Sane SP. Bioinspiration and Biomimicry: What Can Engineers Learn from Biologists? 淡江理工學刊. 2016;19(1):1–6.

7. Da Vinci L. Codex on the flight of birds. Leonardo Da Vinci, Reynal and Co. NY; 2013.

8. Lee N, Horstemeyer MF, Rhee H, Nabors B, Liao J, Williams LN. Hierarchical Multiscale Structure-property Relationships of the Red-Bellied Woodpecker (Melanerpes carolinus) Beak. J R Soc Interface. 2014;11(96).

9. Johnson KL, Trim MW, Horstemeyer MF, Lee N, Williams LN, Liao J, et al. Geometric effects on stress wave propagation. J Biomech Eng. 2014;136(2):21023.

10. Gurgens C, Russell DF, Wilkens LA. Electrosensory avoidance of metal obstacles by the paddlefish. J Fish Biol. 2000 Aug;57(2):277–90.

11. Wilkens LA, Hofmann MH. The Paddlefish Rostrum as an Electrosensory Organ: A Novel Adaptation for Plankton Feeding. BioScience. 2007;57(5):399–407.

12. Wojtenek W, Pei X, Wilkens LA. Paddlefish strike at artificial dipoles simulating the weak electric fields of planktonic prey. J Exp Biol. 2001;204(8):1391–9.

13. Kajiura SM. Head morphology and electrosensory pore distribution of carcharhinid and sphyrnid sharks. Environ Biol Fishes. 2001;61(2):125–133.

14. Kajiura SM, Holland KN. Electroreception in juvenile scalloped hammerhead and sandbar sharks. J Exp Biol. 2002;205(23):3609–3621.

15. Jorgensen JM, Flock A, Wersall J. The Lorenzinian Ampullae of Polyodon spathula. Cell Tissue Res. 1972;130(3):362–77.

16. Rosen RA, Hale DC. Occurrence of Scarred Paddlefish in the Missouri River, South Dakota - Nebraska. Progress Fish-Cult. 1980;40(2):82–5.

17. Wilkens LA, Russell DF, Pei X, Gurgens C. The paddlefish rostrum functions as an electrosensory antenna in plankton feeding. Proc R Soc Lond B Biol Sci. 1997;264(1389):1723–1729.

18. Allen JB, Riveros G. Hydrodynamic Characterization of the *Polyodon spathula* Rostrum Using CFD. J Appl Math. 2013;2013:1–8.

19. Grande L, Bemis WE. Osteology and phylogenetic relationships of fossil and recent paddlefishes (Polyodontidae) with comments on interrelationship of Acipenseriformes. J Vertebr Paleontol. 1991;11.

20. Schneider CA, Rasband WS, Eliceiri KW. NIH Image to ImageJ: 25 years of image analysis. Nat Methods. 2012 Jun 28;9(7):671–5.

21. Porter ME, Long JH. Vertebrae in compression: Mechanical behavior of arches and centra in the gray smooth-hound shark (*Mustelus californicus*). J Morphol. 2009;NA-NA.

22. Yamada H, Evans F. Strength of biological materials. 1st ed. 1970.

23. Stockwell RA. The cell density of human articular and costal cartilage. J Anat. 1967;101(Pt 4):753.

24. Barbero A, Grogan S, Schäfer D, Heberer M, Mainil-Varlet P, Martin I. Age related changes in human articular chondrocyte yield, proliferation and post-expansion chondrogenic capacity. Osteoarthritis Cartilage. 2004 Jun;12(6):476–84.

25. Courtland H-W. Comparative equilibrium mechanical properties of bovine and lamprey cartilaginous tissues. J Exp Biol. 2003 Apr 15;206(8):1397–408.

26. Eurell JA, Frappier BL. Dellmann's Textbook of Veterinaru Histology. 2013.

27. Gorenšek M, Joksimović Č, Kregar-Velikonja N, Gorenšek M, Knežević M, JERAS VP, et al. Nucleus pulposus repair with cultured autologous elastic cartilage derived chondrocytes. Cell Mol Biol Lett. 2004;9(2):363–373.

28. Soltz MA, Ateshian GA. A conewise linear elasticity mixture model for the analysis of tension-compression nonlinearity in articular cartilage. J Biomech Eng. 2000;122(6):576–586.

29. Huang C-Y, Soltz MA, Kopacz M, Mow VC, Ateshian GA. Experimental Verification of the Roles of Intrinsic Matrix Viscoelasticity and Tension-Compression Nonlinearity in the Biphasic Response of Cartilage. J Biomech Eng. 2003;125(1):84.

30. Huang C-Y, Stankiewicz A, Ateshian GA, Mow VC. Anisotropy, inhomogeneity, and tension–compression nonlinearity of human glenohumeral cartilage in finite deformation. J Biomech. 2005 Apr;38(4):799–809.

31. Allison PG, Deang JF, Diaz AJ, Poda AR, Hoover J., Horstemeyer MF, et al. Characterization of paddlefish (Polyodon spathula) rostrum stellate bones. Bioinspired Biomim Nanobiomaterials. 2013;3(1):63–8.

32. Oliver WC, Pharr GM. An improved technique for determining hardness and elastic modulus using load and displacement sensing indentation experiments. J Mater Res. 1992;7(6):1564–1583.

33. Kittiphattanabawon P, Benjakul S, Visessanguan W, Shahidi F. Isolation and characterization of collagen from the cartilages of brownbanded bamboo shark (Chiloscyllium punctatum) and blacktip shark (Carcharhinus limbatus). LWT - Food Sci Technol. 2010 Jun;43(5):792–800.

34. Jeevithan E, Wu W, Nanping W, Lan H, Bao B. Isolation, purification and characterization of pepsin soluble collagen isolated from silvertip shark (Carcharhinus albimarginatus) skeletal and head bone. Process Biochem. 2014 Oct;49(10):1767–77.

35. Reid SA, Boyde A. Changes in the mineral desnity distribution in human bone with age: Image analysis using backscattered electrons in th SEM. J Bone Miner Res. 1987;2(1):13–22.

36. Khosla S, Riggs BL, Atkinson EJ, Oberg AL, McDaniel LJ, Holets M, et al. Effects of sex and age on bone microstructure at the ultradistal radius: a population-based noninvasive in vivo assessment. J Bone Miner Res. 2006;21(1):124–31.

37. McCalden RW, McGeough JA, Barker MB. Age-related changes in the tensile properties of coritcal bone. The relative importance of changes in porosity, mineralization, and microstrucuture. J Bone Jt Surg. 1993;75(8):1993–1205.

38. Wang X, Shen X, Li X, Agrawal CM. Age-related changes in the collagen network and toughness of bone. Bone. 2002;31(1):1–7.

39. Currey JD. Bones: Structure and Mechanics. 2002.

40. Dean MN, Summers AP. Mineralized cartilage in the skeleton of chondrichthyan fishes. Zoology. 2006 May;109(2):164–8.

41. Ross ST, Brenneman WM. The Inland Fishes of Mississippi. 2001. 81-83 p.

42. Skomal G. The Shark Handbook: The Essential Guide for Undersetanding the Sharks of the World. 2008.

43. Miller K, Chinzei K. Constitutive modelling of brain tissue: Experiment and theory. J Biomech. 1997;30(11):1115–21.

44. Chaudhry H, Bukiet B, Ji Z, Stecco A, Findley T. Deformations Experienced in the Human Skin, Adipose Tissue, and Fascia in Osteopathic Manipulative Medicine. J Am Osteopath Assoc. 2014 Oct;114(10):780–7.

45. Zeng Y-J, Sun X, Yang J, Wu W, Xu X, Yan Y. Mechanical properties of nasal fascia and periosteum. Clin Biomech. 2003 Oct;18(8):760–4.

46. Pettersen F-J, Høgetveit JO. From 3D tissue data to impedance using Simpleware ScanFE+IP and COMSOL Multiphysics – a tutorial. J Electr Bioimpedance [Internet]. 2011 Mar 7 [cited 2017 May 30];2(1). Available from: https://www.journals.uio.no/index.php/bioimpedance/article/view/173

47. Doube M, Kłosowski MM, Arganda-Carreras I, Cordelières FP, Dougherty RP, Jackson JS, et al. BoneJ: Free and extensible bone image analysis in ImageJ. Bone. 2010 Dec;47(6):1076–9.

48. Lin DC, Shreiber DI, Dimitriadis EK, Horkay F. Spherical indentation of soft matter beyond the Hertzian regime: numerical and experimental validation of hyperelastic models. Biomech Model Mechanobiol. 2009 Oct;8(5):345–58.

49. Hu T, Desai JP. Characterization of soft-tissue material properties: Large deformation analysis. Lect Notes Comput Sci. 2004;3078:28–37.

50. Natali AN, Pavan PG, Carniel EL, Lucisano ME, Taglialavoro G. Anisotropic elasto-damage constitutive model for the biomechanical analysis of tendons. Med Eng Phys. 2005 Apr;27(3):209–14.

51. Ogden RW, Saccomandi G, Sgura I. Fitting hyperelastic models to experimental data. Comput Mech. 2004 Nov;34(6):484–502.

52. Ogden RW. Large deformation isotropic elasticity - on the correlation of theory and experiment for incompressible rubberlike solids. Proc R Soc Lond Ser B Math Phys Sci. 1972;326(1567):565–84.

53. Xia R. Relation between mean and maximum velocities in a natural river. J Hydraul Eng. 1997;123(8):720–723.

54. Bayraktar HH, Morgan EF, Niebur GL, Morris GE, Wong EK, Keaveny TM. Comparison of the elastic and yield properties of human femoral trabecular and cortical bone tissue. J Biomech. 2004 Jan;37(1):27–35.

55. Vahey JW, Lewis JL, Vanderby R. Elastic moduli, yield stress, and ultimate stress of cancellous bone in the canine proximal femur. J Biomech. 1987;20(1):29–33.

56. Shea K, Smith IF. Improving full-scale transmission tower design through topology and shape optimization. J Struct Eng. 2006;132(5):781–790.

57. Martín P, Elena VB, Loredo-Souza AM, Camaño EB. Experimental study of the effects of dish antennas on the wind loading of telecommunication towers. J Wind Eng Ind Aerodyn. 2016 Feb;149:40–7.

58. Beck AT, Verzenhassi CC. Risk optimization of a steel frame communications tower subject to tornado winds. Lat Am J Solids Struct. 2008;5(3):187–203.

59. Mulherin ND. Atmospheric icing and communication tower failure in the United States. Cold Reg Sci Technol. 1998;27(2):91–104.

60. Smith BW. Communication structures. Thomas Telford; 2007.

61. Mistree F, Hughes OF, Bras BA. The compromise decision support problem and the adaptive linear programmy algorithm. Struct Optim Status Promise. 1993;247–86.

62. McDowell DL, Panchal JH, Choi HJ, Seepersad CC, Allen JK, Mistree F. Integrated design of multiscale, multifunctional materials and products. Butterworth-Heinemann; 2009.

63. Mistree F, Smith WF, Bras BA, Allen JK, Muster D. Mistree F Decision based design A contemporary paradigm for ship design.pdf. In: THE SOCEITY OF NAVAL ARCHITECTS AND MARINE ENGINEERS. 1990.

64. Shukla R, Kulkarni NH, Gautham BP, Singh AK, Mistree F, Allen JK, et al. Design Exploration of Engineered Materials, Products, and Associated Manufacturing Processes. JOM. 2015 Jan;67(1):94–107.

65. Koch PN, Allen JK, Mistree F, Barlow A. Facilitating Concept Exploration for Configuring Turbine Propulsion Systems. J Mech Des. 1998;120(4):702–706.

66. ANSI/TIA-222-G. Structural Standards for Steel Antenna Towers and Antenna Supporting Structures. Telecommun Ind Assoc TIA USA. 2006;

67. Trylon TSF Inc. Stocked Towers Catalog. 2017;4(3):83–105.

68. Fernandez MG, Seepersad CC, Rosen DW, Allen JK, Mistree F. Utility-based decision support for selection in engineering design. In: ASME DETC Design Automation Conference. 2001.

69. Yang K, El-Haik BS. Design for six sigma. 2nd ed. New York: McGraw-Hill; 2009.

70. Vincent JFV, Bogatyreva OA, Bogatyrev NR, Bowyer A, Pahl A-K. Biomimetics: its practice and theory. J R Soc Interface. 2006 Aug 22;3(9):471–82.

71. Vincent JFV, Mann DL. Systematic technology transfer from biology to engineering. Philos Trans R Soc Math Phys Eng Sci. 2002 Feb 15;360(1791):159–73.

72. Prabhu R, Horstemeyer MF, Tucker MT, Marin EB, Bouvard JL, Sherburn JA, et al. Coupled experiment/finite element analysis on the mechanical response of porcine brain under high strain rates. J Mech Behav Biomed Mater. 2011 Oct;4(7):1067–80.

73. Rho J-Y, Pharr GM. Effects of drying on the mechanical properties of bovine femur measured by nanoindentation. J Mater Sci Mater Med. 1999;10(8):485–488.

74. Bushby AJ, Ferguson VL, Boyde A. Nanoindentation of bone: Comparison of specimens tested in liquid and embedded in polymethylmethacrylate. J Mater Res. 2004 Jan;19(1):249–59.

75. Balooch M, Wu-Magidi IC, Balazs A, Lundkvist AS, Marshall SJ, Marshall GW, et al. Viscoelastic properties of demineralized human dentin measured in water with atomic force microscope (AFM)-based indentation. J Biomed Mater Res. 1998;40(4):539–544.

76. Simpson T, Allen J, Chen W, Mistree F. Conceptual design of a family of products through the use of the Robust Concept Extrapolation Method. In American Institute of Aeronautics and Astronautics; 1996 [cited 2017 Nov 12]. Available from: http://arc.aiaa.org/doi/10.2514/6.1996-4161

77. Bigelow HB, Shroeder WC. Fishes of the Gulf of Maine. U.S. Fish and Wildlife Service; 1953. 416 p. (Fisher Bulletin of the Fish and Wildlife Service; vol. 53).

78. Fernandez LPH, Motta PJ. Trophic consequences of differential performance: Ontogeny of oral jaw-crushing performance in the sheepshead, Archosargus probatocephalus (Teleostei, Sparidae). J Zool. 1997;243(4):737–756.

79. Ogawa M, Portier RJ, Moody MW, Bell J, Schexnayder MA, Losso JN. Biochemical properties of bone and scale collagens isolated from the subtropical fish black drum (Pogonia cromis) and sheepshead seabream (Archosargus probatocephalus). Food Chem. 2004 Dec;88(4):495–501.

80. Overstreet RM, Heard RW. Food contents of six commercial fishes from Mississippi sound. Gulf Res Rep. 1982;7(2):137–49.

81. Sedberry GR. Feeding habits of sheepshead, Archosargus probatocephalus, in offshore reef habits of the southeastern continental shelf. Northeast Gulf Sci. 1987;9(1):29–37.

82. He LH, Swain MV. Understanding the mechanical behaviour of human enamel from its structural and compositional characteristics. J Mech Behav Biomed Mater. 2008 Jan;1(1):18–29.

83. Braly A, Darnell LA, Mann AB, Teaford MF, Weihs TP. The effect of prism orientation on the indentation testing of human molar enamel. Arch Oral Biol. 2007 Sep;52(9):856–60.

84. Cate T. Oral histology: development, structure, and function. 4th ed. St. Louis, MO: Mosby; 1994.

85. Habelitz S, Marshall GW, Balooch M, Marshall SJ. Nanoindentation and storage of teeth. J Biomech. 2002;35(7):995–998.

86. Cuy JL, Mann AB, Livi KJ, Teaford MF, Weihs TP. Nanoindentation mapping of the mechanical properties of human molar tooth enamel. Arch Oral Biol. 2002;47(4):281–291.

87. Jeng Y-R, Lin T-T, Hsu H-M, Chang H-J, Shieh D-B. Human enamel rod presents anisotropic nanotribological properties. J Mech Behav Biomed Mater. 2011 May;4(4):515–22.

88. Enax J, Prymak O, Raabe D, Epple M. Structure, composition, and mechanical properties of shark teeth. J Struct Biol. 2012 Jun;178(3):290–9.

89. Brunet F, Allan DR, Redfern SAT, Angel RJ, Miletich R, Reichmann HJ, et al. Compressibility and thermal expansivity of synthetic apatites, Ca5(PO4)3X with X = OH, F and Cl. Eur J Mineral. 1999 Nov 29;11(6):1023–36.

90. Gardner TN, Elliott JC, Sklar Z, Briggs GAD. Acoustic microscope study of the elastic properties of fluorapatite and hydroxyapatite, tooth enamel and bone. J Biomech. 1992;25(11):1265–1277.

91. Kinney JH, Balooch M, Marshall SJ, Marshall GW, Weihs TP. Hardness and Young's modulus of human peritubular and intertubular dentine. Arch Oral Biol. 1996;41(1):9–13.

92. Zysset PK, Edward Guo X, Edward Hoffler C, Moore KE, Goldstein SA. Elastic modulus and hardness of cortical and trabecular bone lamellae measured by nanoindentation in the human femur. J Biomech. 1999 Oct;32(10):1005–12.

93. Rho J-Y, Tsui TY, Pharr GM. Elastic properties of human cortical and trabecular lamellar bone measured by nanoindentation. Biomaterials. 1997;18(20):1325–30.

94. Chen P-Y, Schirer J, Simpson A, Nay R, Lin Y-S, Yang W, et al. Predation versus protection: Fish teeth and scales evaluated by nanoindentation. J Mater Res. 2012 Jan;27(1):100–12.

95. Whitenack LB, Simkins DC, Motta PJ, Hirai M, Kumar A. Young's modulus and hardness of shark tooth biomaterials. Arch Oral Biol. 2010 Mar;55(3):203–9.

96. Fisher RA. Frequency distribution of the values of the correlation coefficient in samples from an indefinitely large population. Biometrika. 1915;10(4):507–21.

97. Suga S, Taki Y, Wada K. Fluoride concentration in the teeth of perciform fishes and its phylogenetic significance. Jpn J Ichthyol. 1983;30(1):81–93.

98. Komabayashi T, Nonomura G, Watanabe LG, Marshall GW, Marshall SJ. Dentin tubule numerical density variations below the CEJ. J Dent. 2008 Nov;36(11):953–8.

99. Jakiel J, Szyszkowska A, Malicka M, Rahnama M, Dawidowicz L. Evaluation of dentinal tubules of dentin of the roots of necrotic teeth by means of scanning electron microscope. Pol Ann Med [Internet]. 2016 Dec [cited 2017 Feb 7]; Available from: http://linkinghub.elsevier.com/retrieve/pii/S1230801316300662

100. Pashley D, Atsuko O, Parham P. The relationship between dentin microhardness and tubule density. Dent Traumatol. 1985;1(5):176–9.

101. Voigt W. On the relation between the elasticity constants of isotropic bodies. Ann Phys Chem. 1889;274:573–87.

102. Sumikawa DA, Marshall GW, Gee L, Marshall SJ. Microstructure of primary tooth dentin. Pediatr Dent. 1999;21(7):439–444.

103. Marshall GW, Balooch M, Gallagher RR, Gansky SA, Marshall SJ. Mechanical properties of the dentinoenamel junction: AFM studies of nanohardness, elastic modulus, and fracture. J Biomed Mater Res A. 2001;54(1):87–95.

104. Pashley D, Okabe A, Parham P. The relationship between dentin microhardness and tubule density. Dent Traumatol. 1985;1(5):176–179.

105. Frazzetta TH. The mechanics of cutting and the form of shark teeth (Chondrichthyes, Elasmobranchii). Zoomorphology. 1988;108(2):93–107.

106. Ramsay JB, Wilga CD. Morphology and mechanics of the teeth and jaws of white-spotted bamboo sharks (Chiloscyllium plagiosum). J Morphol. 2007 Aug;268(8):664–82.

107. Diamond JM. Animal behavior: How great white sharks, sabre-toothed cats and soldiers kill. Nature. 1986;322:773–4.

108. Nico LG, Taphorn DC. Food habits of piranhas in the low llanos of Venezuela. 1988;311–21.

109. Atkins T. The Science and Engineering of Cutting: The Mechanics and Processes of Separating, Scratching and Puncturing Biomaterials, Metals and Non-metals. Butterworth-Heinemann; 2009.

110. Lian J, Wang J. Microstructure and Mechanical Anisotropy of Crab Cancer Magister Exoskeletons. Exp Mech. 2014 Feb;54(2):229–39.

111. Raman S, Kumar R. Construction and nanomechanical properties of the exoskeleton of the barnacle, Amphibalanus reticulatus. J Struct Biol. 2011 Dec;176(3):360–9.

112. Lee SW, Kim GH, Choi CS. Characteristic crystal orientation of folia in oyster shell, Crassostrea gigas. Mater Sci Eng C. 2008 Mar;28(2):258–63.

113. Cohen L, Dean M, Shipov A, Atkins A, Monsonego-Ornan E, Shahar R. Comparison of structural, architectural and mechanical aspects of cellular and acellular bone in two teleost fish. J Exp Biol. 2012 Jun 1;215(11):1983–93.

APPENDIX A

ROSTRUM SIMULATION RESULTS

The following appendix provides a detailed figure list showing the stress distribution for each stress tensor resulting from the different boundary conditions. Figure A.1 shows the viewpoints used in the following figure captions. Table A.1 provides a detailed list describing the boundary conditions, stress tensor, and viewpoints used for each figure within the appendix.

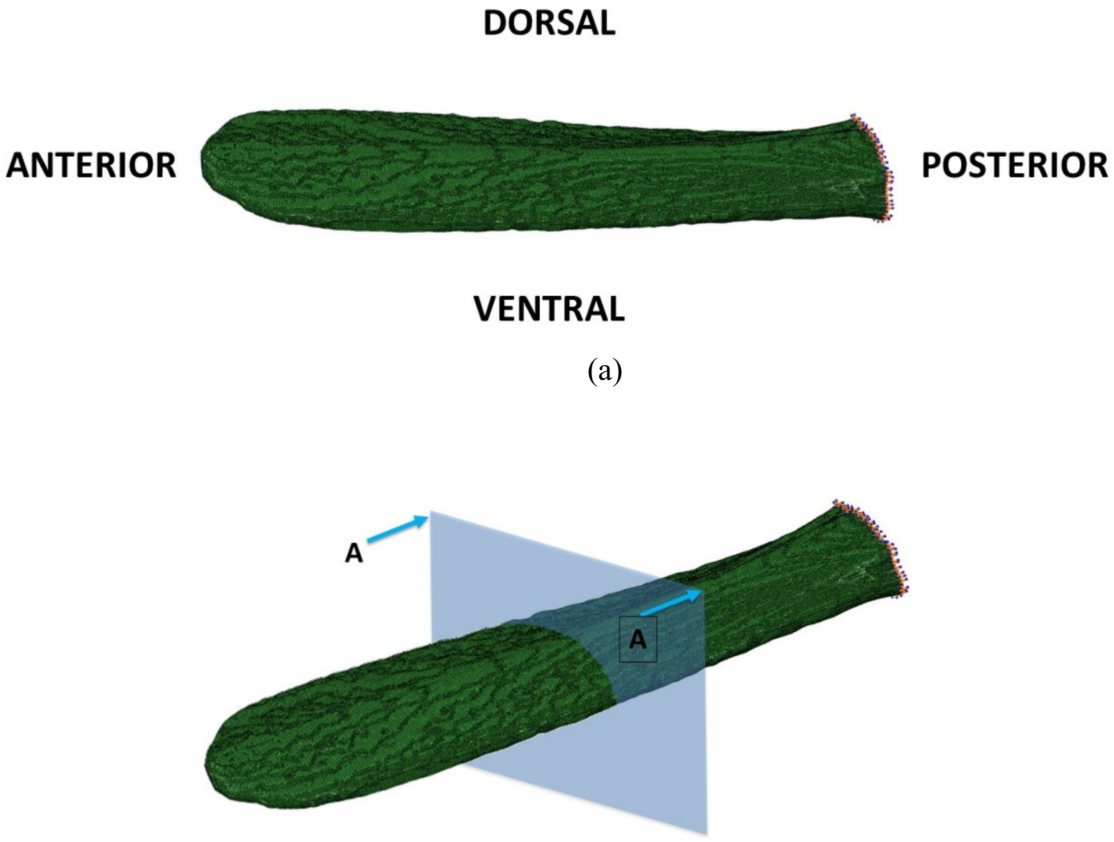

(a)

(b)

Figure A.1 Labeled view points for Appendix A figures.

(a) Labeled sides of the paddlefish rostrum. (b) Section A-A which will be referred to as the 'sectioned view' of the rostrum.

Table A.1 Detailed list of figures within Appendix A.

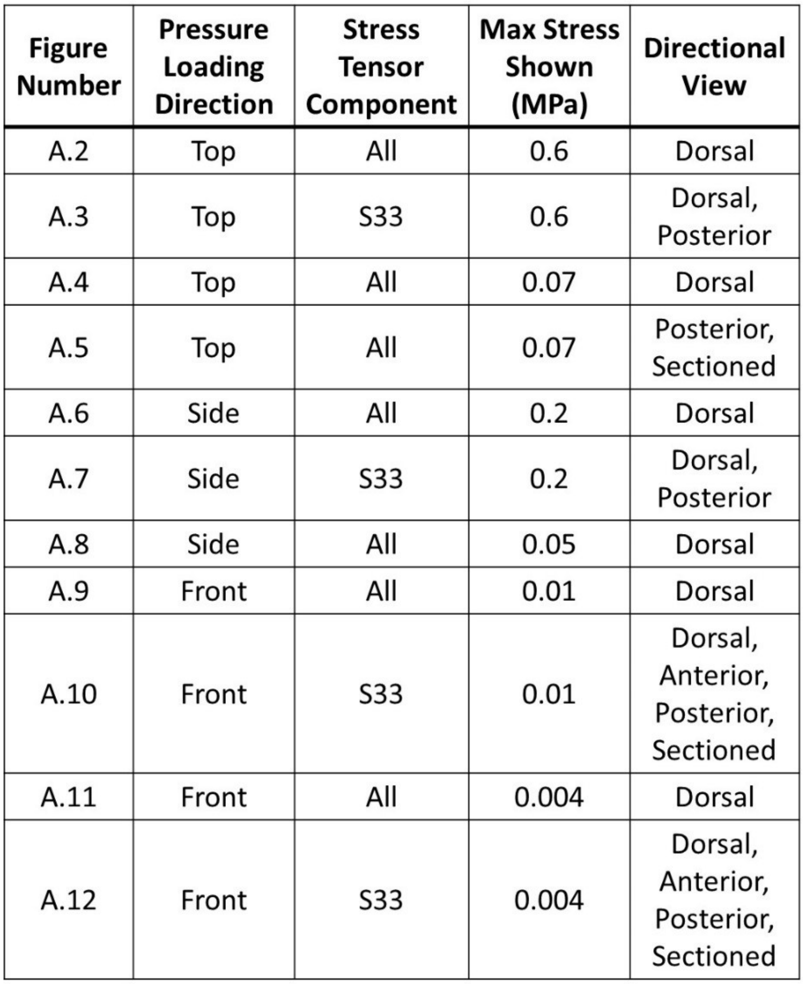

Figure Number	Pressure Loading Direction	Stress Tensor Component	Max Stress Shown (MPa)	Directional View
A.2	Top	All	0.6	Dorsal
A.3	Top	S33	0.6	Dorsal, Posterior
A.4	Top	All	0.07	Dorsal
A.5	Top	All	0.07	Posterior, Sectioned
A.6	Side	All	0.2	Dorsal
A.7	Side	S33	0.2	Dorsal, Posterior
A.8	Side	All	0.05	Dorsal
A.9	Front	All	0.01	Dorsal
A.10	Front	S33	0.01	Dorsal, Anterior, Posterior, Sectioned
A.11	Front	All	0.004	Dorsal
A.12	Front	S33	0.004	Dorsal, Anterior, Posterior, Sectioned

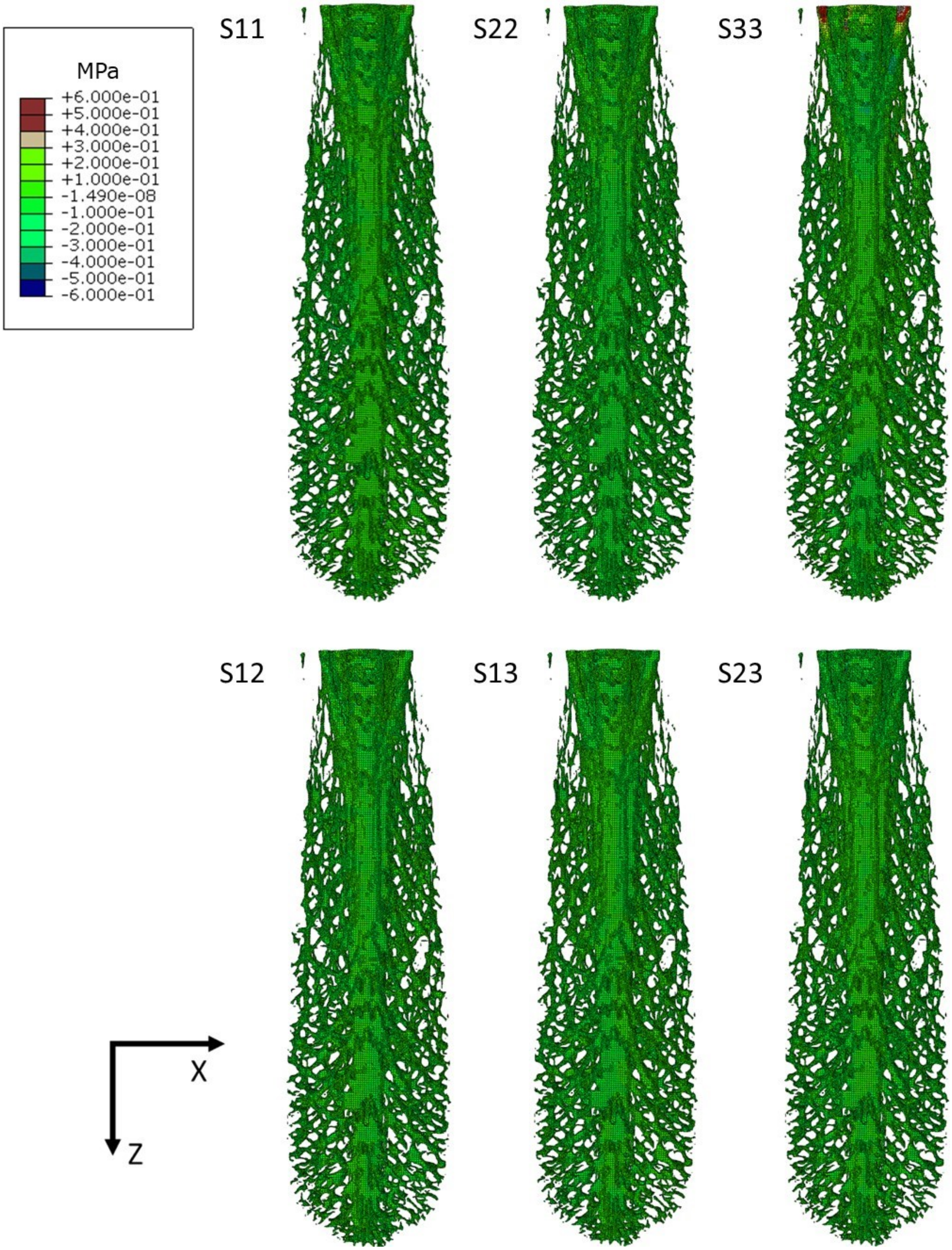

Figure A.2 Dorsal view of the stress distribution for stress tensor components from top-loading pressure simulation. Maximum stress shown is 0.6 MPa.

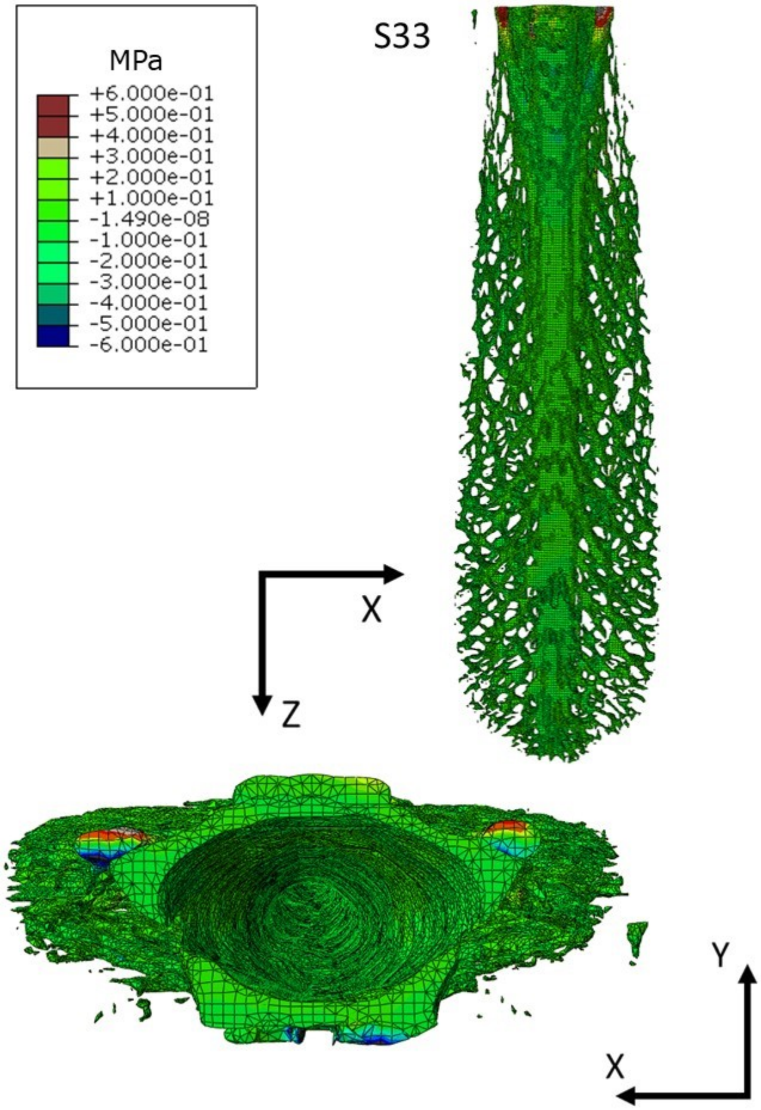

Figure A.3 Dorsal and posterior view of the stress distribution for the S33 tensor component from top-loading pressure simulation. Maximum stress shown is 0.6 MPa.

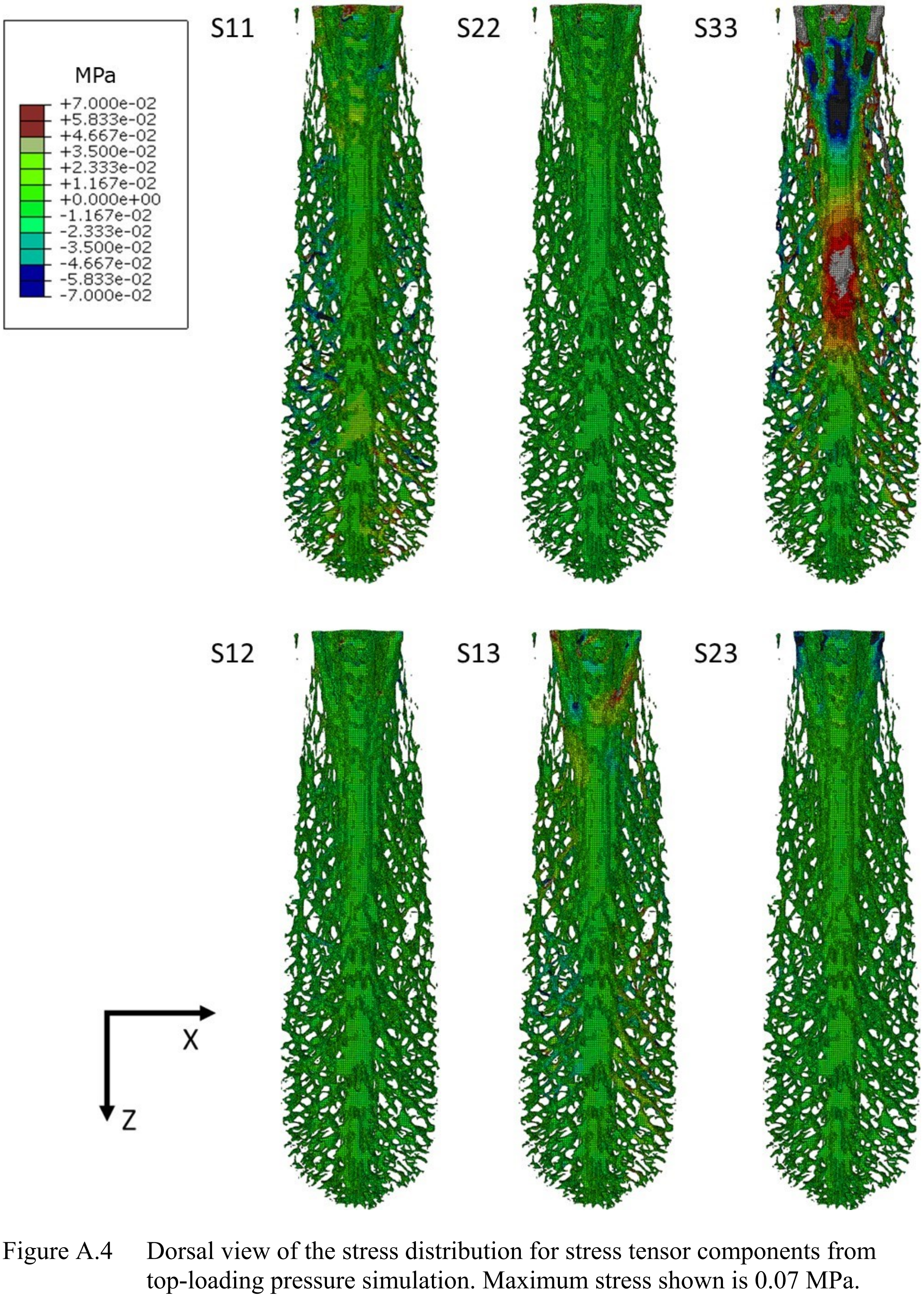

Figure A.4 Dorsal view of the stress distribution for stress tensor components from top-loading pressure simulation. Maximum stress shown is 0.07 MPa.

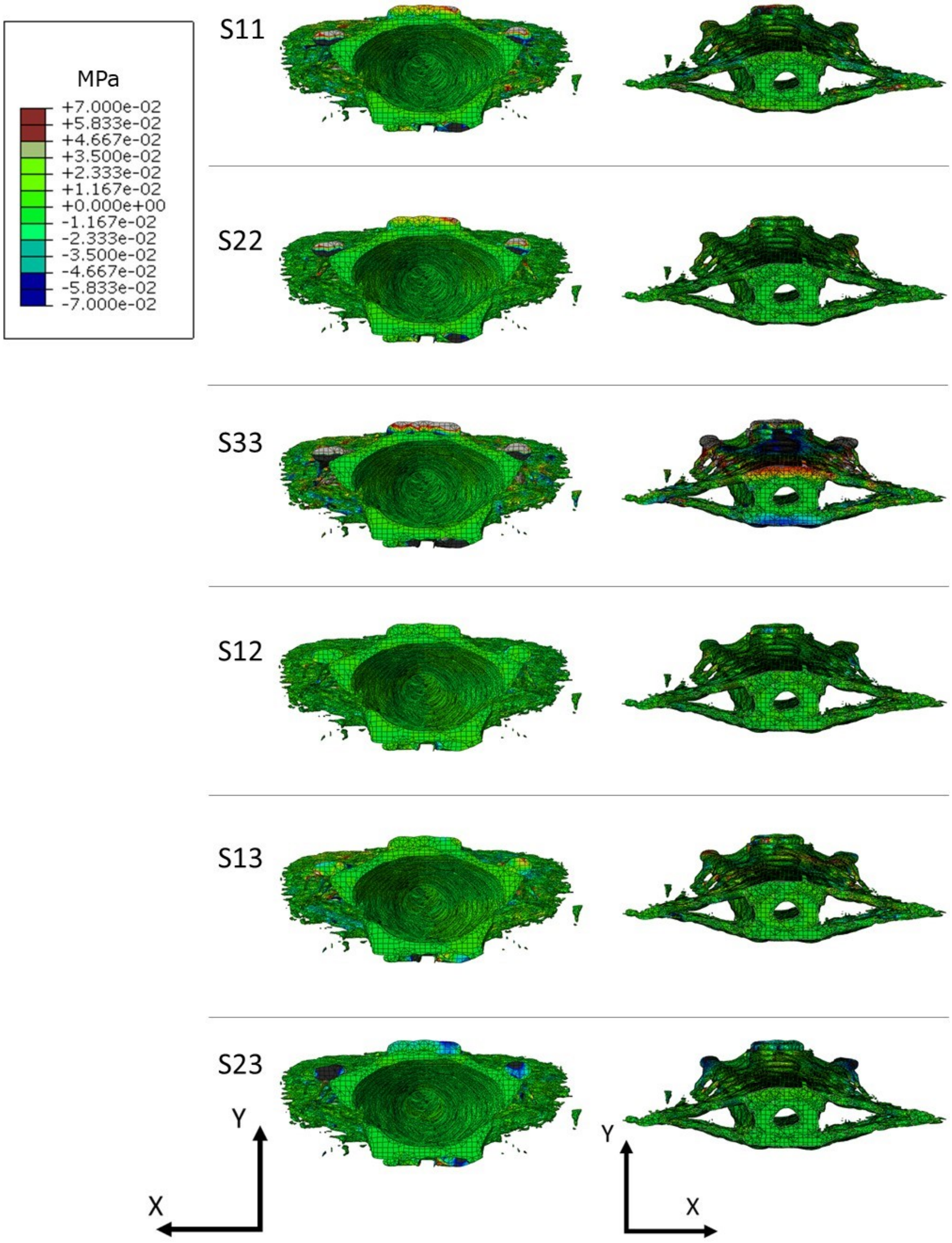

Figure A.5 Posterior view (left) and sectioned view (right) for stress tensor components from top-loading pressure simulation. Maximum stress shown is 0.07 MPa.

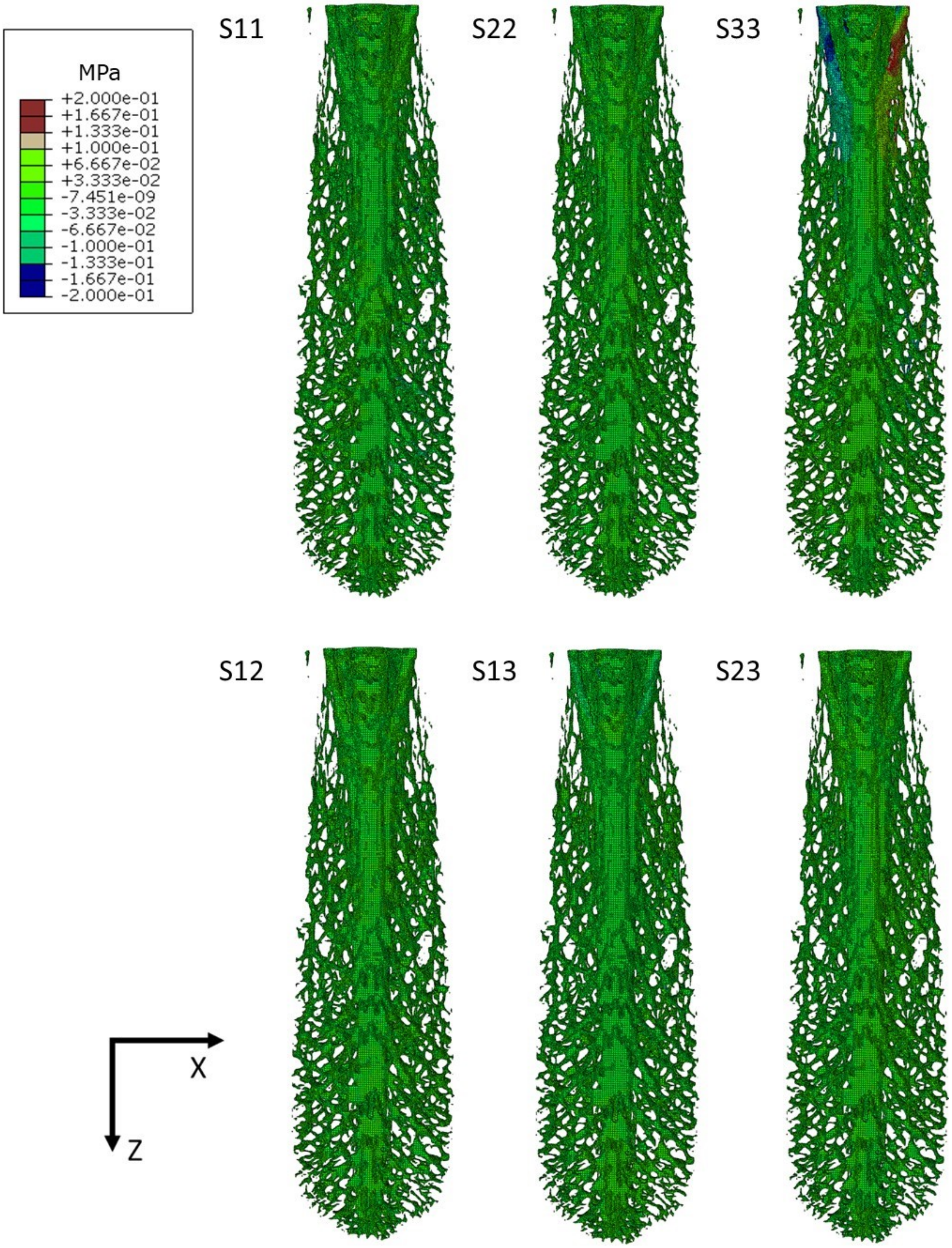

Figure A.6 Dorsal view of the stress distribution for stress tensor components from side-loading pressure simulation. Maximum stress shown is 0.2 MPa.

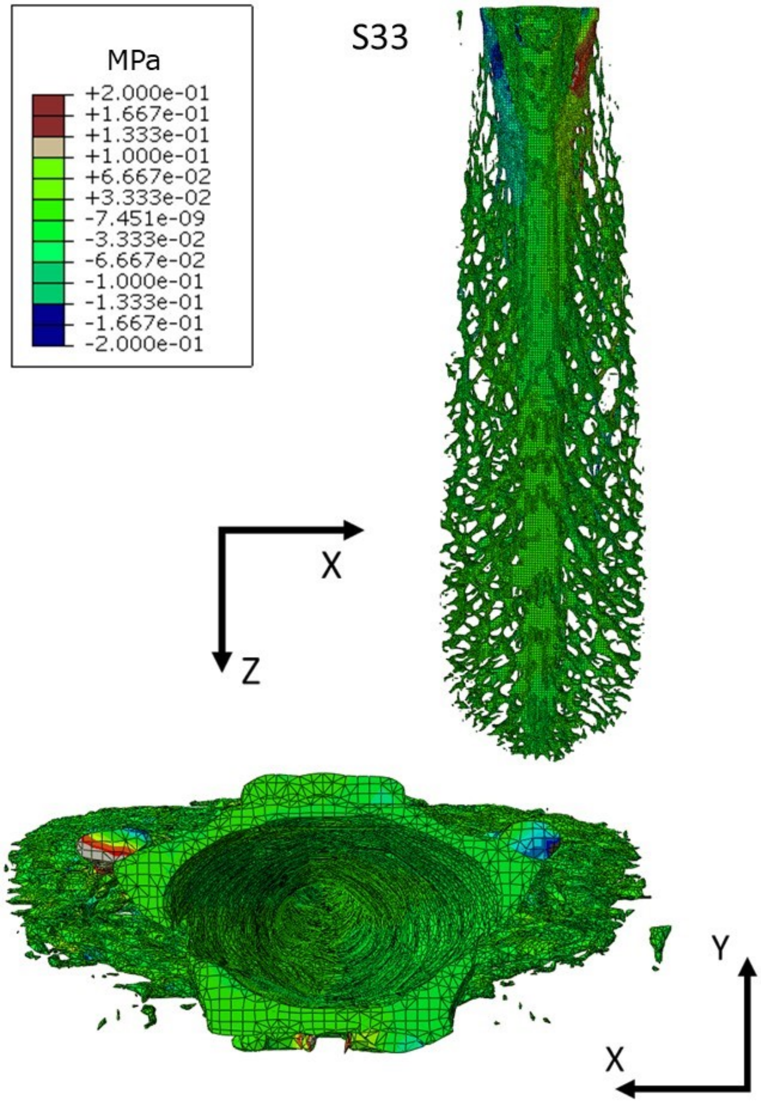

Figure A.7 Dorsal and posterior view of the stress distribution for the S33 tensor component from side-loading pressure simulation. Maximum stress shown is 0.2 MPa.

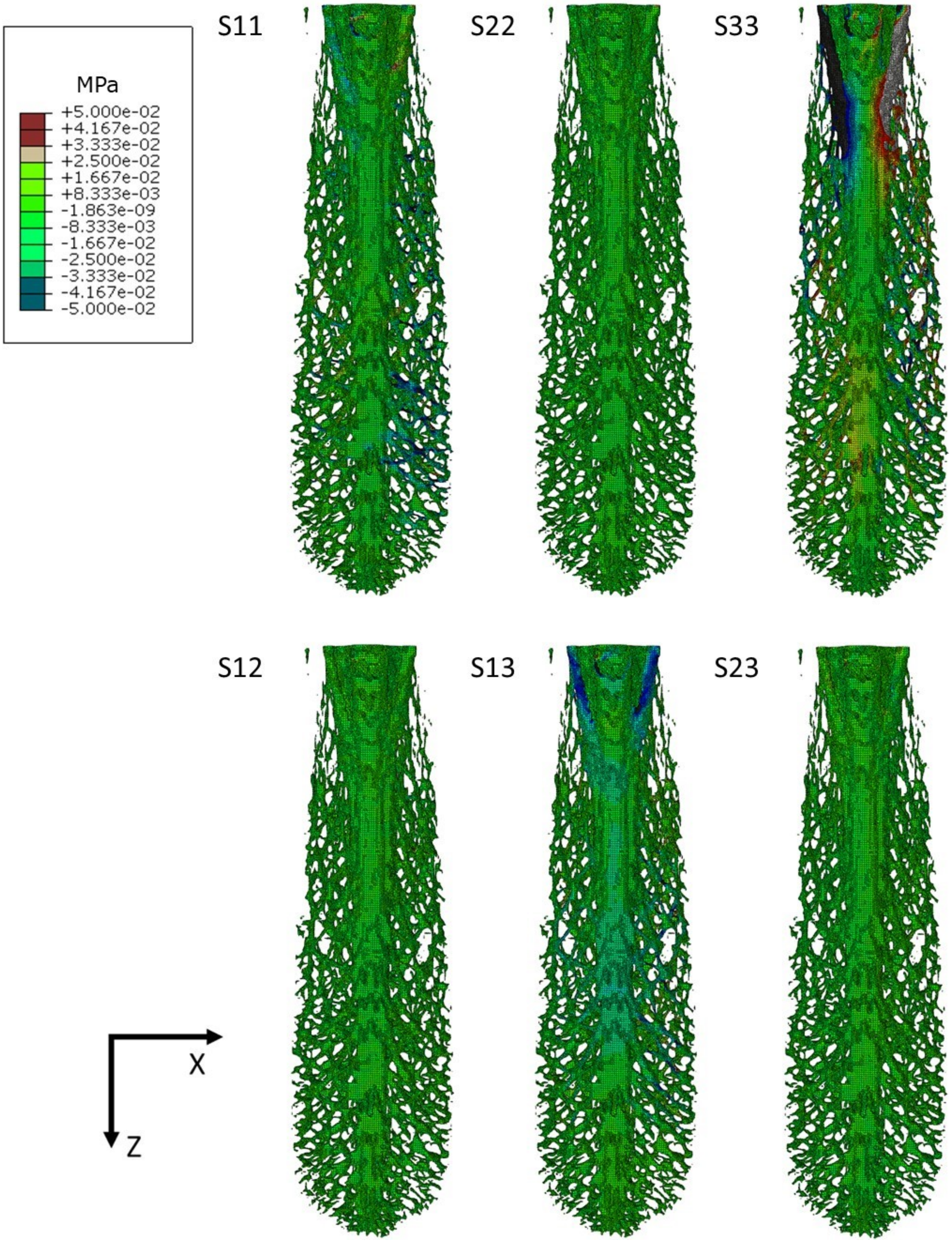

Figure A.8 Dorsal view of the stress distribution for stress tensor components from side-loading pressure simulation. Maximum stress shown is 0.05 MPa.

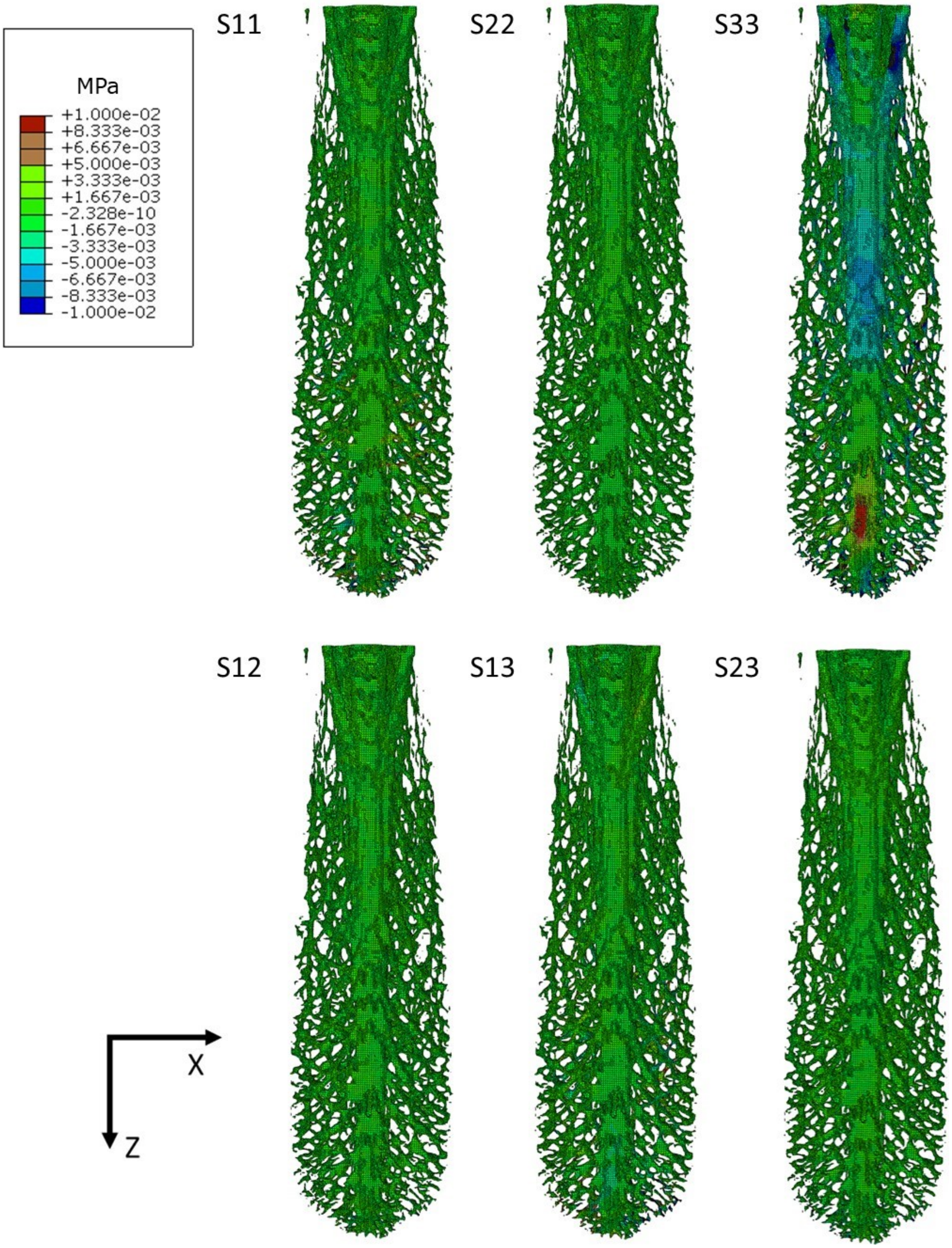

Figure A.9 Dorsal view of the stress distribution for stress tensor components from front-loading pressure simulation. Maximum stress shown is 0.01 MPa.

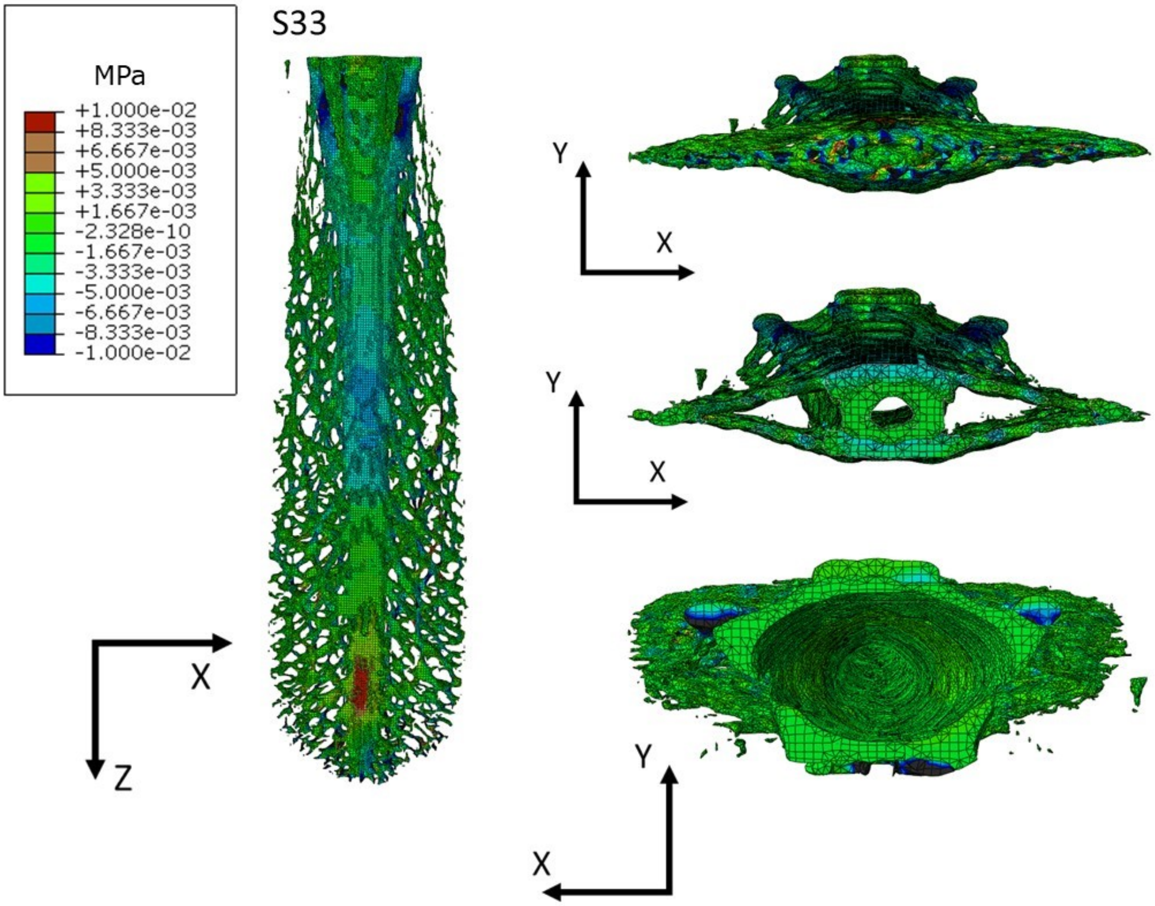

Figure A.10 Dorsal, anterior, posterior, and sectioned view for the S33 stress tensor components from front-loading pressure simulation. Maximum stress shown is 0.01 MPa.

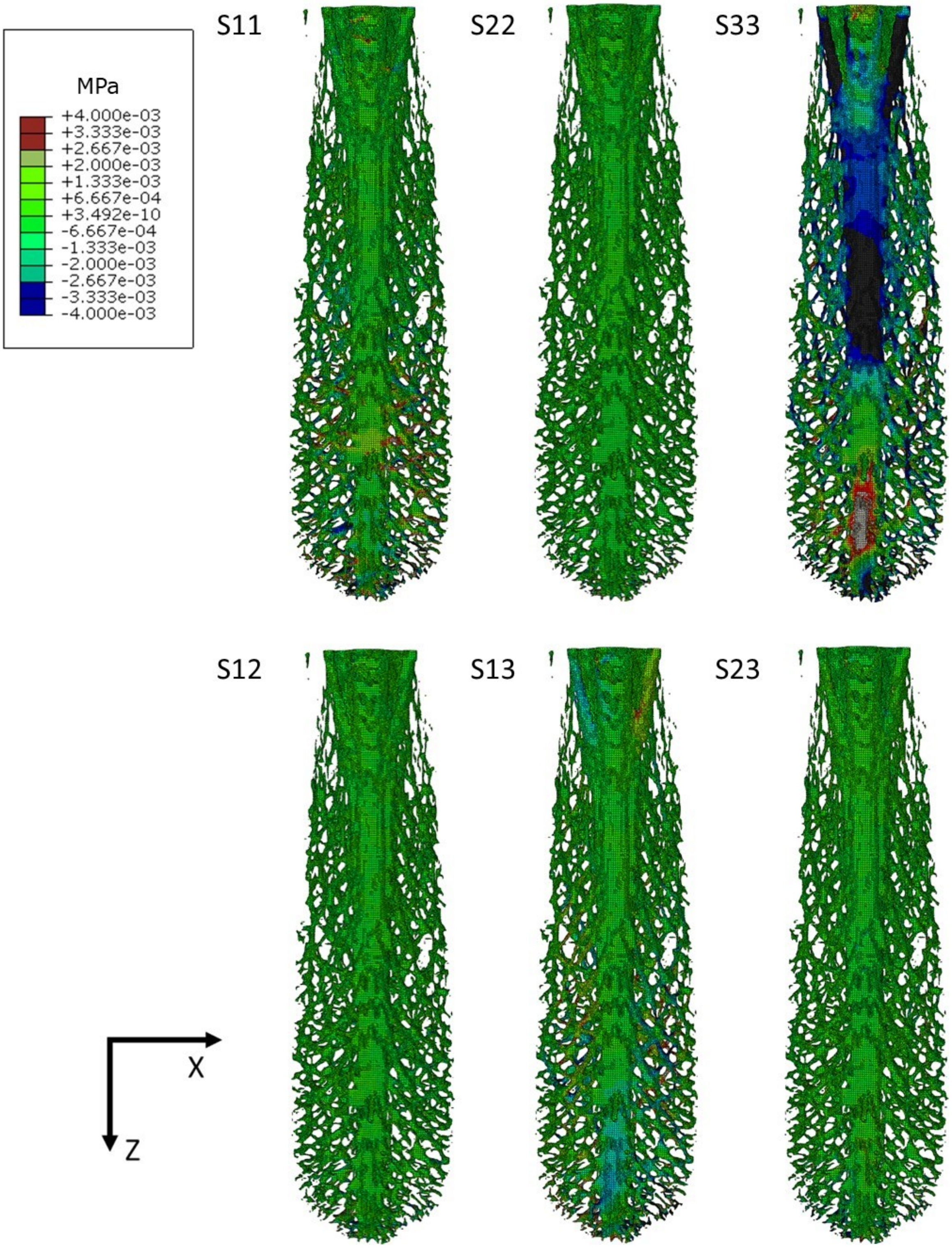

Figure A.11 Dorsal view of the stress distribution for stress tensor components from front-loading pressure simulation. Maximum stress shown is 0.004 MPa.

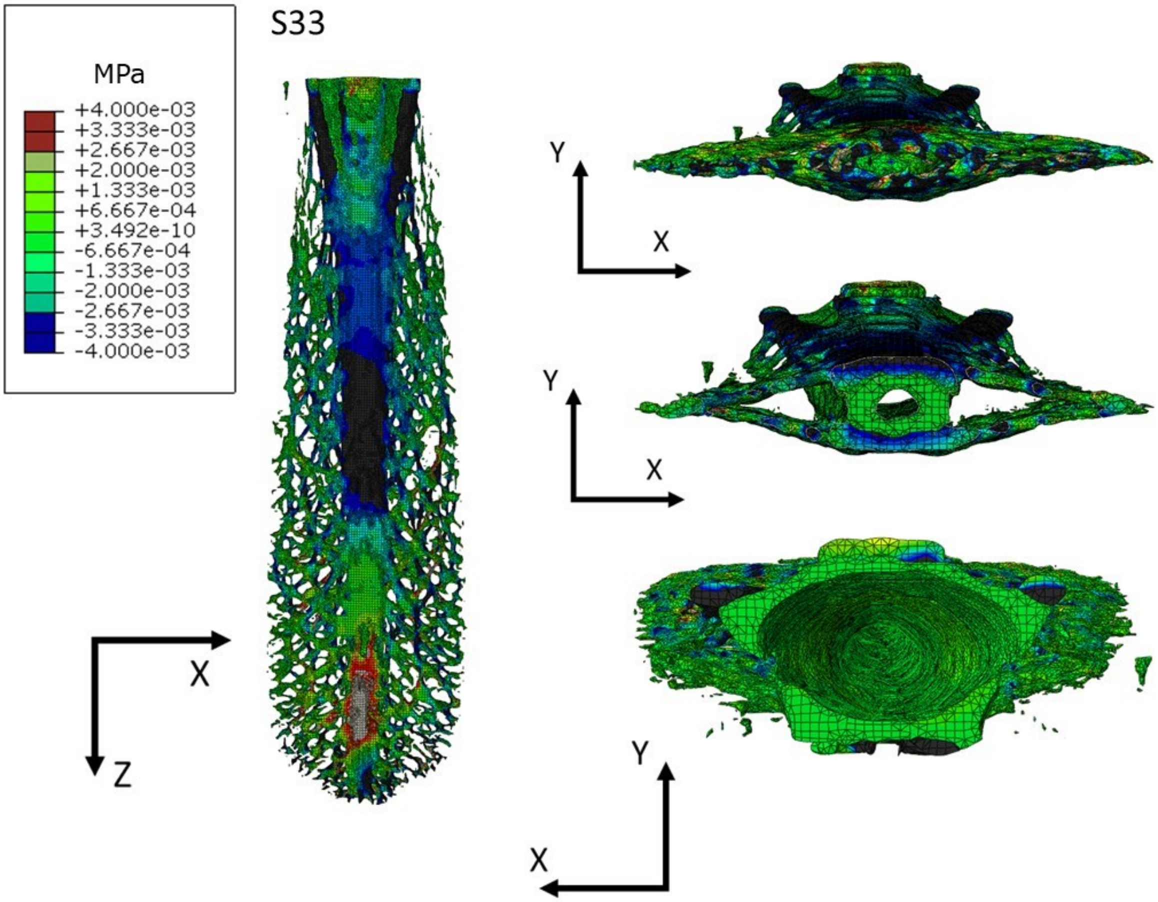

Figure A.12 Dorsal, anterior, posterior, and sectioned view for the S33 stress tensor components from front-loading pressure simulation. Maximum stress shown is 0.004 MPa.

APPENDIX B

SUPPLEMENTARY FILES FOR cDSP CONSTRUCT

The following two sections present the files and code used for the cell tower cDSP problem

B.1 Fortran file

```
C C
C
      SUBROUTINE USRINP (NDESV, NINP, NOUT, DESVAR)
C
C***  DUMMY ROUTINE.  Not used.
C
      INTEGER NDESV, NINP, NOUT
      REAL DESVAR(NDESV)
C
      RETURN
      END



      SUBROUTINE USROUT (NDESV, NOUT, DESVAR, LCONDF, LCONSV,
LXFEAS)
C
C***  DUMMY ROUTINE.  Not used in the formulation
C
      INTEGER NDESV, NOUT
      REAL DESVAR(NDESV)
      LOGICAL LCONDF, LCONSV, LXFEAS
C
      RETURN
      END



      SUBROUTINE USRANA (NDESV, NOUT, DESVAR)
C
C***  DUMMY ROUTINE.  Not used in the formulation
C
      INTEGER NDESV, NOUT
      REAL DESVAR(NDESV)
C
      RETURN
      END
```

```
      SUBROUTINE USRMON (NDESV, NDEVAR, NMPRI, NNLCON, NNLGOA,
NOUT,
     &                   DESVAR, DEVVAR, CONDEV, DEVFUN, GVAL)
C
C***  DUMMY ROUTINE.  Not used in the formulation
C
      INTEGER NOUT, NDESV, NDEVAR, NMPRI, NNLCON, NNLGOA
      REAL DESVAR(NDESV), DEVVAR(NDEVAR),
     &     CONDEV, DEVFUN(NMPRI), GVAL(NNLCON+NNLGOA)
C
      RETURN
      END



C+
C****************************************************************
*******
C
C Subroutine USRSET
C
C Purpose:  Evaluate non-linear constraints and goals.
C           NOTE - Do not specify the deviation variables
C
C----------------------------------------------------------------
-------
C Arguments       Name     Type   Description
C ---------       ----     ----   -----------
C Input:          IPATH    int    = 1   Evaluate constraints and
goals
C                                 = 2   Evaluate constraints only
C                                 = 3   Evaluate goals only
C                 NDESV    int    Number of design variables
C                 MNLNCG   int    Max. number of nonlinear
constraints
C                                 and goals
C                 NOUT     int    Output file/device number
C                 DESVAR   real   Vector of current system
variables
C
C Output:         CONSTR   real   Vector of constraint values
C                 GOALS    real   Vector of goal values
C
C Input/Output:   none
C----------------------------------------------------------------
-------
C Common Blocks:  none
C
C Include Files:  none
C
```

```
C Calls to:       none
C----------------------------------------------------------------
-------
C Development History
C
C Modifications:
C
C****************************************************************
*******
C-
C
      SUBROUTINE USRSET (IPATH, NDESV, MNLNCG, NOUT, DESVAR,
     &                   CONSTR, GOALS)
C
C---------------------------------------
C     Arguments:
C---------------------------------------
C
      INTEGER IPATH, NDESV, MNLNCG, NOUT
C
      REAL DESVAR(NDESV)
      REAL CONSTR(MNLNCG), GOALS(MNLNCG)
C
C---------------------------------------
C     Local variables:
C---------------------------------------
C
      REAL H, W, SIGY, E, P, BT, BW, CA, I1, I2, I3, I4, I5, I6,
I, WT
       REAL STR, PCR
C
C
C
C     1.0 Set the values of the local design variables (optional)
C
      H   = DESVAR(1)
      BW  = DESVAR(2)
       BT  = DESVAR(3)

C
C     2.0 Perform analysis relevant to non-linear constraints and
goals
C
C
      SIGY = 360000000.
       SF   = 2
       SIG  = SIGY/SF
       EA   = 214000000
       EB   = 1000
      E    = EA*EB
```

```
       RH   = 7850
      P    = 2000.
       CA   = (2*(BW-BT)*BT)+(BT*BT)
      CAT  = 4*CA
       W    = H/12
      I1   = (W**4)/12
      I2   = ((W-(2*BT))**4)/12
      I3   = 2*(((BT)*((W-((2*BW)**3)))/12))
      I4   = ((W-(2*BW))*(BT**3))/12
      I5   = (W-(2*BW))*(BT)*(((W/2)-(BT/2))**2)
      I6   = 2*(I4+I5)
      I    = I1-I2-I3-I6
       BL   = 4*H
      WTM  = CA*BL*RH
       WT   = WTM+(154.4*H)
       CO   = 9375.1*exp(0.0251*H)
      STB  = 15.715*((P*H*(W/2))/I)
      STC  = 1.356*(WT/CAT)

C
C     3.0 Evaluate non-linear constraints
C
      IF (IPATH .EQ. 1 .OR. IPATH .EQ. 2) THEN
C
C        Maximum bending stress in stand
C
         CONSTR(1) = SIG - STB
C
C        Maximum compressive stress in stand
C
         CONSTR(2) = SIG - STC
C




      END IF
C
C     4.0 Evaluate non-linear goals
C
      IF (IPATH .EQ. 1 .OR. IPATH .EQ. 3) THEN
C
C        Minimize CA
C
         GOALS(1) = 0.000931/CA - 1.

C

C        Maximize height
C
```

```
          GOALS(2) = H/80 - 1.

C

C         Minimize cost
C
          GOALS(3) = 25460.73/CO - 1.

C
      END IF
C
C     5.0 Return to calling routine
C
      RETURN
      END



      SUBROUTINE USRLIN (MLINCG, NDESV, NLINCO, NLINGO, NOUT,
     &                   DESVAR, COFLIN, RHSLIN)
C
C***  DUMMY ROUTINE.  Not used in the formulation
C
      INTEGER MLINCG, NDESV, NLINCO, NLINGO, NOUT
      REAL DESVAR(NDESV),
     &     COFLIN(MLINCG,NDESV), RHSLIN(NLINCO+NLINGO)
C
      RETURN
      END
```

B.2 DAT file

```
PTITLE  : Problem Title
    Design of a cell tower

NUMSYS  : Number of system variables
    3    0    0

SYSVAR   : System variable information
height 1     40.0000     80.000       70
beamw  2      0.070      0.150       0.08
beamt  3      0.0070      0.015       0.008

NUMCAG  : Number of constraints and goals
    1    2     0    0    3

LINCON  : Linear constraints
ratio 2  : beam width thick
     (2,1.0) (3,-10.0)
EQ 0

DEVFUN  : Deviation function
   1    : level
   1 3  : level 1, 3 terms
  (-1,1) (-2,1) (-3,0)

STOPCR  : Stopping criteria
1  0  50  0.05  0.05

NLINCO  : Names of nonlinear constraints
stbend  1 : bending stress
stcomp  2 : compressive stress

NLINGO  : Names of the nonlinerar goals
minca 1  : min CA
maxht 2  : max height goal
minco 3  : min cost goal

ALPOUT   : Input/output Control
     1   1   1   1   1   1   1   1  1  1

USRMOD  : Input/Output flags
    1   0   0   0

OPTIMP  : Optimization parameters
    -0.05   0.5  0.005

ENDPRB  : Stop reading the data file at this point
```

APPENDIX C

STRUCTURE-PROPERTY RELATIONS OF THE SHEEPSHEAD TEETH

C.1 Introduction

Archosargus probatocephalus, commonly referred to as the sheepshead fish, live along the coasts of the Atlantic and the Gulf of Mexico. They can grow to a length of about 30 inches and to a weight of 20 pounds and are known for its bizarre, almost human-like in appearance, teeth (77). Previous studies have focused on the bones, scales, diet, and oral jaw strength of *A. probatocephalus* (78)(79); however, the biomechanics and the material properties of the teeth have not been examined. In general, teeth can be subjected to large loads during feeding, producing a stress and strain that may result in the failure of teeth, which is even more of a danger for the sheepshead with its dietary regimen ranging from small invertebrate species (copepods, amphipods, and mysids) to hard-shelled animals such as barnacles, crabs, oysters, and clams (77)(80)(81).

Teeth are considered one of the hardest substances found in animals (82). They exhibit exceptional mechanical properties that allow them to bear various imposed loads while retaining their shape and are ideal for biting and chewing (83). Teeth are composed of highly mineralized enamel and dentin. For example, human enamel is 85 vol% mineralized and is the hardest tissue in the human body (84). The function of enamel is to provide a hard surface for crushing and slicing food and, for some species, wounding its prey (39). Conversely, human dentin is 50 vol% mineralized, 30 vol% organic components, and 20 vol% fluids with a microstructure characterized by distinct tubules (85). The individual properties of both enamel and dentin were studied to understand the function and strength of the teeth of the sheepshead.

The chemical composition of teeth can provide insight into its mechanical strength, particularly the wt% of calcium and phosphorus (86) (87). Calcium and phosphorus are present in hydroxyapatite, $Ca_5(PO_4)_3(OH)$, the mineral strengthening human teeth; however, unlike human teeth, fish teeth are strengthened by fluorapatite, $Ca_3(PO_4)F$ (88). Compared to hydroxyapatite, fluorapatite has a higher bulk modulus (89), stiffness constants, and elastic modulus (90). In this paper, the chemical composition of the sheepshead enamel and dentin are investigated through X-ray Energy Dispersive Spectroscopy (EDS), and the micromechanical properties of the enamel and dentin were captured using nanoindentation. Nanoindentation is a common technique used for determine the mechanical properties of hard biological tissues (91) (92) (93), and the data from this study will be compared to previous nanoindentation tests done on the bonnethead shark, sand tiger shark, great white shark, and piranha (94)(95). Previous research on the mechanical properties of fish teeth have focused on sharp teeth whose primary function is to tear through the flesh of its prey. In contrast, the function of the *A. probatocephalus* teeth is to crush the shells of its prey. The goal of this paper is to investigate the microstructure, chemical composition, and material properties of *A. probatocephalus* teeth to determine if a correlation between the mechanical properties of the teeth and habitat exist.

C.2 Materials and Methods

C.2.1 Sample preparation

Specimens of *A. probatocephalus* were acquired from the Mississippi Gulf Coast. Sheepshead teeth were kept in ambient dry condition before testing, and all samples were extracted from one fish. Figure C.1 shows the extracted teeth used for this study. Molar teeth were removed, cold mounted in epoxy resin, and polished transversely approximately halfway down to create the surface for analysis. Samples were polished with a Struers TegraPol-11 (Struers Inc., Cleveland, OH) using interchangeable silicon carbide grinding discs of decreasing grit size (e.g. 320, 500, 1200, 4000.) Diamond and silica suspensions with grit size 1 μm and 0.04 μm, respectively, were used for the final polishing.

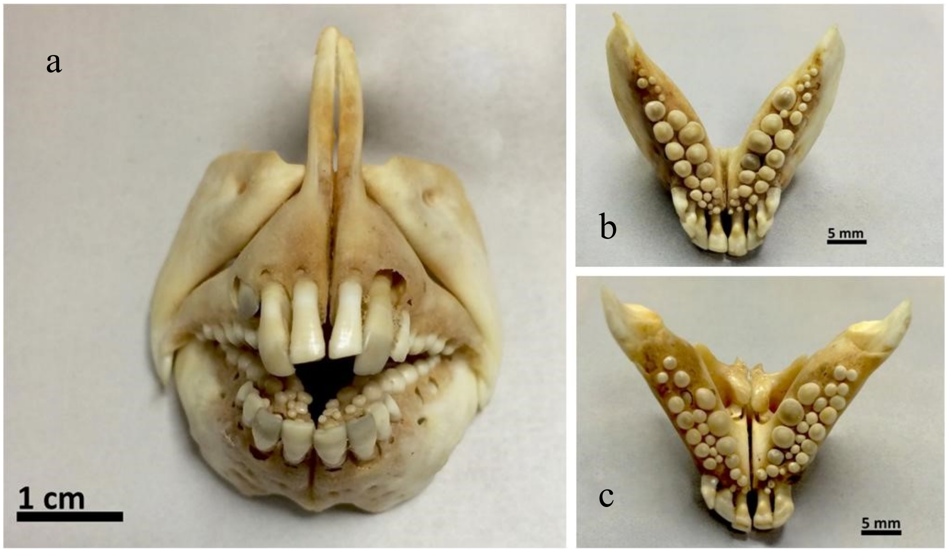

Figure C.1 (a) *A. probatocephalus* teeth. (b) Upper section. (c) Lower section.

C.2.2 Structural Analysis

Optical micrographs of polished samples were taken using a ZEISS Axiovert 200 m. The microstructure of the dentin and enamel were characterized by Scanning Electron Microscopy (SEM) at 20 kV using a ZEISS SUPRA 40 FESEM (Carl Zeiss Inc., Thornwood, NY). Figure C.2 diagrams the surface area used for nanoindentation, optical microscope, and SEM. The dentin tubule number density, dentin tubule diameter size, and nearest neighbor distances of the dentin tubules were quantified using ImageJ analysis software (20). The results are shown in Figure C.3.

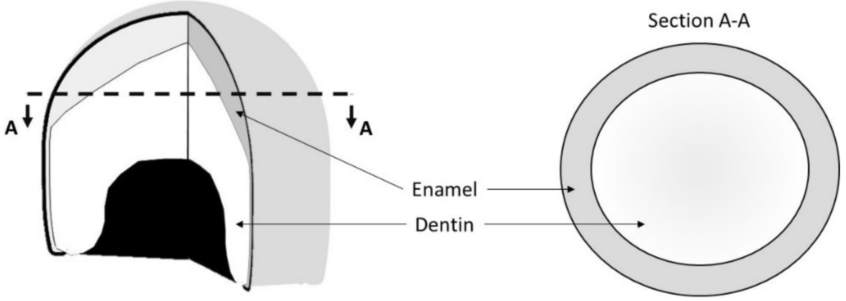

Figure C.2 *A. probatocephalus* tooth (left) and surface area (Section A-A) for structural and chemical analysis

C.2.3 Nanoindentation

Specimens were tested using a Triboindenter TI-900 (Hysitron Inc., Minneapolis, MN) with a diamond Berkovich tip of radius of 150 nm. A total number of 75 indentations with a max load of 1000 µN was performed on both the enamel and dentin sections. Specimens were indented at a load rate and unload rate of 200 µN/sec. The max load was held for 5 seconds before unloading. Load versus displacement was continuously recorded throughout the testing. Additionally, 100 indentations spaced 26 µm apart with a max load of 1000 µN were performed along the entire diameter of the polished sample to observe the changes in material properties based on the test location of the tooth. The data was analyzed using standard routines (Oliver and Pharr, 1992) (32) to determine the hardness, H. The hardness for each test is defined by Eq. (C.1):

$$H = \frac{Pmax}{A} \tag{C.1}$$

where P_{max} is the peak load, and A is the projected indentation area indenter. The reduced Young's modulus is calculated during the unloading phase and is described by Eq. (C.2):

$$E_r = \frac{1}{2}\sqrt{\frac{\pi}{A}}\frac{dP}{dh} \tag{C.2}$$

where dP/dh is the slope of the unloading curve. For the sake of this convenience, the reduced Young's modulus will be referred to as modulus for the remainder of this paper.

C.2.4 Chemical Analysis

The chemical composition of both the enamel and dentin were explored by EDS, using a ZEISS SUPRA 40 FESEM equipped with an EDAX PV7715/89 ME analyzer (EDAX, Mahwah, NJ), and the local variations in chemical composition were recorded to observe the changes in chemistry throughout the tooth.

C.3 Results

C.3.1 Structural Analysis

Figure C.3 displays the ImageJ analysis of the dentin tubules, quantifying the changes in number density, diameter size, and nearest neighbor distance. The number density increases from the dentin-enamel junction towards the center of the dentin region, increasing from 65000 per mm2 to 115000 per mm2. Likewise, the tubule diameter is larger in the center of the dentin region, increasing from 0.50 µm to 0.87 µm. The nearest neighbor distance of the dentin tubules decreases towards the center of the dentin, from 3.01 µm to 2.47 µm.

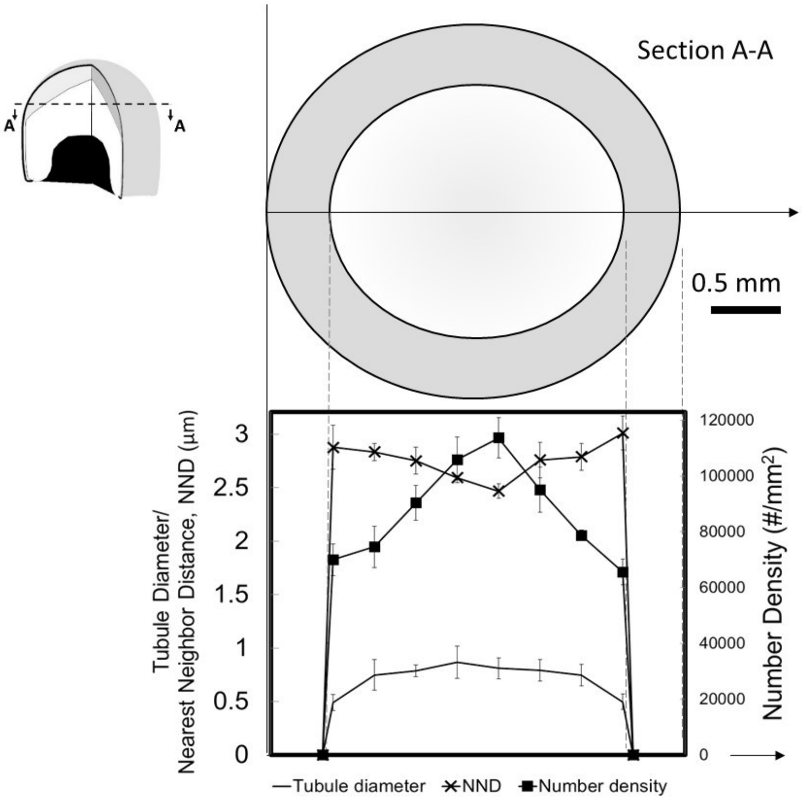

Figure C.3 Dentin tubule quantification as a function of spatial location.

C.3.2 Nanoindentation

From the nanoindentation testing, the dentin of the sheepshead teeth has a hardness of 0.89 ± 0.21 (mean ± S.D.) GPa and a modulus of 23.29 ± 5.30 GPa. The enamel of *A. probatocephalus* has a hardness of 4.36 ± 0.44 GPa and a modulus of 98.14 ± 6.91 GPa.

Additionally, uncertainty analysis was performed on the nanoindentation data. Eq. (C.3) shows the confidence interval associated with a normal probability distribution (96).

$$\bar{x} - t_{v,\alpha}\frac{S_x}{\sqrt{N}} \leq \mu \leq \bar{x} + t_{v,\alpha}\frac{S_x}{\sqrt{N}} \qquad \text{(C.3)}$$

where $\bar{x}$ is the average of the data points, Sx is the standard deviation of N measurements, and t represents a constant based on the confidence level, α, and degrees of freedom, ν. The 95 percent confidence interval for the hardness of the dentin and enamel are 0.89 ± 0.05 GPa and 4.36 ± 0.14 GPa, respectively. The 95 percent confidence interval for the modulus of the dentin and enamel are 23.29 ± 1.22 GPa and 98.14 ± 2.21 GPa, respectively.

Nanoindentation was also performed along the entire diameter of the polished sample to determine the changes in the modulus and hardness. Figure C.4 shows the changes in modulus and hardness along the diameter of the tooth. Within the dentin, the modulus and hardness are constant. However, in the enamel region, a gradient of material properties is present, with the harder material being closer to the surface of the tooth.

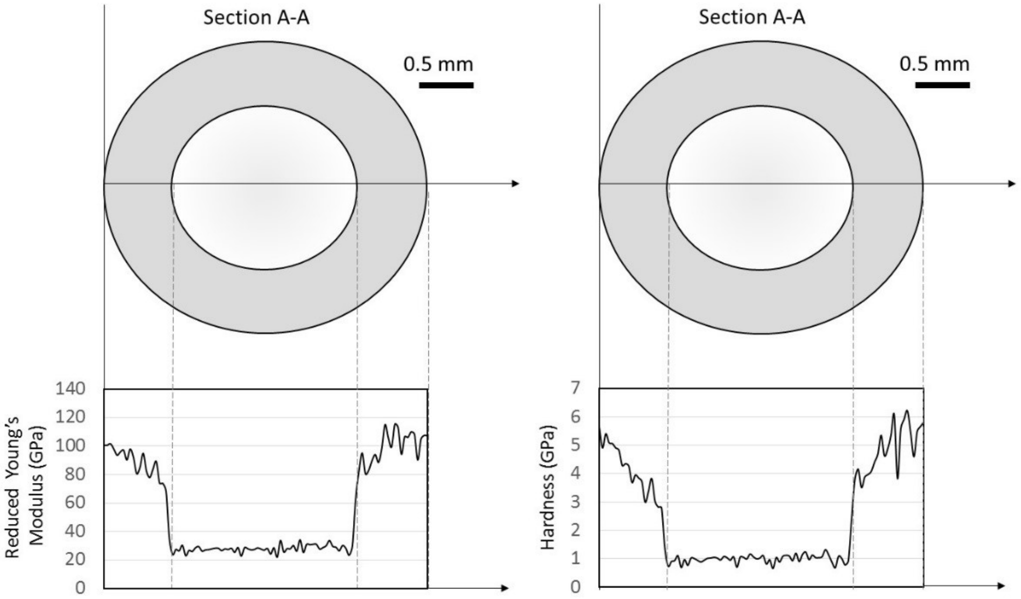

Figure C.4 Modulus and hardness along the cross section of the *A. probatocephalus* tooth.

C.3.3 Chemical Analysis

The chemical composition for the enamel and dentin regions are shown in Table *C*.1. Furthermore, the changes in chemical composition along the enamel region for calcium, phosphorus, and fluoride are shown in Figure *C*.5.

Table C.1 Energy Dispersive Spectroscopy (EDS) results for the enamel and dentin regions of *A. probatocephalus*.

	Element Weight Percent						
	Calcium (Ca)	Phosphorus (P)	Oxygen (O)	Fluoride (F)	Carbon (C)	Sodium (Na)	Magnesium (Mg)
Enamel	40.3	24.0	21.9	5.3	3.5	2.7	2.2
Dentin	36.0	22.3	25.9	4.1	5.9	2.8	2.9

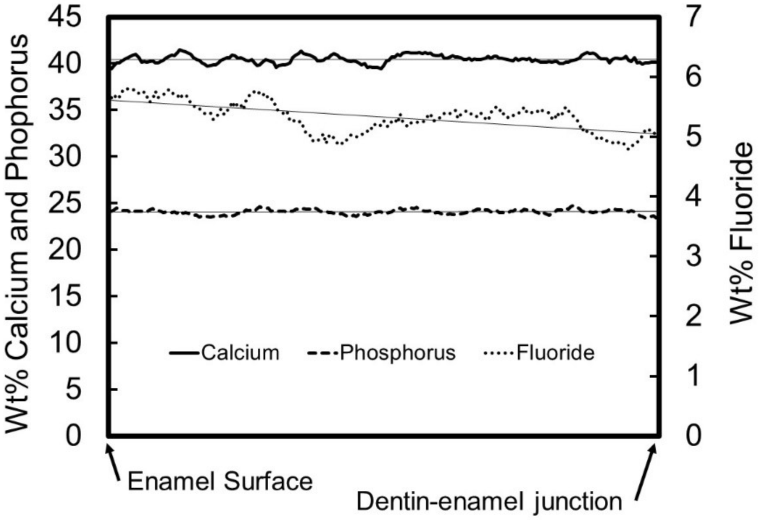

Figure C.5 Energy Dispersive Spectroscopy (EDS) results showing the wt% of calcium, phosphorus, and fluoride within the enamel region of the sheepshead tooth.

C.4 Discussion

The purpose of this study was to investigate the microstructure, chemical composition, and material properties of *A. probatocephalus* (sheepshead) fish teeth. The results are the first reported for the sheepshead and provide material properties for a fish that has a diet consisting of hard-shelled organisms that include barnacles, crabs, oysters, and clams.

The presence of fluoride in the sheepshead teeth have also been noted in other fish by Suga et al.(97), who investigated the presence of fluoride in various other fishes. The fluoride concentration seen in this paper coincides with the findings in Suga et al. which showed a range of 1.5 wt% - 5.5 wt% fluoride in the enamel of different fishes. Though marine fishes, such as the sheepshead, live in an environment that naturally contains fluoride, Suga et al.(97) observed that the fluoride concentrations in the enamel of fishes were not dependent on its environment, but rather the phylogeny of the fish.

From Figure C.4, there is a gradual increase in modulus and hardness within the enamel region traversing to the tooth outer layer due to the chemical composition gradient within the enamel. Previous research by Cuy et al. (86) and Jeng et al. (87) showed that the changes in material properties of the human enamel correlate with the wt.% of calcium and phosphorus; whereby, an increase in calcium and phosphorus led to an increase in hardness; however, from Figure C.5 the wt.% of calcium and phosphorus for the sheepshead tooth does not change within enamel region. Instead, a change in the wt.% of fluoride is present. Figure C.6 compares the similar trends of the modulus and wt.% fluoride, suggesting a direct correlation between the two.

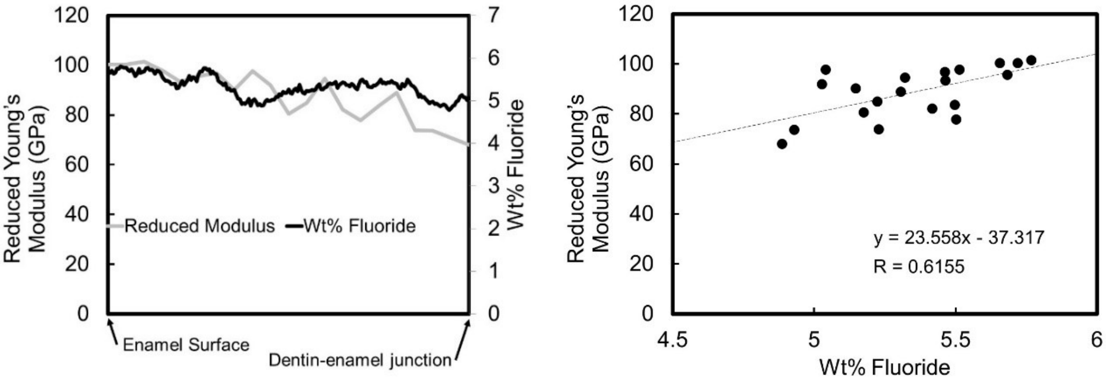

(a) *(b)*

Figure C.6 a). Modulus and wt.% Fluoride throughout the enamel region. b.) Modulus vs wt.% Fluoride.

SEM images in Figure C.7 capture the tubule structures existent within the dentin layer of the tooth. As aforementioned, tubule number density differences exist between the tubules located along the dentin-enamel junction and those located within the center of the dentin region (Fig. 3). Differences in tubule density and diameter have been previously been reported by Komabayashi et al.(98), who observed a factor of two increase in the dentin tubule density of human mandibular canines from the outer to the inner surface. Similarly, a sheepshead's tooth exhibits an increase in tubule density by a factor of 1.75 from the outer to inner surface. Additionally, human teeth studied by Jakiel et al. (99) noted the increase of dentin tubule diameter towards the root of the tooth. Because of the nanoindentation methodology used within our paper, the results observed in Figure *C*.4 were not able to show the effects of dentin tubules on the hardness and modulus properties of the dentin. However, previous research (100) using a microhardness technique has noted an inverse relationship between the tubular density and the hardness. For the current study, the average modulus of 23.29 GPa observed in the dentin in Figure C.4 is more of a representation of the intertubular dentin (or the dentin between the tubules). Additionally, the dentin hardness does not show a spatial dependence, which is seen in previous studies done on the intertubular dentin in human teeth (91).

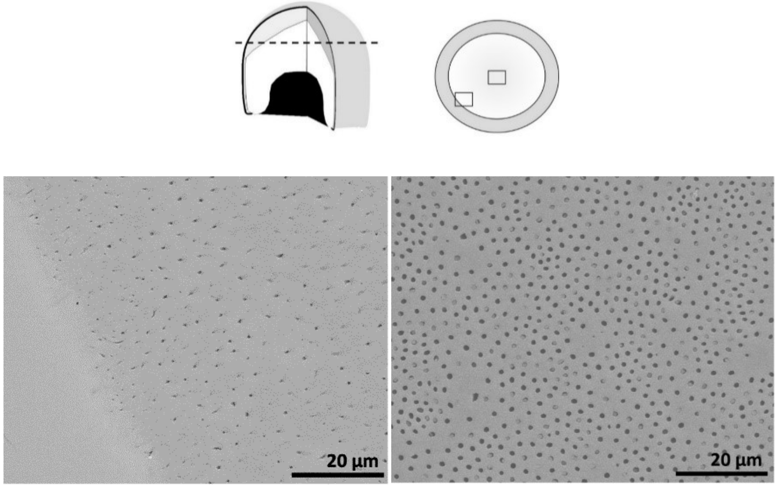

Figure C.7 Scanning Electron Microscope (SEM) images of a polished tooth surface comparing the dentin tubule density near the dentin-enamel junction (left) and in the center of the tooth (right).

Currently, a relationship describing the effect of tubular density and tubule diameter on the microhardness of the dentin does not exist. To estimate the effect of the tubule density and diameter within the sheepshead dentin, an approach similar to that done by Voigt (101) is applied:

$$h = h^{*}(1 - \varphi) \tag{C.4}$$

where h is the microhardness of the dentin, h^{*} is the hardness of the intertubular dentin, and φ is the area fraction of the pores caused by the dentin tubules. Eq. (C.4) can be rewritten as:

$$h = h^{*}(1 - \eta\nu) \tag{C.5}$$

where η and ν are the number density and cross-sectional area of the dentin tubules, respectively. Using this approach to determine the microhardness properties of human dentin produces results that are comparable to previous microhardness results. Data taken from Sumikawa et al. (102) and Marshall et al. (103) were used to estimate the microhardness of the outer region of the human dentin. These calculations compared well with microhardness results from Pashley et al (104). Data used for this comparison is compiled in Table *C*.2.

Table C.2 Comparison of human dentin microhardness experiments done by Pashley *et al.* and microhardness calculated from Eq. (5): $h = h^{*}(1 - \eta\nu)$. (102)(103)(104)

Tooth	Region	Tubule Density, η (#/mm^2)	Tubule Cross Sectional Area, ν (mm^2)	Intertubular Hardness, h* (GPa)	Micro-hardness, h (GPa)	Calculated Microhardness: h = h* (1-ην) (GPa)
Lateral Incisor						
	Distal Area	29400	1.52E-06	0.74	0.69	0.71
	Central Region	38200	1.52E-06	0.74	0.69	0.70
Primary Canine						
	Distal Area	24100	1.96E-06	0.74	0.69	0.71
	Central Region	18300	1.96E-06	0.74	0.69	0.71

Using Eq. (5), the microhardness of the sheepshead dentin can be calculated from the image analysis results from this paper. Figure C.8 shows the spatially dependent microhardness of the dentin. This approach can be used to analyze the dentin region of different animals.

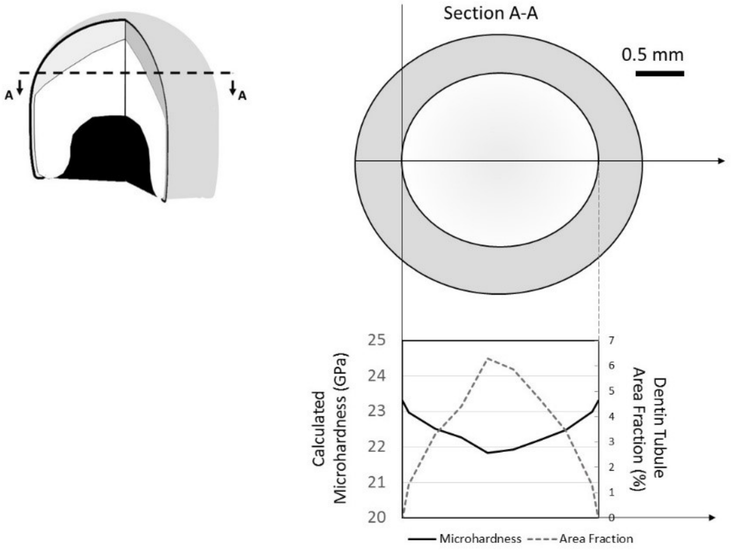

Figure C.8 Spatially dependent microhardness calculated from Eq. (5) ($h = h^{*}(1 - \eta\nu)$) and area fraction of the dentin tubules within the sheepshead dentin.

Additionally, nanoindentation tests have been performed on the teeth of the sand tiger shark (95), bonnethead shark (95), piranha (94), and Great white shark (94). Table C.3 and Figure C.9 compare the results from different fish species with the results obtained from the sheepshead.

Table C.3 Material properties of teeth from different fish species.

Species	Material	Common Name	H (GPa)	E_r (GPa)	Reference
Carcharias taurus	Dentin	Sand tiger shark	1.21±0.16	28.44±2.21	(16)
Sphyrna tiburo	Dentin	Bonnethead shark	0.97±0.07	22.49±1.72	(16)
Serrasalmus manueli	Dentin	Piranha	0.8±0.3	23.0±6.0	(17)
Carcharodon carcharias	Dentin	Great white shark	0.7±0.2	20.4±5.6	(17)
Archosargus probatocephalu	Dentin	Sheepshead	0.89±0.21	23.29±5.30	current study
Carcharias taurus	Enamel	Sand tiger shark	3.20±0.20	72.61±4.73	(16)
Sphyrna tiburo	Enamel	Bonnethead shark	3.53±0.30	68.88±1.50	(16)
Serrasalmus manueli	Enamel	Piranha	4.1±0.9	86.5±15.9	(17)
Carcharodon carcharias	Enamel	Great white shark	4.1±1.1	84.4±19.9	(17)
Archosargus probatocephalu	Enamel	Sheepshead	4.36±0.44	98.14±6.91	current study

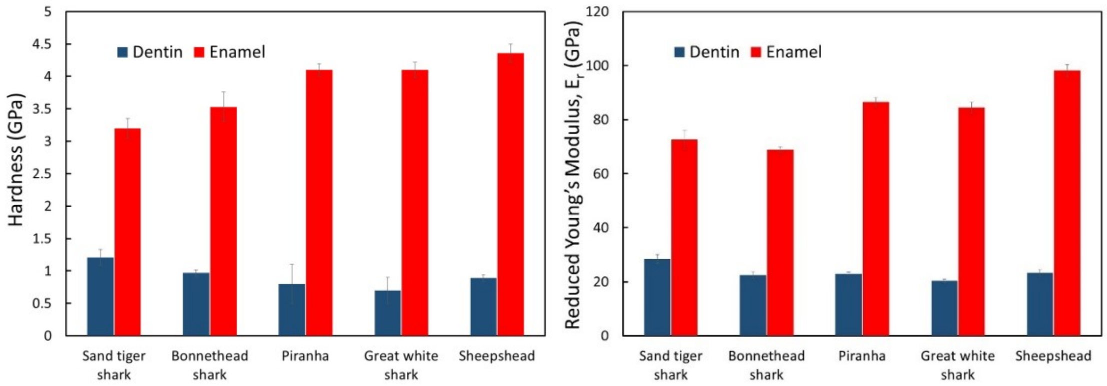

(a) (b)

Figure C.9 Comparison of (a) hardness and (b) modulus for various aquatic species (94)(95). Error bars represent t_{95}, a 95% confidence interval.

From Figure C.9, the sheepshead teeth have a higher average modulus and hardness when compared to the results from other fishes. The material properties of the sheepshead enamel (4.5 GPa hardness and 100 GPa modulus) are also comparable to human enamel, which have exhibited a maximum hardness of 6 GPa and modulus of 110 GPa at the tooth's surface (86).

The differences in mechanical properties observed in Figure C.9 may be a result of dietary habits and functions of the teeth. Previous biomechanical studies have examined the form and function of shark teeth (105)(106). The primary predatory strategy of the great white shark is to severely injure its prey by taking a huge bite of its flesh, bring it close to death, and then feed (107). Similarly, piranhas are known to use their sharp teeth to take bits of flesh from fishes and other vertebrates (108). Additionally, the structure of the shark and piranha tooth contain serrations, which are known to enhance cutting efficiency (109). As such, the shape and structure of the piranha and shark tooth are ideal for the fishes' strategy of attacking the flesh of its prey. Alternately, because many of the hard-shelled prey of sheepshead fish are much slower, and even stationary, the need to impair its prey is unnecessary. Instead, the typical behavior for feeding on hard shelled animals consists of positioning their prey over the teeth, forcefully biting, and ejecting any loose shell debris (78).

Where the great white shark and piranha primarily attack the flesh of its prey, the sheepshead often have to break through the shells of its diet. The function of the sheepshead teeth requires stronger mechanical properties, which allow the fish to fracture crabs, oysters, barnacles, and clams. Figure C.10 compares the hardness and elastic moduli obtained from previous studies of the prey of the sheepshead to the elastic modulus and hardness of the teeth of the sheepshead (110)(111)(112). Furthermore, the elastic modulus exhibited by the some of the sheepshead prey is much greater than recorded values observed for fish bones encountered in the prey of sharks and piranhas. The mean modulus values of carp and tilapia rib bones were found to be 7.5 GPa and 8.6 GPa, respectively (113).

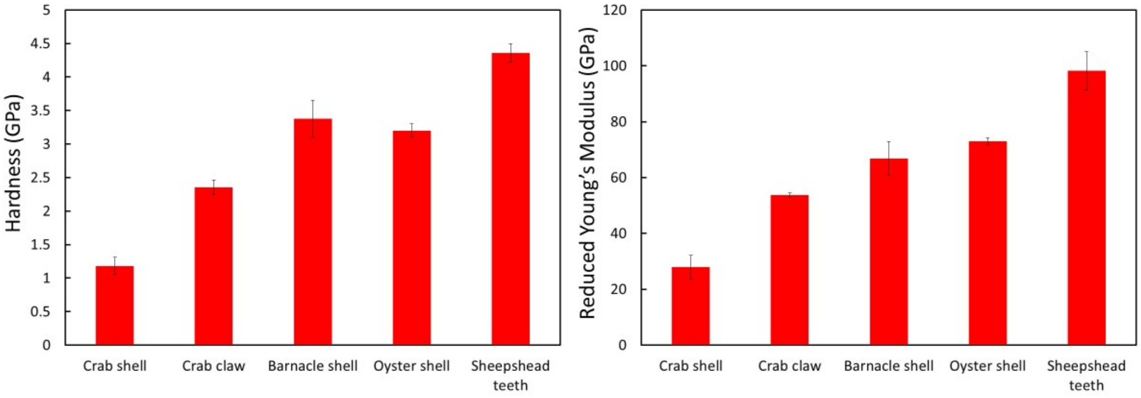

(a) (b)

Figure C.10 (a) Hardness and (b) modulus of the sheepshead teeth compared with some of sources of the sheepshead's diet (110)(111)(112). Error bars represent standard deviation.

C.5 Conclusions

In this study of the *A. probatocephalus (sheepshead fish)* the mechanical properties and chemical composition of the enamel and dentin were studied. Nanoindentation tests showed that the material properties of the enamel increased closer to the surface of the tooth. EDS results further suggest that the modulus and hardness gradient are a result of the wt% fluoride within the enamel, where an increase in fluoride results in an increase in modulus and hardness. Additionally, an approach to determine the effect of tubule diameter and number density on the microhardness was presented in this paper. The mechanical properties of the sheepshead teeth were also compared to other aquatic species. The sheepshead teeth exhibit higher modulus and hardness compared to shark and piranha teeth, which may be a result of the contrasting functions of the teeth and dietary differences between the shark, piranha, and sheepshead. Finally, the sheepshead teeth have a greater hardness than the hardness of the materials in which they eat.